

UNIVERSITÀ DEGLI STUDI DI
MILANO-BICOCCA

DIPARTIMENTO DI FISICA “G. OCCHIALINI”

TESI DI LAUREA MAGISTRALE PER IL CORSO DI
ASTROFISICA E FISICA DELLO SPAZIO

**Studying the Mass Bias
in Galaxy Clusters
using Simulated Athena Satellite
Observations**

Supervisor:

Prof.ssa Monica COLPI

Candidate:

Riccardo Aurelio GILARDI

External Supervisor:

Dott. Iacopo BARTALUCCI
(IASF-INAF)

22 Marzo 2022



Contents

Abstract	3
1 Introduction	5
1.1 The Λ CDM model of the universe	5
1.2 Galaxy Clusters	8
1.2.1 Galaxy clusters as cosmological probes	9
1.2.2 Observational properties and mass estimates	11
1.3 The tension with the Planck CMB	13
1.4 The problem with X-Ray Mass	15
2 Data analysis	18
2.1 X-ray Observations	18
2.1.1 X-ray calibration files	20
2.2 X-ray telescopes	22
2.2.1 <i>Chandra</i> and XMM- <i>Newton</i>	22
2.2.2 Athena+	22
2.3 Mass Measurement	24
2.4 <i>Chandra</i> X-ray analysis	26
2.5 The role of our Pipeline	27
3 The Pipeline	28
3.1 Point-like source with Power-law emission	28
3.1.1 Initializing the pipeline and XML files	28
3.1.2 Simput Files Creation	29
3.1.3 Simulation	30
3.1.4 Imaging	32
3.1.5 Spectra	34
3.2 <i>Chandra</i> results comparison and simulations	35
3.2.1 Cluster Simput Files Creation	35
3.2.2 Background Simputs	39
3.2.3 Simulation and Imaging	43
3.2.4 Spectra and Temperature Fit	47
4 Profiles and science using the pipeline outputs	52
4.1 Brightness Profiles	53
4.1.1 Background and Point-like sources	54
4.1.2 Analysis of toy-model objects	56
4.2 Temperature and abundance profiles	57
4.2.1 The elephant in the room: WFI vs X-IFU	59
4.3 Deprojection and Forward Method	60
4.3.1 Instrumental corrections and cosmology	60
4.3.2 Forwarding method and Mass profile derivation	62
4.4 Comparison with <i>Chandra</i> analysis	64
4.4.1 Choice of the sample	64
4.5 Bottom line of the pipeline and analysis code development	69

5 Results	70
5.1 Chandra Comparison	71
5.2 Simulations	75
6 Conclusion	79
Bibliography	82
Appendices	86
A <i>Chandra</i> comparison plots	86
B Simulated clusters plots	91

Abstract

Galaxy Clusters are the largest self-gravitating objects in the Universe. They form at the nodes of the cosmic web and are mostly constituted by dark matter, $\sim 70\%$, and a hot gas filling the cluster volume, namely the ICM, accounting for $\sim 28\%$ of the mass. Galaxies and stars form only about 1-2% of their total mass. The number distribution of galaxy cluster mass as a function of redshift can be used to constrain the cosmological parameters (e.g. [49]). For this reason, galaxy clusters are powerful cosmological probes if their mass is well-known.

In recent years, the **Planck collaboration** (see [33]) measured σ_8 using cluster count from the Cosmic Microwave Background power spectrum and the cluster mass count as derived from the Sunyaev Zel'Dovich (SZ) effect and found a 3σ tension. This means that the same instrument showed a large discrepancy between estimates of the same quantity and while the power spectrum is a well-studied object, estimates for the mass of clusters from the measure of the SZ effect were calibrated on X-ray.

The mass of clusters is derived in X-rays under the hypothesis of **hydrostatic equilibrium (HE)**. The validity of this assumption has been studied in the central bright regions of the clusters (see [35] and [37]). The outer regions of the cluster are expected to host a plethora of physical phenomena related to ongoing merging activities. For this reason, one needs to carefully study what are the limitations of the HE there. Unfortunately, the emission from these regions is faint and current X-ray observatories do not have sufficient throughput to collect it.

Studies on a large sample of clusters and simulations estimate a 15% bias between the X-ray HE mass and the "true" mass in the outer parts. However, this bias alone does not explain the tensions found by Planck (see [17] and [23]). At the same time, one can not assume the larger HE biases necessary to solve the tension as this would require non-thermal pressure terms larger than expected in modern studies (e.g. [15]) and would clash with the actual **baryon fraction** estimates from other cosmological measurements (for example see [32]).

In this context, the **Athena+ satellite** that will be launched around 2030 will be a game-changer. The high throughput of its mirrors combined with the large effective areas of its imager WFI and spectrometer X-IFU will be able to observe the outer regions of clusters.

In this master thesis, I studied the scientific output that will be possible to obtain with Athena by producing and studying mock WFI observations made using a set of cosmological simulations. In particular, under the guidance of Dr Iacopo Bartalucci from IASF-INAF Milano and under the supervision of Prof. Monica Colpi from Università Degli Studi di Milano-Bicocca, I investigated the HE in the outer region of galaxy clusters observed with Athena. I developed a **pipeline** with which we can derive the mass profile of a cluster as it would be seen from Athena WFI, either starting from an image of a real cluster from another satellite or with a cluster built from a model.

The analysis pipeline is completely written in python, but the simulations are made using a combination of the ray-tracing simulation software SIXTE (see [12]) and of the X-ray astronomy toolkit XSPEC (see [4]). These codes and their use are extensively explained in the thesis.

We first tested the robustness of the pipeline by comparing results obtained with real observation taken with *Chandra* and WFI mock observations of the same objects.

We obtained that our mass estimates and *Chandra*'s had an average median ratio of $M_{Ath}/M_{Cha} \sim 1.00$, with variance of $\sim 6\%$ and a peak precision of $\sim 0.2\%$ in the clusters' intermediate region.

We also demonstrated that Athena will be able to derive results with similar precision as the actual observatories with a much smaller exposure time and we showed the typical maximum radius of detection WFI will be able to observe as a function of the sky, particle background and of exposure time.

Finally, we produced Athena WFI observations of a restricted sample of eight simulated clusters drawn from the suite of cosmological simulations of the 300project (see [1]).

We obtained the following:

- We found out that WFI will be capable of seeing colder substructures and clumps of matter surrounding the hotter inner part of clusters, which have always been invisible to the actual X-ray telescopes. This is with a fraction of the exposure time needed for actual X-ray observations of the only inner part of galaxy clusters.
- We understood how fundamental it is to be able to distinguish the larger objects from point-like sources at large radii, where actual X-ray telescopes suffer from PSF deterioration. Now we know that with Athena we will understand better the dynamics of galaxy clusters and we will identify much more easily matter falling from the dark matter filaments into the central regions, while with current instruments even a point-like source within $5 - 10'$ from the cluster centre would have a PSF of $5\text{--}20''$ in radius, making it mistakable for a real large clump of a gas interacting with the cluster potential.
- We investigated the impact of substructures on the results by comparing mass profiles obtained masking and including them in the analysis. Our final estimates of the total mass varied by a factor smaller than 6%, meaning the turbulence pressure term connected with the dynamics of these clumps did not correct by a large margin the HE results, in agreement with what has been recently obtained by [15] and showing again how the problem of galaxy cluster mass and cosmological parameter estimation is still open and cannot all be addressed to the X-ray mass measurement only.
- We observed a systematic ratio between the known mass of objects at R_{500} and our estimates of $\sim 0.97 \pm 0.03$ for the different sources. This could represent another proof of the presence of a non-thermal pressure term to be considered in the mass estimation for cluster but might also be corrected with more precise instrument files for WFI when they will be available.
- X-IFU will be also able to observe directly lesser dense and bright sub-structure and clumps surrounding galaxy clusters and it could extract spectra from the cosmic web filaments. With this knowledge, we could also develop advantageous observational strategies combining WFI and X-IFU observations of different parts of the same objects.

The pipeline product of this work and with which we obtained our physical results on the topic of clusters mass is a complete and usable piece of software that can be used to preview and predict many possible Athena results in galaxy cluster astronomy, develop possible observational strategies for objects in a different context and studies on background analysis and characterization. It could be also used as a baseline to produce a similar pipeline for the spectrometer X-IFU.

This work fits in with the actual horizon of starting projects on the topics of X-ray astronomy and cluster physics: the X-ray E-Rosita full-sky survey will discover thousands of clusters, for which it will be fundamental to define a follow-up strategy with Athena. Also, Euclid will deliver thousands of weak lensing measurements, yielding unprecedented multiwavelength support.

1 Introduction

In this first section of the thesis, I will describe the theoretical framework on which our work is based and I will explain the issues which bring us to develop our pipeline for producing simulated Athena-WFI images of galaxy clusters.

This is not an extensive or complete discussion on the topics. In this regard and for the love of simplicity I will try to avoid introducing into this discussion mathematical symbols or unnecessary formalism, such as general relativity tensorial algebra.

I cite the sources for the results I am going to discuss, but also more generic reviews and articles which discuss different perspectives and arguments I did not directly take into account while developing this work.

Even with the technical and theoretical preparation from my academic studies, to work on this project I had to learn most of my current knowledge on the physics of galaxy clusters: their known properties, structure, observation techniques with which we study them, their link to cosmology and the current state of the art information on them and on the mass bias issue.

1.1 The Λ CDM model of the universe

Cosmology has been one of the most lively branches of astrophysics and astronomy since the first half of the 20th century. Thanks to the sparks ignited by early theoretical works animated by considerations on the theory of general relativity and the progressively deeper observations in many wavelengths we've been able to obtain with our always improving technologies and knowledge, we reached a point at which we're capable of measuring different cosmological parameters with high precision and through different kind of observations.

Large-scale structure, CMB and Cosmic expansion Contemporary cosmology is based on the so-called **copernican principle**, for which on a **large-scale** the universe can be considered at any time to be homogeneous and isotropic in all of its properties¹. Now we know the large-scale at which we cannot distinguish any difference between structures and voids is in the order of tens to hundreds of mega-parsecs.

One of the reasons astronomers started considering the hypothesis of the universe to be evolving is because in the late 20s Edwin Hubble and Milton Humason published the results of their galaxy observation campaign. They derived a simple empirical relation between a galaxy distance and the speed with which it was moving away from us, now called the **Hubble law**, for which galaxies are moving away from us in all directions, with velocities increasing with their proper distance from us:

$$v = H_0 d_P \quad (1)$$

This was a cutting-edge result that led to the beginning of a fertile discussion about whether the universe was expanding with a constant density (the so-called **steady-state scenario**, sustained between others by Fred Hoyle) or if it was somehow born from a singularity with very high density (**big bang scenario**, first indirectly described in the notorious " $\alpha\beta\gamma$ -paper" written by Ralph Alpher and George Gamow in 1948).

This discussion took a strong turn in favour of the Big Bang scenario when two Bell laboratories radio engineers, Arno Penzias and Robert Wilson, discovered in 1965 an isotropic background signal with a black-body temperature of around 2.7 keV and emissivity peaks in the microwave, at 1.87 mm , which was later recognised to be the **cosmic microwave background (CMB)** predicted by Gamow as a proof for the Big Bang scenario in 1948.

CMB is a residue black-body emission from a period around $z=1100$ we call **recombination time** at which, thank its expansion, the universe went from being so hot and dense that matter² was coupled with

¹If these symmetries were also constant at every time we would talk about a **perfect Copernican principle**

²at the time, mostly an hydrogen plasma

radiation, to being cold enough for matter to become transparent to light, de-couple from it and radiate it away.

What we see now everywhere is a redshifted image of the universe from the recombination time. And since CMB was emitted just after the time radiation was still coupled with the matter, its energy density distribution represents the matter density distribution of the time.

The CMB is now one of the most studied astronomical sources ever, by missions such as COBE (1989-1996), WMAP (2001-2003) and Planck (2009-2013). From the measurement of its temperature (and consequently density) fluctuations power-spectrum and its polarization matrices, we directly measured many cosmological parameters and it has shown us how the universe reached its current state with time. For this work in particular I will cite three³ of the tens of paper the Planck collaboration is publishing with the results of its analysis on Planck CMB data.

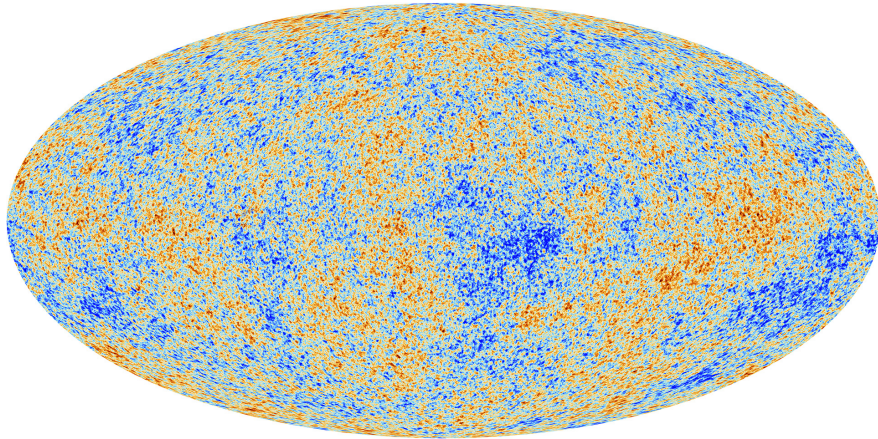


Figure 1: The CMB full-sky map obtained by the **Planck collaborations**. The color map refers to the temperature of the radiation. The blue and red being cold and hot, respectively. The fluctuations are of the order of magnitude of $10^{-4} \sim 10^{-5} K$.

Cosmological parameters and Friedmann equations Within the context of Einstein's **general relativity** it is possible to describe the universe through its **curvature** κ , which affects its metric tensor $g_{\mu\nu}$ and hence how light and matter move in space-time.

The extension of the Copernican principle to this theory is that the metric of a dynamic space-time like ours can be sliced into maximally-symmetric three-dimensional surfaces⁴, in which every mechanical property is isotropic and homogeneous and all the time dependencies are linked to a single **scale factor** $a(t)$. This kind of metric is called a **Robertson-Walker metric**.

Using it to solve the conservation of energy-matter equation in tensorial form and Einstein equations, which links the space-time metric to its mass-energy content, gives us the **Friedmann equations**, which describe the relationship between the scale factor $a(t)$ with the mass-energy density evolution of its component, which are matter, radiation and cosmological constant Λ .

All the parameters mentioned above and the observables linked to them, such as the **Hubble parameter** $H(t) = \dot{a}/a$ are connected through this set of differential equations. Even without explicitly writing all of them, the thing to pinpoint is that their derivation is interconnected and as we will see, most of them can

³see [31], [32] and [33]

⁴In formal terms, we're talking about a $R \times \Sigma$ manifold, R representing the time direction and Σ being a 3-dimensional maximally-symmetric submanifold.

be measured through many different methods. Comparing these many different measurements of the same interconnected parameters describing our cosmology is the subject of **contemporary cosmography**.

A way to synthetise the characteristics of a cosmological model through a manipulation of Friedmann equations is by defining the **density parameters** Ω for its components, expressed as

$$\Omega = \frac{8\pi G}{3H^2(t)}\rho = 1 + \frac{\kappa}{H^2(t)a^2(t)} \equiv 1 - \Omega_c \quad (2)$$

Each mass-energy component also has its own **equation of state**, written in the form of a relation between its pressure P and its energy density ρ :

$$P \propto \rho \propto a^{-3(1+w)} \quad (3)$$

where adiabatic exponent w is equal -3 for matter, -4 for radiation and 0 for the cosmological constant.

Λ CDM model and structure formation Putting together our theoretical framework based on general relativity, with our actual best estimates from many different kind of measures for the cosmological parameters, suggests our universe is **flat** ($\kappa = 0$) and **Λ -dominated**, with

$$\Omega_\Lambda \simeq 0.7 \quad \Omega_\Lambda \simeq 0.3 \quad \Omega_\Lambda \simeq 10^{-4} \quad h \simeq 0.67 \quad (4)$$

where $h \equiv H_0/100 \text{ km/s/Mpc}$ is the reduced Hubble constant.

Many different observations suggest that the vast majority of matter in the universe, between 80% and 90% is non-baryonic and does not interact with light, but only through gravitation. We call it **dark matter (DM)** and even if its nature is still being discussed, we believe it was already present before the recombination time.

The structure of DM can be linked to how, after CMB was emitted, matter on the large-scale formed a **cosmic web** of filaments at which nodes both its baryonic and DM component collapsed to form the self-gravitating structures that we see today, from stars to galaxies and so on. The size and mass of CMB anisotropies are linked to that of matter clouds that are now still forming the structure we observe.

A widely-accepted parametrization of the Big Bang cosmological model, which I also adopted in this project is the so-called **Lambda cold dark matter model** (Λ CDM), also called the standard model. This modelization assumes our actual universe energy density is mostly formed by cosmological constant, baryonic matter and **cold dark matter**, which would be made up of small particles when compared to the size of proto-galaxies⁵. Their size can be linked to their thermodynamic properties and predict they had a large free streaming length in the early stage of the universe.

This theory is highly arguable and still discussed, but is coherent with Planck anisotropic distribution and its cosmological parameter estimates which we're using as a reference for this project and can predict how matter over-densities in the early universe growth until they collapsed into larger and larger structures and they reach the actual galaxies mass distribution we see today⁶.

One of the most interesting consequences of this model is that it predicts a **hierarchical structure formation**, with smaller structures being formed for the first time earlier than larger structures. Some works predict for example the first stars formed at around $z \simeq 65$ and the first galaxy similar to the Milky Way formed at around $z \simeq 11$ ⁷.

⁵It's beyond the objectives of this thesis to explore this any further, but the most popular hypothesis is that these particles might take the form of **Massive Compact Halo Objects (MACHOs)**, **Robust Associations of Massive Bayonic Objects (RAMBOs)** or some kind of yet undiscovered **Weakly-Interacting Massive Particles (WIMPS)**.

⁶The theory is far from being perfect and one of its major unresolved question today is that a CDM model would predict a larger number of small-sized white dwarves in the early universe than the number we see. It's unclear if they do not exist or we did not see them yet for some reason.

⁷**The first stars in the Universe**, Naoz, S., Noter, S., & Barkana, R., MNRAS Letters, Volume 373, Issue 1, pp. L98-L102, 2006

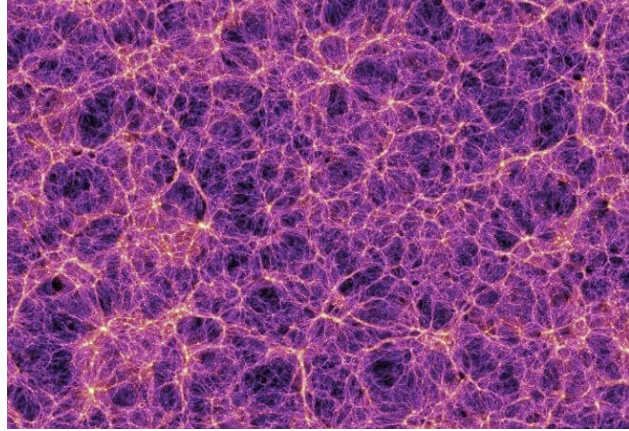


Figure 2: Dark matter distribution as predicted by the Millennium simulation at $z=0$ i.e. present time. Filaments of dark matter cross at nodes within which galaxy cluster form and evolve.

In this project we did not make any comparison between different cosmological models, adopting the Λ CDM as a reference and sticking to its parameter estimations during the pipeline development and in our subsequent analysis. However as I will explain in sections 3 and 4, our code can be easily adapted to produce WFI simulations and analyze them in the function of any set of cosmological parameters (critical densities and H_0 above all).

1.2 Galaxy Clusters

Galaxy clusters are the largest self-gravitating objects in the Universe. They form in the nodes of the cosmic web after the first smaller group of galaxies started to converge under the influence of the same gravitational potentials at around $z \sim 1^8$, just around $7.5 \cdot 10^9$ years ago⁸. Them being so "recently" formed is consistent with the prediction of a hierarchical model for the cosmological structure formation theory.

Most of the known clusters lie within $z \sim 0.5$ and have a total mass of the order of $10^{14} \sim 10^{15} M_\odot$, with virial radii in the order of $100 \text{ kpc} \sim 1 \text{ Mpc}$. They are mostly formed by dark matter, which constitutes $80 \sim 85\%$ of their total mass. The rest of which is made of baryonic matter, with around $13 \sim 15\%$ is constituted by hot plasma, namely the **intra-cluster medium (ICM)**, and only the 2% of their mass being in the form of stars and compact objects.

Their shapes and dynamics are very diverse, going from more relaxed and unperturbed structures to the most perturbed and asymmetric structures which are undergoing evident merging processes like the famous bullet cluster.

Figure 3 shows an example of this variety of shapes and dynamical states.

⁸Earliest example of observed proto-group of galaxies, which did not self-gravitate yet, have been found at up to $z \sim 6 - 7$. For example see Harikane, Ouchi, Ono et al. ApJ 883 142 (2019)

⁹Differently from what is used to in other branches of astrophysics, in the field of galaxy cluster physics any reference to the "local universe" is usually about the region with $z \lesssim 0.2 \sim 0.3$.

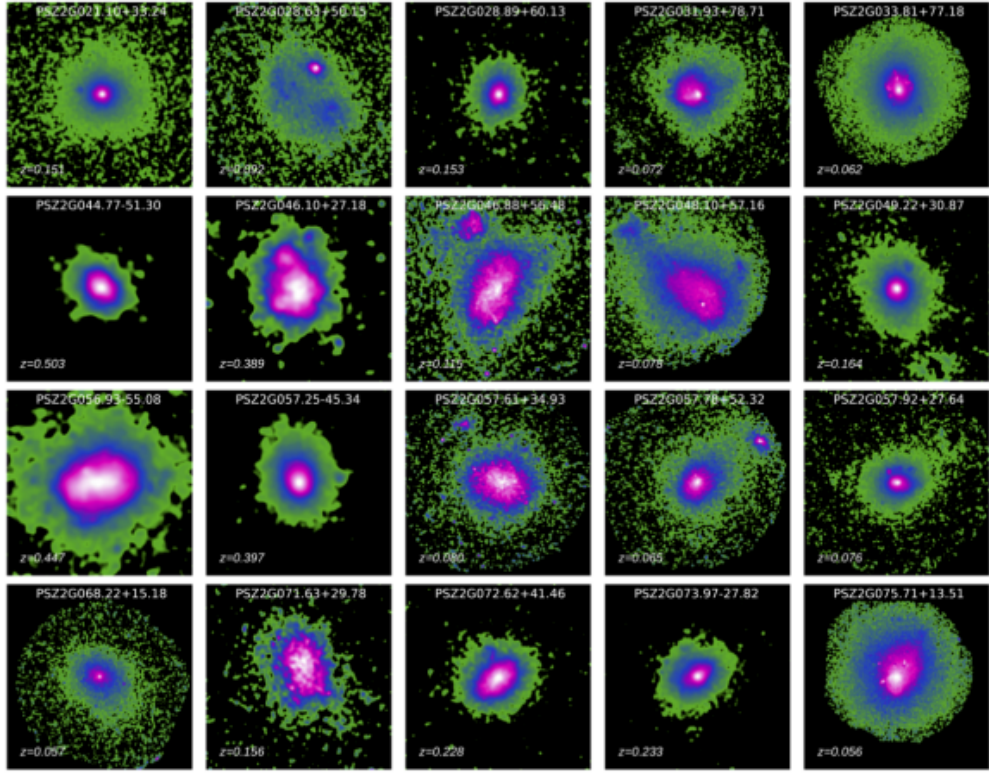


Figure 3: Gallery of clusters from the CHEXMATE collaboration presentation paper [47]. Each image represents an X-ray observation in the $[0.7 - 1.2]$ keV band. This gallery shows the diversity of galaxy cluster shapes.

1.2.1 Galaxy clusters as cosmological probes

It might sound overly simple, but the most important properties of galaxy clusters are that they are very big and bound. They are so big that they are the closest object in the universe to the size of the large-scale structure.

These two simple facts inextricably tie their properties to that of their surrounding. Even intuitively one might reasonably expect that their evolution, mass and distribution, must be tightly linked to the universe's evolution. This is exactly the case, as it was demonstrated with numerical simulation but also observed directly that they can be used to constrain and bound cosmological parameters, making them optimal cosmological probes.

In particular, the main object of this thesis project, the galaxy cluster mass profile, allow us to constraint the mass and cosmological constant density parameters as shown in the work of Vikhlinin et al. 2009¹⁰ and the work of Borgani and Guzzo 2006¹¹ of which I'm showing two plots in **Figure 4**.

Knowing with high precision the number of clusters and their masses is a powerful cosmological measurement instrument. In general, the study of these large objects' properties is the link between dynamics, physical processes and cosmology.

¹⁰see [49]

¹¹see [7]

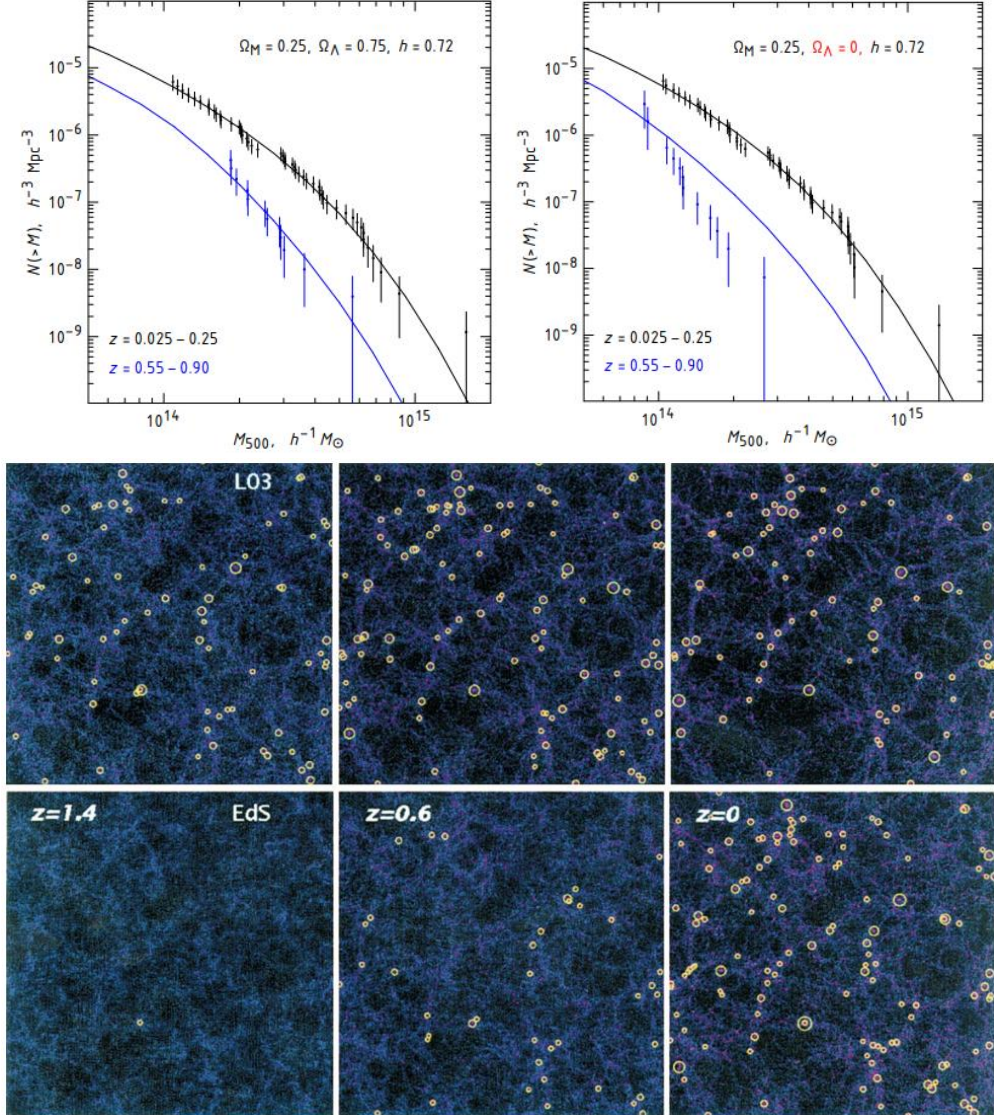


Figure 4: *Top two panels:* plots from [49] which shows how the measured mass distribution shown with coloured dots can fit the model prediction as a function of the cosmological model. XMM-Newton results are consistent with a Λ CDM model at all redshift and with an Einstein-De Sitter model just for smaller values of z , as shown in the left and right top panel, respectively. *Bottom panels:* dark matter distribution as predicted by cosmological simulations [7] at different redshifts (horizontal) and with different cosmological model (top and bottom). The number of yellow circles represent nodes on the cosmic web in which galaxy cluster formed and it is clear how the models predicted different results. The two picture above are different representation of the same concept: the link between the number mass distribution of clusters at different redshift to the cosmological model of the universe.

Ω_m and Ω_Λ are not the only cosmological parameter that can be studied with the observation of galaxy clusters. Below we will talk about the role of σ_8 , which is linked to the size of the mass perturbation from which clusters originally formed. In the project discussion, we will also take into consideration as a cosmological constraint the clusters' gas fraction f_{gas} , which is linked to the universal baryonic fraction Ω_b/Ω_m , because as these objects are baryonic matter is mostly formed by gas, we can say that in their outermost and most relaxed region, further from their gravitational potential and any merging activities, their composition must be close to the universe's.

1.2.2 Observational properties and mass estimates

Being at the nodes of the cosmic web means most galaxy clusters are still being injected by large quantities of low-density clumps and blobs of gas through the dark matter filaments and this would make us reasonably assume their outer region are particularly affected by turbulent processes linked to these continuous merging activities.

This was just predicted and at the moment we have only one image from X-ray deep observations of the region between a galaxy cluster and the closest part of a filament injecting matter into it, thanks to the work of Eckert et al. published on Nature in 2015¹².

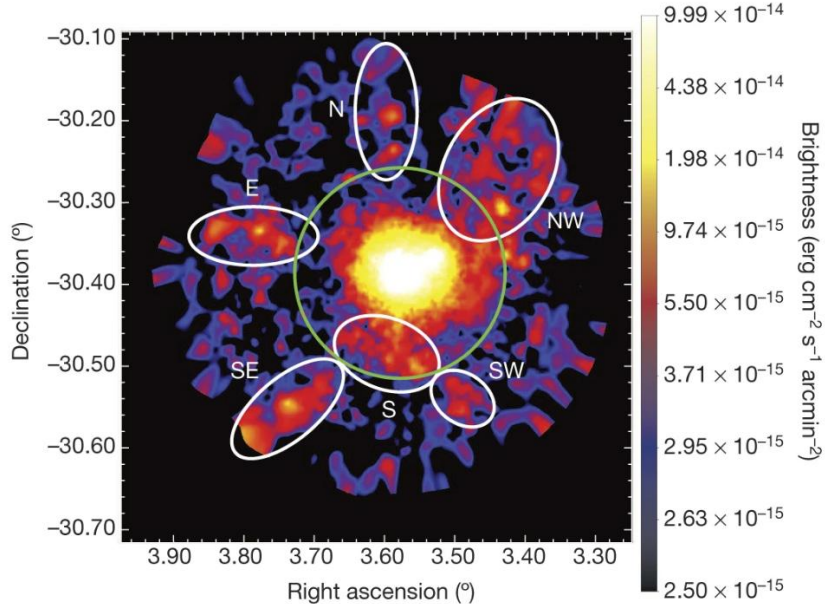


Figure 5: The X-ray brightness map of Abell 2247 taken with XMM-Newton/EPIC from [16] in which the filaments around a galaxy cluster highlighted with white circles were visible for the first time. This is the only case where the filaments are directly visible in X-ray.

¹²see [16]

At the moment the three main ways with which we can observe or measure galaxy cluster properties are **X-ray observation**, **weak gravitational lensing** in optical/UV and the measurement of the **Sunyaev-Zel'Dovic (SZ) effect** in the microwaves.

Figure 6 shows two example of composite images produced overlapping multiwavelenght observations of the same clusters.

X-rays The X-ray observation of galaxy clusters is the main topic of this thesis and in its next section about X-ray astronomy and data analysis, we will extensively explain the relation between the x-ray brightness and spectral profile to the clusters' total masses and temperature.

What is important to remember is that the ICM is gas so hot its particles emit light through **thermal Bremsstrahlung** processes and we can use its properties to measure the clusters' **mass radial profile** under the hypothesis of them being in HE.

Galaxy clusters are the brightest X-ray emitting object in the local universe and are clearly visible in the lightwave interval between $0.1 \sim 10 \text{ keV}$.

Optical/UV In the realm of optical and UV light, derive the presence of galaxy clusters through their deflection of the light emitted by sources behind them. This effect, described by general relativity links the deflection angle with the mass within a volume it passes reaching our telescopes. The greatest power of this effect is that it let us directly measure cluster masses with no assumptions on their structure, composition or dynamical state.

We can achieve very precise mass measurement with the use of weak lensing, but it does not give us other information on the clusters and it requires to have behind them a luminous source at a higher redshift of which we see the deflected light. This is not always the case for many clusters.

In the optical/UV band, we can also try to observe clusters by the analysis of the **dynamics** of the galaxies forming them. Problem is that it is hard to localize with no prior information which objects are gravitating around the same potential, while in the X-rays we would see the luminous ICM surrounding them. Furthermore, even at lower redshifts, it is often impossible to distinguish single galaxies or even groups of galaxies with their dynamics and at higher redshifts, the measure of their position and speed requires many cosmological considerations by us, which make the process even more complicated.

Microwaves For what concerns the microwaves, **SZ effects** is the energy boost which the CMB spectrum receive when its photons pass through a dense mass region in the sky, such as a galaxy cluster, and they are scattered with a series of inverse Compton processes with the highly energetic electrons of the hot ICM.

Because it is caused by scattering rather than an emission, the SZ effect scale with the clusters' density but not with their redshift, contrary to the case of X-ray brightness, which is affected by the many cosmological redshift effects, and they also decrease with the square distance of the sources from us. We can only observe the emission from the most bright sources, but we can build a number mass distribution of clusters at any redshift through the measurement of the SZ effect. The only problem with this, as we will explain later, is that the SZ effect scale with the cluster density, but to measure their masses, a relation that links the CMB perturbation to the cluster size is needed as a calibration.

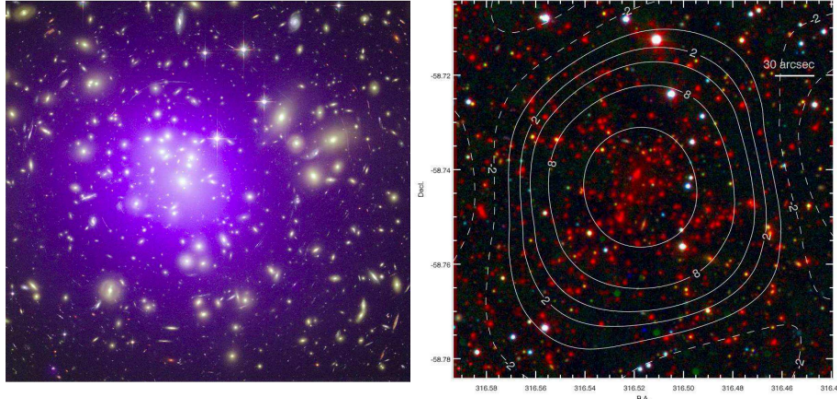


Figure 6: *Left panel:* composite X-ray/optical image of the galaxy cluster Abell 1689 ($z=0.18$). In purple is shown the $10^8 K$ gas X-ray emission as seen from the *Chandra* Observatory, while in yellow are shown optical images of galaxies as seen with the Hubble Space Telescope. The elongated arcs are effects of the optical lensing of galaxies behind the cluster caused by the matter within it. *Right panel:* is shown the composite optical/IR image of SPT-CL J2106-5844 ($z=1.133$), the largest galaxy cluster ever observed at $z > 1$ through the SZ effect. The images are from Magellan/LDSS3 (optical) and Spitzer/IRAC (Mid-IR). White contours correspond to the South Pole Telescope SZ significance values (dashed contours correspond to negative values). Source [21].

1.3 The tension with the Planck CMB

Since the end of the **Planck Surveyor telescope** mission in 2013, the vast collaboration of scientists who worked on it analyzed the data it produced with increasing precision, publishing dozens of papers each year in which many different aspects of the CMB map and its properties were discussed.

Regarding the cosmological parameters estimates which they obtained, often measuring the same quantities with different CMB observables, they found an overall excellent consistency with the predictions of a Λ CDM cosmological model and data from other experiments.

The only two areas of tensions they found in their first results from 2013 were linked to the Lyman- α BAO measurement at high redshifts¹³ and to σ_8/Ω_m relation when derived from the CMB power spectrum anisotropy and the measurement of SZ effect through galaxy clusters. Both of these observations are particularly articulate and depend on many parameters which might suffer degeneracies between them, but only the latter yet today still presents a $2 - 3\sigma$ discrepancy.

σ_8 is a parameter linked to the distribution of matter before recombination, which influenced the subsequent structure formation process and forms a direct link between the observed properties of CMB to the properties of the actual galaxy clusters. It is defined as the RMS of density fluctuations in the CMB power spectrum within a comoving spherical volume of radius 8 Mpc :

$$\frac{\delta M}{M} = \sigma(M) \equiv \sigma_8 \left(\frac{M}{M_8} \right)^{-(3+n)/6} \quad (5)$$

with $M_8 = 4\pi\bar{\rho}(8 h^{-1} Mpc)^3/3$, $n \simeq 0.97 \pm 0.01$ and $\sigma_8 \sim 0.7 - 0.9$.

It can be derived directly with a degeneration with Ω_m , which can be measured in many other different ways, such as counting the number mass distribution of clusters as we already said.

¹³see section 5.2 of [32] for an extensive explanation

This kind of spectral measurement is derived with a complex Fourier anti-transformation of the map intensity fluctuation into spherical harmonics with a long series of physical parameters dependencies on each of its coefficients. It is a computationally difficult problem, but our current knowledge of the power spectrum series expansion is calibrated to a high degree of precision.

The measure of σ_8 from the observation of the SZ effect is based on the fact that if we know the mass of the galaxy clusters in which through the CMB radiation undergo numerous inverse Compton scattering, we can correlate its *Compton y parameter* to the CMB flux of photons which undergo the scattering. Its fluctuation and deviation are then used to constraint σ_8 and Ω_m .

What the Planck collaboration found out from its data is a series of astonishingly coherent results, compatible with a Λ CDM cosmological model, but with a strong incompatibility between two estimates of the same cosmological parameter, linked to early universe structures' mass. This was not solved with three subsequent series of analyses on the CMB data¹⁴, taking into account a large range of effects both observational and physical¹⁵, all the possible degeneracies and comparisons with other instrument results.

This is a current unresolved problem of modern cosmology, which might be a lead to a technical and computational revolution or into new unexplored physical concepts we have not discovered yet.

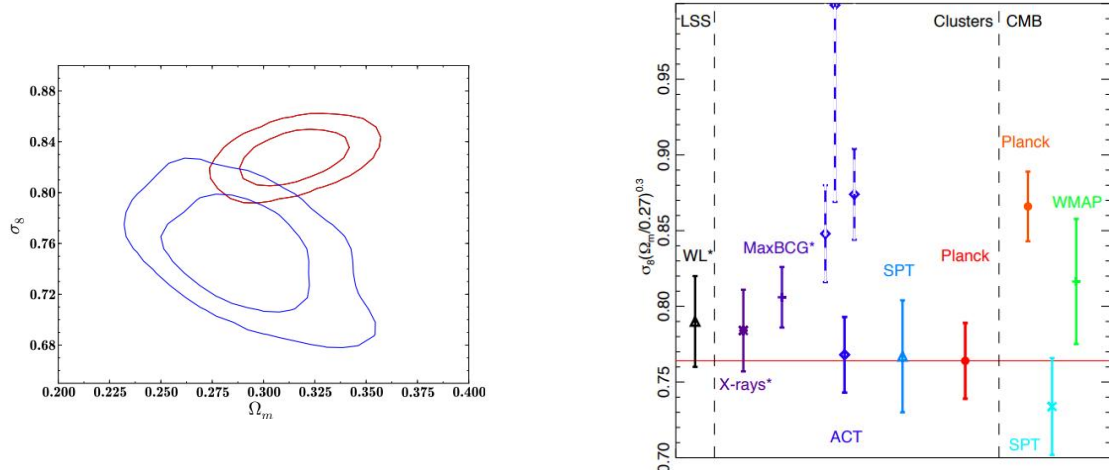


Figure 7: *Left panel:* likelihood contour at 68% and 95% for the measurement from CMB power-spectra (in red) and SZ effect (in blue)¹⁶. *Right panel:* comparison of 68% confidence intervals for σ_8 constraints from many experiments of large-scale structure, galaxy clusters mass measurement and CMB power-spectrum analysis. Credits: [31]

¹⁴Again, see for example [31], [32] and [33]

¹⁵For example considerations from [43] constrained the tension to a still high value of $\sim 2.6\sigma$

¹⁶To be precise, the blue line is also constrained with consideration linked to BAO measurement and BBN theory and it has a degeneracy on the hydrostatic correction ($1 - b$) between 0.7 and 1.

1.4 The problem with X-Ray Mass

In this subsection I will connect the dots I draw within this introduction to explain what is the scientific open issue we want to address with this project, which is the measure of galaxy cluster masses in X-ray.

Plank's σ_8 tension and X-ray masses This might not sound evident, but a possible solution to the tension on the σ_8 estimates found with Planck could be linked to how we measure galaxy clusters' masses in X-ray.

If we assume that there are no major issues with the mass fluctuation measurement based on the CMB power-spectrum analysis¹⁷, the only major factor that could justify a large correction to our SZ estimates would be linked to how we calibrate the relation that links the observed energy boost from inverse Compton scatterings to the clusters' masses.

The scaling relation between the CMB flux and the SZ effect is calibrated with their mass measurement from X-ray observations. In the next section of the thesis we will further explore how this is derived, but for now is sufficient to know X-ray cluster mass measurements come from their Bremsstrahlung brightness, which scales with their squared distance from us and with redshift. This makes it particularly hard for us to observe in X-ray these objects at larger redshifts, namely cosmological dimming. Moreover, we already saw how their brightness radial profile steadily decreases from their centre to their outer regions and we cannot directly observe them with our actual instruments such as the *Chandra* and *XMM-Newton* observatories.

HE is generally not a valid assumption, for the most perturbed clusters with complex dynamics, but our actual observation up to R_{500} did not find any major discrepancy from this value, for them. One possible way we might be miscalculating galaxy cluster mass other than the X-ray observation intrinsic difficulties above mentioned is that the HE might be violated, especially in their still unseen outer regions, in which we expect the interaction of gas clumps and substructures falling through the cosmic web filaments to the central region of the core to be linked to a turbulent motion of the ICM which would provide a non-thermal pressure term to the equation.

Why X-ray masses One might wonder the reason why we used for this calibration the indirect and complicated X-ray mass measurement and not direct measures such as that derived with lensing or something different like the dynamical analysis of stars and galaxies in the clusters' potentials. The reasons are multiple and are all linked to the intrinsic weaknesses of these methods.

When calibrating the Sunyaev-Zel'dovich effect y -parameter we're mainly interested in the gas density, as DM does not interact with light and the only possible targets for the inverse Compton processes are free electrons from the ICM. Weak gravitational lensing and the dynamical study of galaxies might directly measure the total mass in the cluster through its gravitational potential but cannot give us information on the clusters' gas fraction and their radial density profile, which can only be derived from the analysis of their Bremsstrahlung brightness profiles in X-ray. There is no way to derive the gas fraction and thus derive the gas density from the total cluster mass, without additional hypotheses on the physics of clusters.

For what concern lensing and the optical/UV observation of clusters, we also have to keep in mind that even if in the future we will have available thousands of weak lensing mass measures thanks to missions like **Euclid**, we already mentioned that not every object has behind it a source bright enough to let us accomplish lensing measurement of its mass, especially at higher redshift when bright sources become rarer. Moreover, as X-ray observations both lensing measurement and dynamical analysis are limited at higher redshift by the brightness of their sources and the observation of single galaxies or stars is impossible at a

¹⁷This is an educated guess, but it is not unjustified. We have to remember that many parameter estimates based on CMB are coherent between themselves and with a Λ CDM model and that deriving σ_8 and Ω_m directly from the power spectral analysis is a simpler task. Nonetheless, we should not consider this assumption to be correct without some other considerations and analyses.

higher distance, where they cannot be resolved singularly and our cosmological proper distance definition become relevant to their velocity measurement.

These arguments serve the purpose of exemplifying how the X-ray observation of galaxy clusters is a fundamental way of deriving their physical properties, which as we already said, is one of our most important cosmological probes for the large-scale structure of the universe as it today and as it was in the past¹⁸ and cannot simply be replaced by other kind of observations.

Are X-ray masses incorrect? Numerical simulations estimated in recent years the plausible non-thermal pressure term we might expect for the outer regions of clusters to be in the order of 5 – 20% of its total HE pressure support, as shown in the *left panel* of **Figure 8**, from [15]. This effect alone would not be sufficient to justify the correction needed to reduce Planck’s tension below 1σ .

Many numerical studies¹⁹ compared the ratio between mass estimates coming from weak gravitational lensing and X-rays, all finding a systematic underestimation in the X-ray masses under the hypothesis of HE around $\sim 15\%$.

This might seem another proof of an eventual issue with the only X-ray masses, but other research on weak lensing results²⁰ eventually found out that this **hydrostatic bias** with X-ray was not sufficient to justify Planck’s tension, which would have required a $25 \sim 30\%$ correction. An example is shown in the *right panel* of **Figure 8**, from [17].

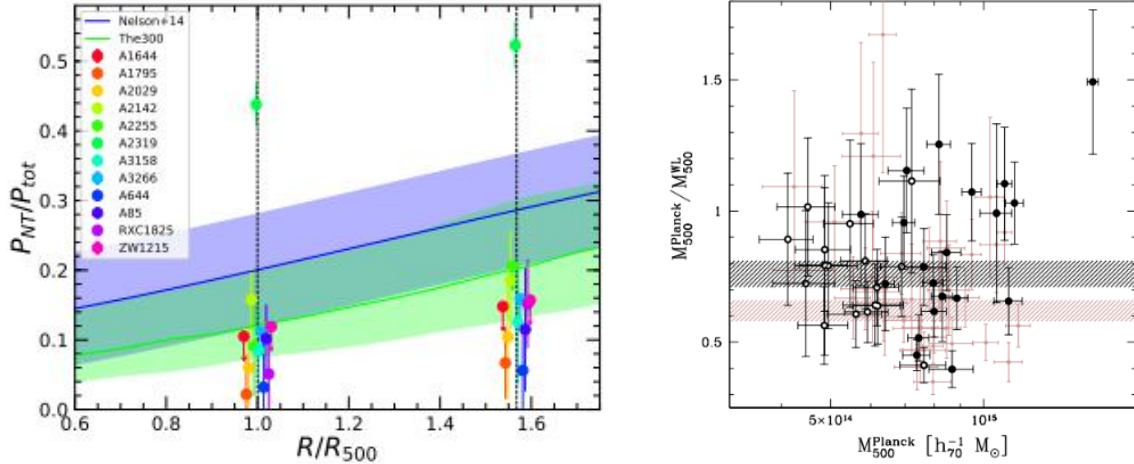


Figure 8: On the LEFT a plot from [15] shows the ratio between the predicted non-thermical pressure support term and the total pressure for a series of galaxy clusters at R_{500} and R_{200} . The two bands are the mean non-thermal pressure ratio predicted by two different numerical simulations from two works of Nelson and Rasia. On the RIGHT a plot from [17] in which the weak lensing mass eastimates at M_{500} from the CCCP collaboration are compared to the mass estimates from Planck SZ analysis, derived through a calibration based on the X-ray galaxy clusters’ mass estimates.

¹⁸An example of recent large scale research on this topic is found for example in the two works from 2021 from the DES collaboration [13] and [14]

¹⁹For example see the works of Rasia et al. [40], Nagai et al. [24] and Reiprich et al. [41]

²⁰For example see the results from the CCCP [17] and WCP [23] collaborations

This bias with lensing introduces another issue. For filling this mass gap with lensing estimates only with a hydrostatic correction while also compensating for the σ_8 tension from Planck, it would not only be required to add other pressure terms to the hydrostatic equilibrium equation or take into consideration some other dynamical correction. We would need to add a large fraction of baryonic mass, in contrast with our cosmological estimate for the **baryonic fraction** $\Omega_b/\Omega_m \sim 0.16 \pm 0.04$.

We're not sure of how large-scale structures such as galaxy clusters, of which properties have been proved to be linked to the cosmological parameters, could have divergent properties with them, at least in their outer regions. We expect future telescopes such as Athena, which will be able to calculate the gas fraction of clusters in their outer regions, will also get us closer to the answer to this apparent issue.

Some modern research, such as the last works from Dominique Eckert, tried to derive cluster masses in X-ray keeping their gas fraction ratio to the cosmological baryonic fraction as a constraint, to explore how their profiles could change supposing they behave as reliable cosmological probes.

Summary

The scientific objective: galaxy clusters represent the ultimate manifestation of large scale structure formation, and for this reason, they are tightly connected with the Universe's fundamental properties. We can leverage them as cosmological probes only if we can determine their mass precisely and correctly. Later studies have shown that is not the case, and their mass determination represents a still open question for the scientific community. In the next years, there will be available to us large data sets from new X-ray all-sky surveys, like **eRosita** and we will also obtain numerous mass estimates through weak-lensing optical observations thanks to the **Euclid project** or **LSST**. The possibility to simulate a large number of clusters observations in the function of their properties, the observation conditions and our telescopes features with advance will grant us the possibility to preview what physical insight we might expect to find, and constraint our estimates on the hydrostatic bias for future research.

The method: X-rays represent a powerful tool to determine the mass of the cluster, adopting the assumption of the hydrostatic equilibrium with the gravitational well. The validity of this assumption is crucial for any study envisaging to use clusters as cosmological tools. Despite the interest in this subject, it has been tested for local and relaxed clusters, focusing on the central parts because these objects and regions are easy to observe. Only future missions such as Athena will deliver the statistic necessary to extend these studies in the outskirts. This thesis work is concentrated on testing our capability of investigating this matter with the use of the Athena WFI instrument by simulating the observation of simulated clusters.

The results: We obtained two major results with this work. The first one is of technical nature. We were able to prepare and provide freely to the community a pipeline capable of starting from simple inputs such as temperature and brightness maps and performing a full typical X-ray analysis leading to the extraction of the HE mass profile. The measurements performed using our pipeline have a fiducial systematic of 6%, due to the current limitations of the Athena ray-tracing simulator. Furthermore, we were able to measure the HE mass of the simulated cluster up to R_{500} with limited exposure time stating the power of the Athena WFI instrument within the optics of studying thousands of objects. Finally, using these results we were able to confirm the emerging picture that the X-ray HE is affected by a systematic in the order of 10%. This strongly supports the fact that the tension found by Planck is not due to X-ray biased mass estimates.

2 Data analysis

In this second section of the thesis, I give a full picture of the topics linked to the X-ray observation of galaxy clusters and the estimate of their mass in this bandwidth under the hypothesis of hydrostatic equilibrium.

I firstly describe X-ray astronomy in general, with its peculiar datasets and limitations, to then talk about the properties of the currently active space observatories, *Chandra* and XMM-Newton and compare them to those of the soon-to-be-built Athena space telescope.

The role of Bremsstrahlung emissivity In the case of ICM, we're dealing with a gas mostly formed of hydrogen inside a large gravitational potential. This grants it a temperature high enough to be ionized into the almost same proportion of electrons and protons ($n_e \sim n_p$) and to emit radiation as **Bremsstrahlung**, which is the process linked to free-free interactions.

Its emissivity is proportional to the square of the density and has an exponential cut-off depending on their temperature:

$$\epsilon_{\nu}^{ff} = \frac{2^5 \pi e^6}{3m_e c^3} \left(\frac{2\pi}{3m_e k} \right)^{1/2} n_e^2 T^{-1/2} \exp(-h\nu/kT) \sum_i Z_i^2 n_i \bar{g}_{ff}(Z_i, T, \nu) \quad (6)$$

The latter part of this expression, including the Gaunt factor \bar{g}_{ff} , is just a function of the gas composition and it can all be reduced to numerical values.

Bremsstrahlung emissivity being more intense for less massive particles, we can consider it to be concerned only to photon-electron interactions. Typically in the central regions of clusters, we can expect values for the gas density in the order of $\sim 10^{-2} \text{ cm}^{-3}$, while in their outer regions this might reach values 2 order of magnitudes below. This steep ratio exemplifies why the outer regions of clusters are less likely to be seen and why we did not see the thin, and hence faint, substructures and clumps falling into them from the cosmic web.

Under the hypothesis of HE for the gas, we can correlate its emissivity in the X-rays to a measure of its **temperature** through a spectral fit of its exponential cut-off²¹ and we can correlate it to its **density** by a measure of its **radial brightness** $I_{\nu}(r)$, which scales with $n_e^2(r)$:

$$I_{\nu}(b) = \int_{b^2}^{\infty} dr^2 \frac{\epsilon_{\nu}(r)}{\sqrt{r^2 - b^2}} \quad (7)$$

$$\epsilon_{\nu}(r) = \frac{1}{2\pi r} \frac{d}{dr} \int_{r^2}^{\infty} dr^2 \frac{I_{\nu}(b)}{\sqrt{b^2 - r^2}} \quad (8)$$

2.1 X-ray Observations

Space-based **X-ray astronomy** was born in the 1960s when the VELA observatories, a series of satellites mounting X-ray and gamma detectors built by the US to monitor soviet possible nuclear activities, discovered a plethora of highly luminous X-ray emitting sources in the space we did never see before from Earth because of the atmosphere barrier, such as gamma-ray bursts, active galactic nuclei, Seyfert stars, black-holes' accretion disks' emission and the huge and bright conglomerate of hot gas and dark matter we now call **galaxy clusters**.

Since then, many X-ray missions have been launched and many technological leaps have been made, but we can say that X-ray telescopes are still all based on **grazing incidence detectors**, built as a series of

²¹In future, possibly with X-IFU, we will have a high enough spectral resolution in X-ray spectrometer that we will able to measure cluster temperatures from their emission lines width, which increase with the gas particles velocity dispersion, and hence their average kinetic energy and temperature.

concentric parabolic and hyperbolic mirrors on which light is reflected the same focal point through Fresnel Law. The use of mirrors is needed because of the high-penetration of high-energy ionizing radiation such as the X-rays, within $\sim 0.1 \text{ keV}$ and $\sim 100 \text{ keV}$.

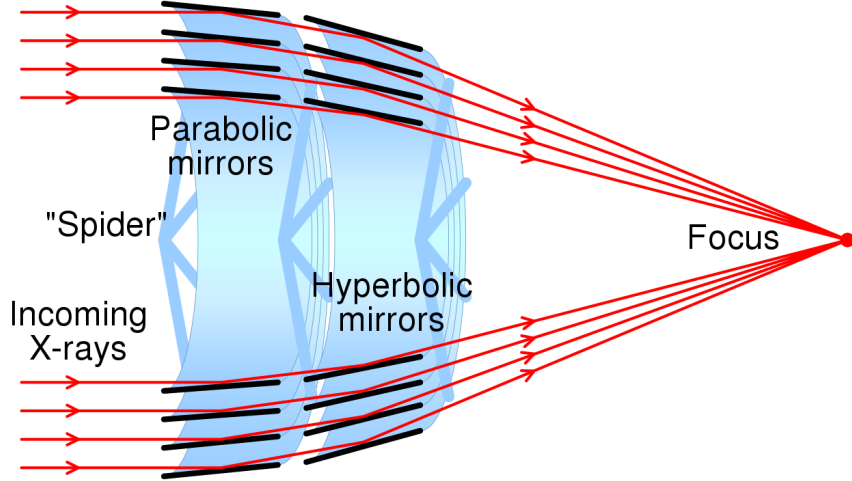


Figure 9: Simple scheme showing how a system of concentric mirror can reflect high-energy photons into a single point.

Spectro-imaging datasets When photons reach a sensor their position and energy is recorded at the same time, in a so-called **spectro-imaging** process. This is completely different from the case of optical-UV observations, for which to measure photons' energy they have to be deflected through a prism or grating.

On the other hand, the weakness of spectro-imaging are that:

- its position measurement accuracy is highly dependant on the mirror construction and condition and our knowledge of them in real-time and is typically lower than optical-UV's.
- The number of counts from outside the instruments are strongly dependent on the radial distance of detections from the focal point position.

In particular, the reduction of the observed brightness getting closer to the image edges is what we call **vignetting**. This effect is compensated by dividing images by their exposition time maps and considering the satellite dithering movement during the observation.

Because of the nature of these observations and the relative sparsity of X-ray photons, typical observation datasets in this band take the form of an event file table, containing information on each observed photon position, energy and time of arrival and globally describing their spatial density distribution.

Observation Components In general, a typical X-ray observation of an extended source such as galaxy clusters collect photons from four main components: the **source**, eventual **point-like sources** surrounding it, **background** emission from each unresolved source in the **sky**, which we can see at every position and finally the **instrumental background** emission, also referred to as particle background, formed of photons which did not pass through the instrument mirrors, but have been generated by different means.

For example, the latter observations might come from high-energy particles that our CCDs detect as photons or photons emitted through fluorescence by the telescope component, which might be excited from interaction with high-energy particles.

In the next section, in which the simulation pipeline will be described, we will see what each component's spectra and brightness profiles look like and how they are affected by the instrumental calibration files and vignetting effect.

2.1.1 X-ray calibration files

When comparing observations from different instruments or derived with different settings, the way we can describe the influence of the observational apparatus on the datasets is through the use of so-called **instrument calibration files**. These are a large variety of tables, typically containing spectral information derived from direct analysis of the detector before launching them. They might change with time also because of any kind of deterioration or damage the observatories might intercourse during their development.

The two major factors we've found ourselves interested in the development of a simulation and analysis pipeline for X-ray images were the **point-spread function (PSF)**, **auxiliary response file (ARF)** and, to a minor extent for our purposes, the **response file matrix (RMF)**.

PSF The PSF calibration files contain a series of tables indicating how the light from a single point-like source is convoluted between near pixels on the image. It directly affects the counts measured in each radial bin both for the brightness profile and temperature profile derived from spectra.

Typically it can be fitted with a series of analytical expressions with the form of bell-shaped functions, such as a Gaussian or King function with increasing width further from the image centre.

Effective area calibrations An important parameter in astronomy is the so-called **effective area**, which describe the ratio between the observed radiation power by the instrument and its real power flux density as a function of the energy band. This is connected to the observed energy spectrum and brightness profiles.

In the case of X-ray astronomy, effective areas are typically strong functions of the energy and can vary with time, as shown in the example below.

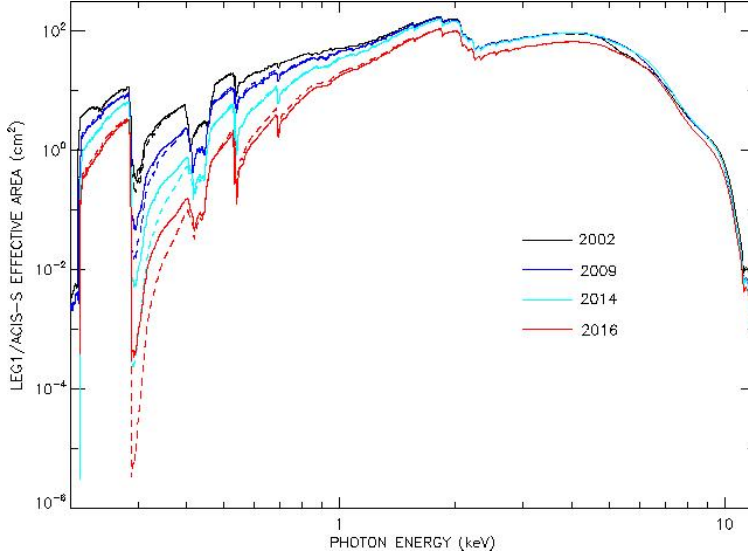


Figure 10: Here is shown as an example the effective area for Chandra AXIS-S as a function of energy. Thisplot also shows how it deteriorated with time.

ARF and RMF are two of the instrumental calibration files connected with an observatory's effective area:

$$([S_{obs}] \otimes RMF) \times ARF \quad (9)$$

ARF contains the spectral response of the instrument. It folds mirror effects such as the loss of efficiency at high energy and the presence of absorption material deposited on the telescope. This file is essential for our analysis because it affects the spectrum shape, which we use to determine the temperature of the cluster.

RMF contains information on how the energy of the photons is redistributed due to instrumental limitation. We can improve the energy resolution of the instrument by using this file.

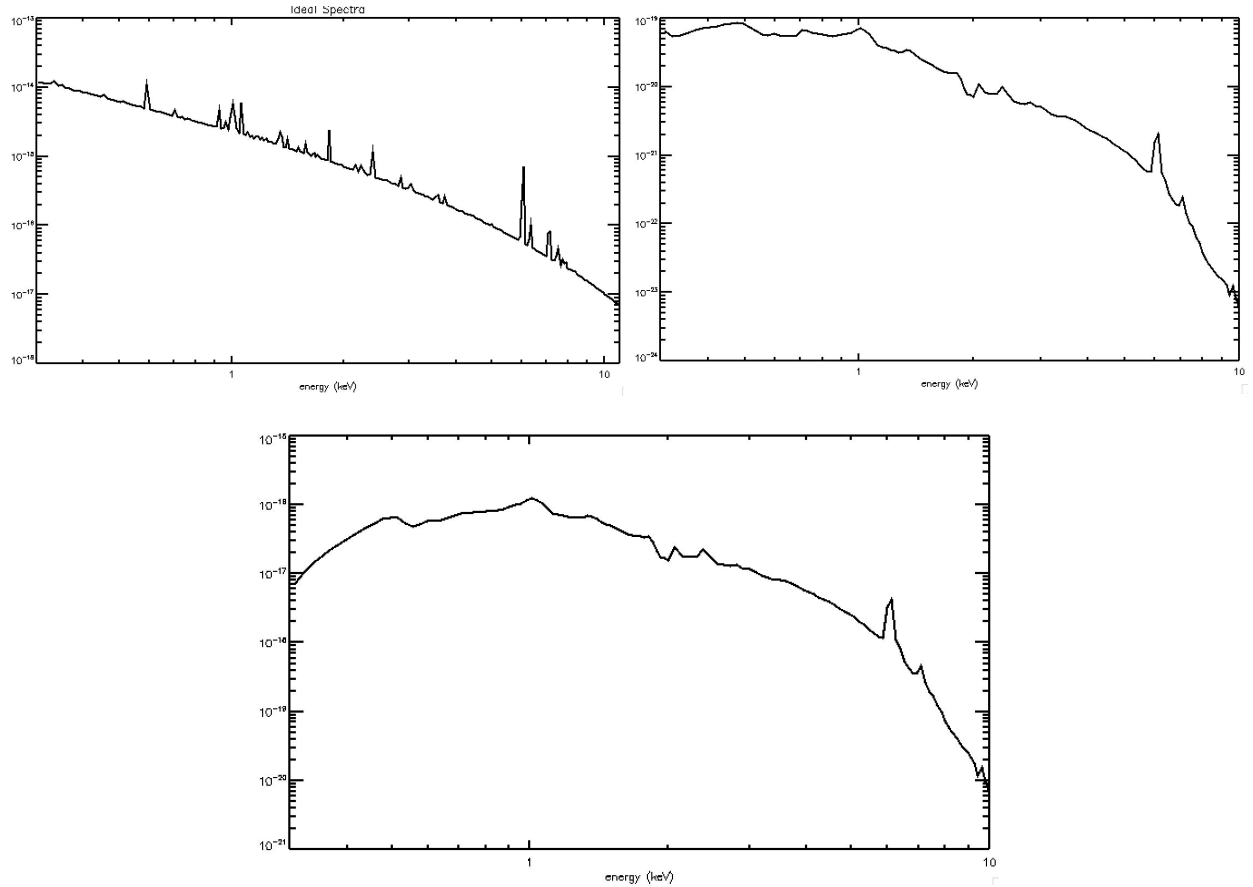


Figure 11: *Top panels:* On the left is shown an example of energy spectrum we might expect a cluster to emits. On the right it has been convoluted with Chandra's RMF. *Bottom panel:* The observed spectrum, found convolving it for the RMF and then multiplying it for the ARF.

2.2 X-ray telescopes

In the field of galaxy clusters astronomy, the two most recent and active instruments are the *Chandra* X-ray Observatory and *XMM-Newton*, both launched in 1999 respectively from NASA and from ESA and both expected to retire within the next 10 years.

These two telescopes are based on the same kind of technologies, with different fields of applications because of their different characteristics, which make them particularly useful when their observations are combined and used together.

2.2.1 *Chandra* and *XMM-Newton*

In particular, for our analysis, we used Chandra observations as a reference for calibrating our simulation pipeline, but it is interesting to compare its characteristics to those of *XMM-Newton*:

- Chandra has an higher resolution of around $\sim 0.5''$ and smaller field of view radius of $\sim 16'$ and effective area $200\text{ cm}^2 @ 1\text{ keV}$
- *XMM-Newton* on the contrary has lower resolution $\sim 10''$ and larger field of view $\sim 30'$ and effective area $\sim 10^3\text{ cm}^2 @ 1\text{ keV}$

These properties make *Chandra* observations more suitable for detailed analysis of the central region of clusters, while *XMM-Newton* can observe with lower resolution their overall figure thanks to its larger field of view and capability of measuring larger fluxes. This can be appreciated from **Figure 12**, where we can see that the *Chandra* images on the right can retrieve the details of the cluster ICM distribution. On the other hand, *XMM-Newton* can detect cluster emission up to 3 times *Chandra*, as visible from the isophotes.

2.2.2 *Athena+*

Chandra and *XMM-Newton* made us obtain outstanding results regarding the observation of the more bright and dense inner regions of clusters, giving us precise results regarding their inner mass, gas fraction and dynamics.

Their current limitations are that their effective area did not prove to be high enough to observe the faint and thinner outer regions of clusters, in which we think we might find interesting physical outcomes related to cosmology and our understanding of the dynamics of the cosmic web. Today our observational limit for clusters is around their R_{500} . This is not enough to make assumptions on their total mass without the hypothesis of HE.

Moreover, both these instruments suffer from rapidly degenerating PSF, which increases so much, close to their sensors' edges, it does not make it possible for us to distinguish a point-like source PSF from an actual large clump or substructure eventually surrounding the central part of clusters.

We expect most of these difficulties will be overcome by ESA's next X-ray telescope, **Athena**²², which is expected to be launched around ~ 2030 and is now in its final phase of development.

Athena will mount two instruments, namely the **Wide-Field Imager (WFI)** and its spectrometer **X-ray Integral Field Unit (X-IFU)**, which will both boasts crossing-edge performances and technologies. In this thesis, I developed a pipeline for simulating WFI images of galaxy clusters and predicting their possible results, also comparing them to those of Chandra.

Our actual estimates²³ predict that WFI will have a field of view of around $30'$ -squared, and angular resolution in the order of $5''$ on-axis and $\sim 10''$ at a $25'$ radius. This is not as high as Chandra's, which we

²²As a reference for the actual Athena structure and expected results, we can refer to the white-paper being updated by Planck institute and ESA at [25]

²³Being the instruments all still being developed, these value might change with time for better or worse

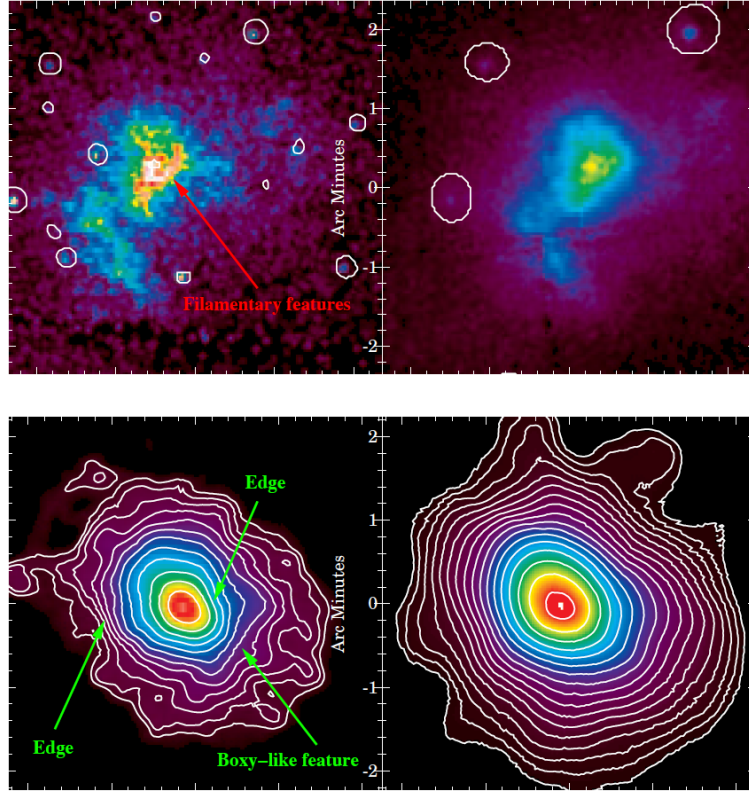


Figure 12: *Top panels:* Images in the [0.5-2.5] keV band of the same galaxy clusters at $z + 0.55$ observed with *Chandra* and *XMM-Newton* on the left and right panel, respectively. *Bottom panels:* same as the top panels but for the cluster CI0016+16. Withe contours represent the isophotes. For all pictures, the white cicle identify the point sources.

might still consider the best instrument for analyzing clusters in central regions. Again, remember us all those observatories are best suited for different kinds of observations and could always be used together.

The best performances we can expect from WFI are anyhow connected to its high effective area of around $10^4 \text{ cm}^2 @ 1 \text{ keV}$, 10 times larger than XMM-Newton's. Together its large field of view and with X-IFU incredible spectral resolution of around $12.5 \text{ eV} @ 6 \text{ keV}$, these properties will reasonably allow us to see the emission from the less dense and fainter outer regions of clusters with high enough radial resolution to analyze their dynamics, and deriving their mass profile up to larger radii, possibly closer to R_{200} , hence making us get closer to the possibility of solving one of the most cosmological compelling issues today.

The larger effective area of WFI will also give us the possibility to observe larger amplitude brightness with much lower exposure times. At the moment an average Chandra observation of a cluster from the local universe lasts around $50 \sim 100 \text{ ksec}$ with $\sim 0.1 \text{ cts/sec}$ from clusters and $\sim 0.01 \text{ cts/sec}$ from the sky background. With WFI, we might find the same central count rates with a fraction of the exposure time between 1/5 and 1/10. This is a huge technical improvement that will grant us the possibility to analyze the many objects future X-ray all-sky surveys such as eRosita will find.

WFI will also have a very stable PSF, which il grant us the ability to discern substructures and point-like sources even near its calorimeter borders.

Figure 13 synthetize these results and show the actual potentiality of this instrument:

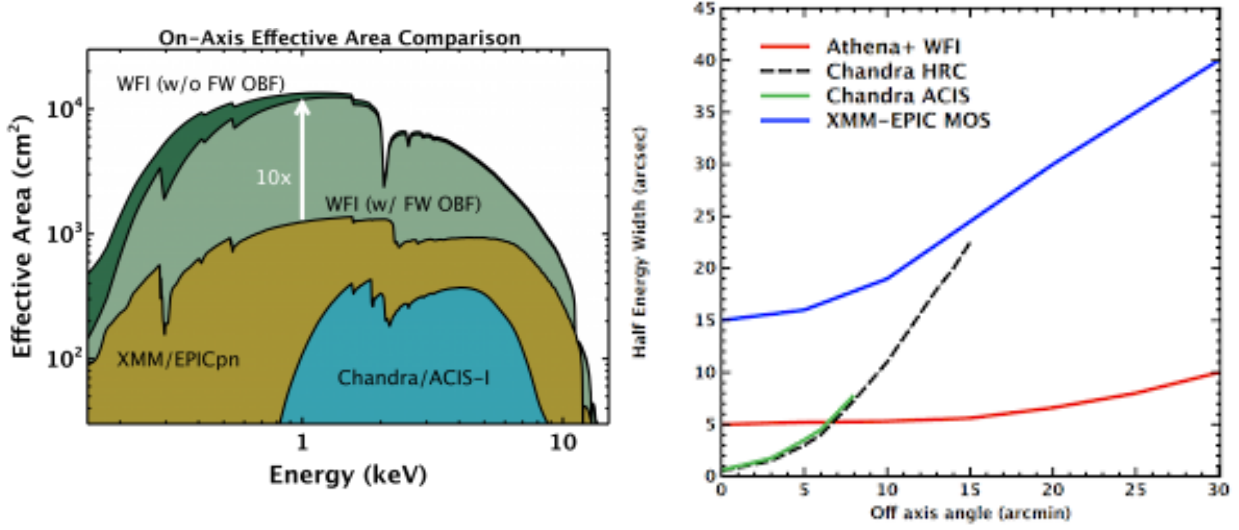


Figure 13: These two plots shows together the comparisons between WFI's, Chandra's and XMM-Newton's effective areas (*on the left* and half energy width as a function of radius, linked to the PSF (*on the right*).

These are not the only outstanding characteristics of Athena, WFI and X-IFU and I did not even try to enter in the details of their construction but can be used as a summary of their properties which are linked to the reason behind this project and that we expect the most to help us solve the problem of galaxy cluster's masses estimates in X-rays.

2.3 Mass Measurement

I briefly explain how we can estimate the **total mass** of a cluster with data from the observation of the **X-ray emission** of its gas.

It is important to understand that when dealing with a large variety of very diverse objects such as galaxy clusters, is fundamental to find the best approximation to describe all of them with the best compromise between accuracy and simplicity. In the case of X-ray mass estimates of these objects, the "spherical cow" hypotheses which have been used since their discovery are that:

- galaxy clusters are only governed by gravitational force. This is linked to their huge mass, which suggests there are no other forces with high enough amplitude to influence the clusters' properties.

This hypothesis is important because it allows us to assume clusters have the property of being **self-similar**, meaning their properties are the same at all scale radii and that two clusters with different masses might look the same in X-ray.

- That the ICM is in **HE**, which can be expressed as a function of its mass density and temperature:

$$M_{tot}(r) = -\frac{r^2}{G\rho(r)} \frac{dP}{dr} = -\frac{kT(r)r}{\mu m_p G} \left[\frac{d \ln \rho(r)}{d \ln r} + \frac{d \ln T(r)}{d \ln r} \right] \quad (10)$$

As we have previously underlined, this approximation obviously is not supposed to hold up in the case of single perturbed objects, like those undergoing merging processes, but it was found to hold up

with sufficient accuracy within our current observational limit around R_{500} . We actually expect this condition to be not valid to a certain extent, but the issue is that hydrostatic bias estimates are not sufficient to solve the clusters mass tension.

Profiles deprojection To describe the actual gas density and temperature of a 3-dimensional structure such as a galaxy cluster starting from the image of it we observe projected on the sky plane, we can both decide to fit it with a parametric profile or geometrically **deproject**.

What we see is the combined effect of the PSF and the sum of the measurement on the line of sight on the emitted signal:

$$[S_{obs}] = [R_{PSF}][R_{proj}][S_{emitted}] \quad (11)$$

Inverting this relation we can directly find the **deprojected brightness radial profile** for clusters²⁴, which we can link to their electron density at fixed temperature with tabulated functions²⁵ called $\lambda = \lambda(T, n_e)$.

Integrating our **radial gas density profile** we derive a measure for its **mass within a certain radius**:

$$M_{gas}(r) = 4\pi \int_0^r dr' \rho(r') (r')^2 \quad (12)$$

For what concern temperatures. Their functional form is too complex to be deprojected in the same way starting from spectral fit data. What we do is to fit our observed projected temperature with **analytical models** from a ground-breaking work by *Vikhlinin et al.* from 2006. From the projected fit parameters we can derive the deprojected temperature ones and hence calculate the projection matrix with which deproject the observed **temperature profile**.

$$[M_{proj}][T_{fit}^{3D}] = [T_{fit}^{2D}] \quad (13)$$

$$[M_{proj}][T_{obs}^{3D}] = [T_{obs}^{2D}] \quad (14)$$

From gas mass to total mass With the deprojected temperature and density profiles, we can then use the HE equation to derive the total mass profile of our cluster.

This is a 3-dimensional profile and we can analyze its projections in any direction.

To this point, we explained how to derive with a deep enough X-ray observation, the galaxy clusters' mass profile, but when dealing with large populations of clusters with less accurate observational data at our disposal, we might need another way to estimate the total mass profiles under the HE assumption. This is the case when dealing with data from **all-sky surveys**, which typically see a large number of clusters without analyzing each of them for a long time.

Up to now, we showed how to directly derive from the X-ray ICM brightness it's temperature and mass profile, which we know constitute a minor fraction of clusters total mass

$$M_{tot} = M_{DM} + M_{gas} + M_{gal} \sim M_{DM} + M_{gas} \quad (15)$$

The link between these and the clusters' total mass can be found again from the HE hypothesis: if clusters are virialized and only concerned by gravitational forces, we can say their total gravitational potential, which

²⁴One might note that the projection matrix is summing exponential terms from the bremsstrahlung emissivity integral, but this result would technically have a different functional form from it. Our current instruments do not have a resolution sufficient to discern this effect from the deprojection.

²⁵Here I'm skipping the fact that lambda functions link the 3-dimensional temperature profile to the 3-dimensional density profile. But it turns out that $\lambda(T_{3D}) \sim \lambda(T_{2D})$ and so we can use our measured profile for this transformation.

is proportional to their total mass, must be proportional to the thermal gas energy integrated along the line of sight. We call this quantity for the total mass the Y_X **proxy**:

$$Y_X = \int dl\rho T \propto M_{gas}T \quad (16)$$

Kravtsov, Vikhlinin and Nagai 2006²⁶ calibrated the relations between Y_X , M_{gas} and M_{tot} with the observation of particularly virialised clusters and measured it agreed within a $5 \sim 10\%$ margin to any observational and simulated data, with a low scatter of $5 \sim 7\%$ at M_{500} .

This kind of proxy which correlate a cluster mass to its observable properties has an equivalent formulation for the Sunyaev-Zel'Dovich effect, called Y_{SZ} . This can be expressed as the integral along the line of sight of the ICM energy pressure density of the gas²⁷, which is proportional to the cluster's total mass. This relation was calibrated using X-ray masses derived under the HE hypothesis and this is why Plank's tension on the σ_8 parameter was correlated to the way clusters' masses are measured through X-ray observations of the ICM.

2.4 Chandra X-ray analysis

For calibrating our WFI simulation pipeline, we compared our results to those of the ***Chandra* analysis** of its observations. For this reason, it is important to summarise how *Chandra* analysis pipeline works.

I will now refer to the pipeline for *Chandra* analysis which Dr Bartalucci gave to me and with which I reduced *Chandra* raw data directly downloaded from the telescope **public observation database**²⁸. This code was built from him using **IDL**, **XSPEC** and *Chandra* X-ray analysis Software **CIAO**²⁹.

1. After building the directory structure for the results, the pipeline proceed in the data reduction process (*chandra_repro*), with which CIAO reads the data from the input directories and build from them bad pixel files and event files, selecting the most suitable calibration files for the particular observation and calculating the particle background spectra which is saved in a .pha file.

It's interesting to note that in this part of the process, CIAO also must take into account the possibility of solar flares being observed by *Chandra* during its routine. These kinds of situations might completely corrupt an observation. This will not be an issue with Athena, because it will be launched in the Solar-Earth lagrangian point *L1*, which will be far enough from us not to see flares³⁰.

2. The next step is to remove from our event files counts from regions in which we can see point-like sources. This process is semi-automatic as CIAO gives us functions with which to locate these sources, but we might want to change these regions not to remove too many counts from our complete image.
3. Later the brightness profiles are extracted with an optimal radial distribution of bins simply by counting how many photons comes from each annulus.

From the overall profile will be subtracted the particle background, as described by the instrument calibration file and the sky-background fit from, which can be derived as the average constant brightness of the outer radii of the image, where the profile becomes invisible.

4. the next part of the pipeline find the best binning for extracting spectra from concentric circular annuli centred on the source, calculate the RMF with which convolve them in each position and then derive fit spectral fit the temperature profiles

²⁶see [20]

²⁷This is proportional to the y Compton parameter, which is directly observed from SZ analysis.

²⁸[2]

²⁹As a reference for its functions, see [10]

³⁰In the recent weeks it was proposed to launch it in *L2* instead, but this does not change my observation.

- the last part of the code deproject and calculate the radial gas density, temperature and mass profile for the source as explained in the **subsection 2.1**.

This was just a simple overlook on the analysis process for Chandra data, which can be used as a hint of how our WFI images simulation proceeded, as it had to consider bottom-up all those effects the analysis of actual data had to decompose top-down.

2.5 The role of our Pipeline

During this thesis project, I developed a **pipeline** with which produce **simulated Athena-WFI galaxy cluster images**. This took the form of a series of scripts written using different software, first of all, the ray-tracing X-ray observation simulation software SIXTE³¹.

The role of this pipeline is that of an instrument with which foreshadow the future Athena observational results in the X-ray. Working with clusters produced with controlled cosmological simulations, with known properties, we can analyze the results of our observations, for example concentrating on their radial mass profiles.

This will give us the possibility to build a base-ground knowledge on the clusters' outer regions, as a function of their properties, dynamical state and observational conditions (background, exposure time, coordinates, ...) and another way to predict the amplitude of the HE bias comparing our estimates with the known mass of simulated objects in a controlled setting.

In the next two sections of the thesis, I will go through each part of the simulation pipeline and the subsequent analysis routine I wrote in python to study its outputs, with their radial mass profiles. The fifth section will show the global results of this analysis and my considerations on the pipeline results in comparison with our theoretical expectations about the physics of clusters' outer regions and Athena WFI capabilities.

³¹see [46], [44] and [12]

3 The Pipeline

This section will be a complete and technical review of the **pipeline**, to explain each passage of the code with the support of a few simple examples.

Our main technological instrument has been **SIXTE**, a software package for X-ray telescope observation ray-tracing simulations developed at the Remeis Observatory (ECAP). It is a highly-modular suite of simulation functions based on the use of input files called **SIMPUT (SIMulation inPUT)**.

These are FITS files containing tables filled with information on the sources required to SIXTE to start a simulation. They are instrument-independent and can both describe a catalogue of any number of point-like sources or large structures as a whole. On **SIXTE manual**³², there is an extended explanation of their structure and creation.

The importance of the simulations being based on **ray-tracing** is that their results are assured to give us a realistic physical description of photons, considering their unique behaviour between the source and the observer and of its interaction with it. This is the opposite of any results in which photons are described collectively with a set of statistical assumptions or through parametrical models.

The process of learning how to use SIXTE and calibrating the results was mostly made by building bottom-up from simple case scenarios each section of the pipeline, as the software, while being already developed and completely functional does not have complete documentation yet and it is still being updated in the software and instrument files.

I will describe each part of the code starting with the simulation of a point-like source with power-law spectral emission. Furthermore, I expand each explanation describing the simulation of a complete simulation of the WFI image of a galaxy cluster made starting from a *Chandra* image or from a simulated object created using cosmological simulations.

Note on the use of different languages and software: It is important to clarify that the pipeline was built using SIXTE, with the support of a combination of scripts commonly adopted in X-ray astronomy such as **IDL**, **XSPEC**, **CIAO**, and **python** (**pyroffit** and **hydromass** above all libraries).

This differentiation was necessary because each software's peculiar function, needed to cover the numerous aspects of X-ray images simulation and data analysis, but it was made to have an instrument with the smallest number of requirements to be used and modified. In particular, I focused on keeping each part of the code completely transparent and editable in the function of the user need, while also concentrating the physical parameters of the source in the SIXTE section of the pipeline: a user who's working with WFI simulation might simply edit some part of SIXTE scripts with its source parameter, not touching the scripts linked to spectrum fit (XSPEC), input maps (CIAO and IDL) and physical analysis of the pipeline results (python).

3.1 Point-like source with Power-law emission

With this first example, I'm going to show the first step with which is possible to create a simulated image for a simple point-like object with a power-law spectral emission and how the results represented it faithfully.

3.1.1 Initializing the pipeline and XML files

The core of the pipeline works using CIAO and SIXTE. Firstly, we begin to initialise the two software and create aliases for the **XML files** position. SIXTE will use these files to locate the instrument **calibration files** for each of WFI's sensors, such as their RMF, PSF and ARF.

Below an example of XML file for one of WFI chips:

³²See as a reference the software manual available for our version of the code at [44]

```

<?xml version="1.0"?>
<instrument telescop="Athena" instrume="WFI">
<telescope>
<arf filename="athena_SIXTE_wfi_w_filter_v20190122.arf"/>
<focallength value="12.0"/>
<fov diameter="1.0"/>
<psf filename="athena_psf_15row.fits"/>
<vignetting filename="athena_vig_15row_20171016.fits"/>
<pha2pi filename="athena_wfi_ph2pi_v20190320.fits"/>
<pirmf filename="athena_wfi_pirmf_v20190320.rmf"/>
</telescope>

<detector>
<dimensions xwidth="512" ywidth="512"/>
<wcs xrpix="256.5" yrpix="256.5" x rval="−29.8e−3" y rval="−43.76e−3"
x delt="130.e−6" y delt="130.e−6" rota="90.0"/>
<depfet integration="0.8e−6" clear="0.8e−6" settling="3.7e−6" type="normal"/>
<rmf filename="athena_wfi_SIXTE_v20150504.rmf"/>
<phabackground filename="SIXTE_wfi_particle_bkg_20190829.pha"/>
<split type="GAUSS" par1="11.e−6"/>

<threshold_readout_lo_keV value="50.e−3"/>
<threshold_event_lo_keV value="50.e−3"/>
<threshold_split_lo_keV value="50.e−3"/>
<readout mode="time">
  <loop start="0" end="511" increment="1" variable="$i">
    <wait time="9.8e−6"/>
    <readoutline lineindex="$i" readoutindex="$i"/>
  </loop>
  <newframe/>
</readout>
</detector>
</instrument>

```

3.1.2 Simput Files Creation

The next step is to create a SIMPUT file for the source.

In the case of a single point-like source the parameters we're using for the creation of its SIMPUT are:

- **RA/Dec:** the source Right Ascension and Declination coordinates in degrees. The position of the source is put in a random position of the sky.
- **srcFlux:** flux of the source (intrinsic property independent of the observation, in [$erg/cm^2/sec$])
- **Emin/Emax:** a reference energy band for fluxes, between Emin and Emax
- **XSPECFile:** a model for its spectral emission (in this case an XSPEC xml file)
- **Elow/Eup/Nbins:** a spectrum energy band, between Elow and Emax with a Nbins

Below an example of the command with which create a SIMPUT file for a point-like source and the look of it:

```

punlearn simputfile
pset simputfile Elow=0.2
pset simputfile Eup=12
pset simputfile Nbins=1000
pset simputfile XSPECFile=./model.xcm
pset simputfile RA=${RA}
pset simputfile Dec=${DEC}
pset simputfile srcFlux=1.e-12
pset simputfile Emin=0.5
pset simputfile Emax=10
pset simputfile clobber=yes
simputfile

```

	SRC_ID	SRC_NAME	RA	DEC	IMGROTA	IMGSCAL	E_MIN	E_MAX	FLUX	SPECTRUM	IMAGE	TIMING
units			deg	deg	deg		keV	keV	erg/s/cm**2			
1	1		178.952651977539	23.43056488037109	0	1	0.7	2.5	1e-12	[SPECTRUM,1]	NULL	NULL

	ENERGY[]	FLUXDENSITY[]	NAME
units	keV	photon/s/cm**2/keV	
1	ENERGY[0:999]	FLUXDENSITY[0:999]	

Figure 14: The two tables in the source SIMPUT file, one referring to its parameters and one to its spectrum

3.1.3 Simulation

While there are many different functions in SIXTE that can produce a simulation for the Athena-WFI imager, I chose to only use the more specifically designed *athenawfisim* function.

This program will use information from the instrument calibration files (read from the sensors XML files) and from the SIMPUT file to produce a **simulated event file** for each telescope chip.

The parameters we modified are:

- **RA/Dec:** Pointing central value for the observation (CRVALs)
- **Prefix:** Output for the event files
- **Exposure:** Exposure time for the observation in seconds
- **Attitude:** we can use an attitude file to describe the telescope **dithering** movement, so to cover a larger portion of the sky and in particular the gaps between each chip
- **Simput:** input SIMPUT file for the source

For the **attitude**, I wrote a script in python to generate a fits file describing the satellite position around the observation central values modelled on an Athena dithering file provided by SIXTE tutorials.

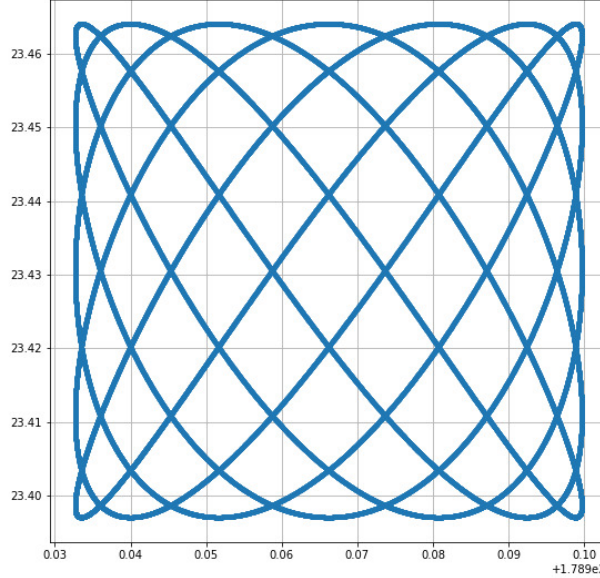


Figure 15: This plot shows an attitude file describing the dithering of the satellite around a central position

Here is an example of the command with which create a SIXTE simulation using athenawfisim:

```
punlearn athenawfisim
pset athenawfisim XMLFile0=${xml0}
pset athenawfisim XMLFile1=${xml1}
pset athenawfisim XMLFile2=${xml2}
pset athenawfisim XMLFile3=${xml3}
pset athenawfisim RA=${RA}
pset athenawfisim Dec=${DEC}
pset athenawfisim Prefix=./pnt_source_
pset athenawfisim Exposure=10000
pset athenawfisim clobber=yes
pset athenawfisim Attitude=./attitude_80ksec.att
pset athenawfisim Simput=./simput.fits
athenawfisim
```

Sidenote: The workflow of the Athena **X-IFU** Spectrometer simulation is similar to WFI and based on the *xifupipeline* SIXTE function. This is also thanks to the fact that SIMPUT files are instrument-independent.

3.1.4 Imaging

SIXTE event files are not simple to directly analyze as an image, so with this step, we produce an actual counts image of our simulation.

In particular to do this we merge the four event files created by simputmultispec with the function *ftmerge* and then create an image using the *imgev* SIXTE functions, of which we choose:

- **NAXIS:** image pixel per axis
- **CRVAL:** central value, the pointing coordinates
- **CUNIT:** CRVAL unit measure
- **CRPIX:** central pixels of the image
- **CDELT:** dimension in degrees of each pixels

To see all WFI chips, at the cost of a lower resolution, a value $\text{CDELT}=-0.0011888874248538006$ should work, while with a value of $\text{CDELT}=-6.207043e-04$ you would see the subject of your image at a higher resolution, cutting out some parts of the WFI field of view.

Below an example of the command with which an image of our source from the simulation's event file:

```
punlearn imgev
pset imgev EvtFile=./pnt_source_comb.fits
pset imgev Image=./image.fits
pset imgev NAXIS1=1078
pset imgev NAXIS2=1078
pset imgev CRVAL1=${RA}
pset imgev CRVAL2=${DEC}
pset imgev CRPIX1=593.192308
pset imgev CRPIX2=485.807692
pset imgev CUNIT1=deg
pset imgev CUNIT2=deg
pset imgev CDELT1=6.207043e-04
pset imgev CDELT2=6.207043e-04
pset imgev CoordinateSystem=0
pset imgev Projection=TAN
pset imgev clobber=yes
imgev
```

Figure 16 shows images of the point-like source with different zooms and the radial brightness of the source.

In both is clear the source was reproduced clearly, with a symmetrical point-spread function of around $2 \cdot 10^{-2} \text{ arcmin}$. It's also visible the particle and instrumental background SIXTE added to the simulation, referring to its instrumental files for the expected background spectrum and which has an almost constant brightness, slightly increasing at higher radii as expected due to vignetting.

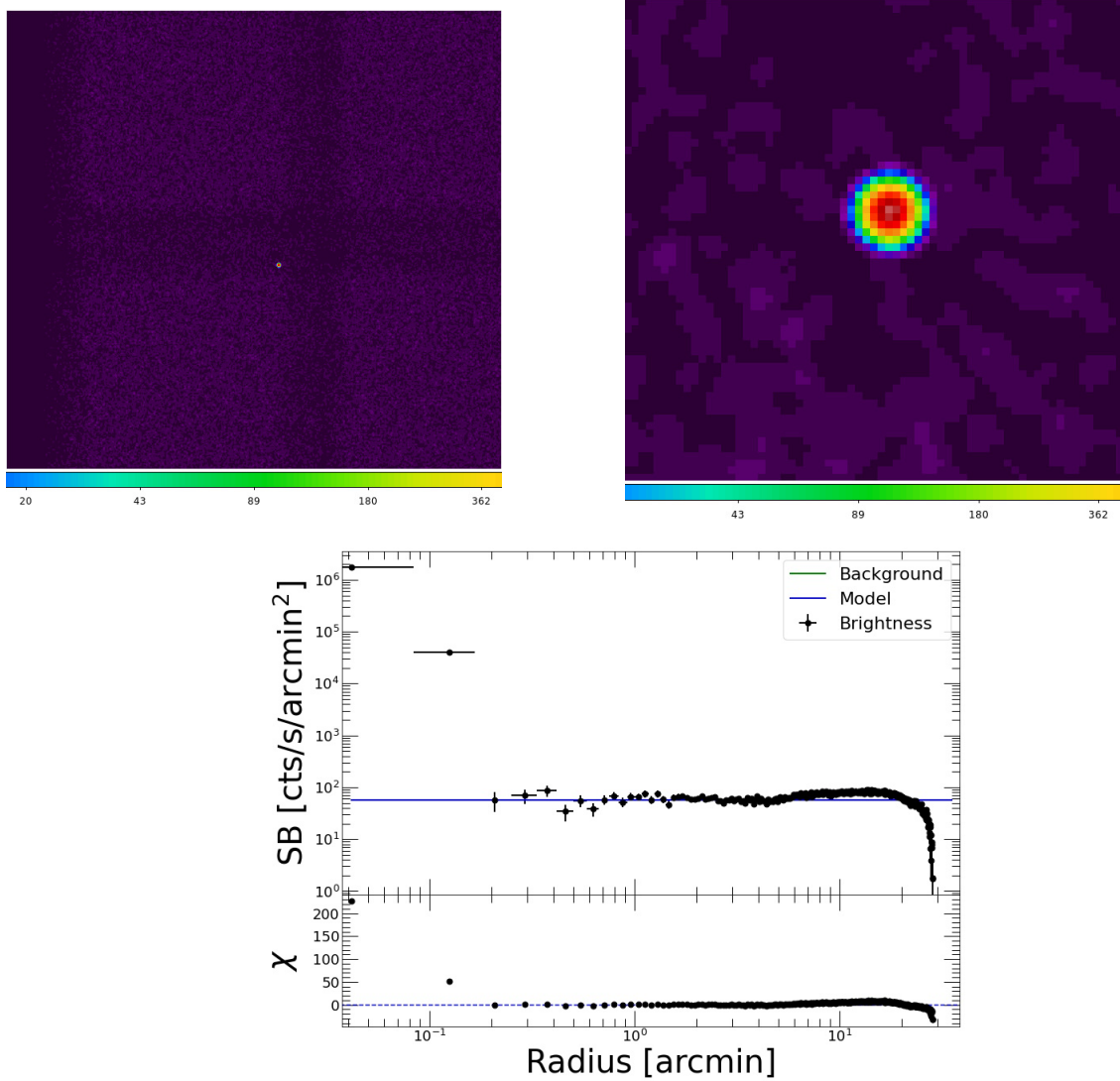


Figure 16: *Top panels:* WFI field of view of the point-like simulation and zoom on the source in the left and right panel, respectively. *Bottom panel:* radial surface brightness profile of the point-like extracted from the SIXTE simulation. We can notice the steep emission in the centre and the flat profile above 0.3 arcmin.

3.1.5 Spectra

SIXTE provides us the `makespec` function, with which is possible to extract spectra as **PHA files** given an input event file and all the instrument calibration files through the XML files directory.

It is also customary to choose any kind of filter on the event file to only extract spectra from the source. In this example, I chose to use a circular region of radius $0.3'$ (0.005°).

```
punlearn makespec
pset makespec EvtFile=./pnt_source_comb.fits
pset makespec Spectrum=./spectra.pha
pset makespec RSPPath=${xmldir}
pset makespec clobber=yes
pset makespec EventFilter="{{RA - ${RA}}**2 + {DEC - ${DEC}}**2 > 0 \
&& {RA - ${RA}}**2 + {DEC - ${DEC}}**2 < 0.005**2"
makespec
```

With this simple case scenario of a power law emission $PSD(E) \sim E^\alpha$ we have an excellent fit in XSPEC with low error

$$\begin{aligned} n_0 &= 1.05815 \pm 5.90532 \cdot 10^{-3} \\ \alpha &= 2.18530 \cdot 10^{-4} \pm 1.01010 \cdot 10^{-6} \\ \chi^2 &= 1039.06/969 \sim 1.073 \end{aligned}$$

Also the spectrum plot with the best fit and the χ^2 graph both show there are no big biases in any energy interval between 0.3 and 10 keV, in which WFI effective area should be at its maximum values.

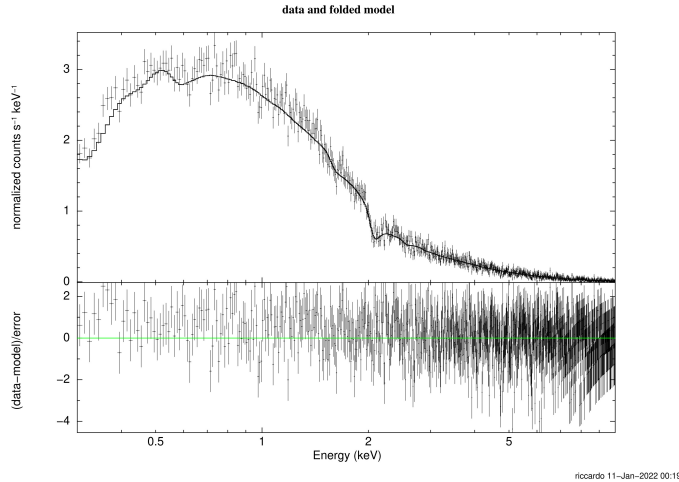


Figure 17: Spectrum of the point-like source and its emission model with points and solid black line, respectively

It is worth noting that the spectrum shape does not look like a power-law emission because this is obtained by convolving the ideal power-law emission with the instrument response through its ARF and RMF.

3.2 *Chandra* results comparison and simulations

In this subsection are describe the passages of the pipeline with which is possible to produce a simulated image and spectra for an extended object (i.e. a galaxy cluster) using SIXTE.

In particular, I will explain how to produce a simulation starting from a count image from another instrument such as the *Chandra* or XMM-Newton, or starting from a map produced with any kind of simulation.

This will be an extension of the simpler point-like example, in which I will show how I reached a realistic simulation of physical objects, with which I obtained the results extensively described in the fifth section of this thesis.

In particular, I produced WFI simulated images starting from *Chandra* observations to compare the originals with my results and be sure to be capable to produce realistic images with this pipeline; and I used the pipeline with simulated objects as an input to analyze the physics of different objects of known mass and customary parameters.

3.2.1 Cluster Simput Files Creation

In the case of extended sources, the SIMPUT creation function I used in the pipeline is *simputmultispec*, which requires as an input a counts map of the source and a parameter value map related to the spectral model in the XCM file.

The choice of *simputmultispec* over other methods is related to its versatility and the many parameters which it makes possible to manipulate. SIXTE manual underlines how this is a function most suitable for 2d input maps as parameter files cannot be deprojected. In the case of 3D input data, the manual shows how to produce a simulation using functions such as *simputmulticell*.

Below is an example of the function in the case of a cluster with a single parameter maps:

```
#Cluster Simput
pset simputmultispec Simput=./cluster.simput
pset simputmultispec XSPECFile=./cluster_model.xcm
pset simputmultispec ImageFile="./sim_map.fits"
pset simputmultispec ParamFiles="./simkt_map.fits"
pset simputmultispec ParamNames="2"
pset simputmultispec ParamsLogScale="yes"
pset simputmultispec ParamsNumValues="32"
pset simputmultispec Emin = 0.5
pset simputmultispec Emax = 10.0
pset simputmultispec srcFlux = 1.049E-11
pset simputmultispec RA=${RA}
pset simputmultispec Dec=${DEC}
pset simputmultispec Elow=0.1
pset simputmultispec Eup=12
pset simputmultispec Estep=0.00025
pset simputmultispec clobber=yes
simputmultispec
```

I will now describe the aspects taken into account in the creation of the SIMPUT file for a real object simulation:

Input count maps While almost all function parameters for simputmultispec are similar to those used with the function simpufile in the case of the point-like source, a few words can be spent on the input counts map for an extended object. In particular, we can consider two settings depending on the source of our maps.

In the case of maps from simulations, we can produce a cluster-only normalised counts map with no background photons. This makes us sure each photon emission will be treated properly with its spectral emission.

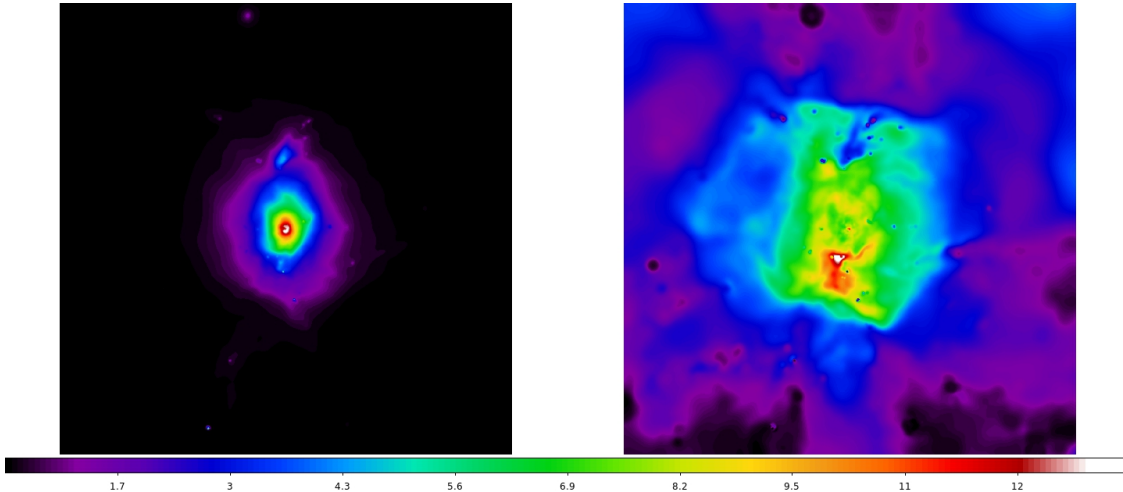


Figure 18: Count map from a simulated source in logarithmic scale and its temperature map in linear scale in the left and right panel, respectively. With simulations such as that is possible to reach a really high resolution in the maps, giving them this fluid and continuous look, which we would not expect from a real observation and in a SIXTE simulation.

When working with maps from real data reduction, on the other hand, we will probably have as an input a background-subtracted exposure time-normalised counts map.

The difference from the simulated input is that even after subtracting the average background counts, the maps would show photons coming from regions where there was no source. Furthermore, the SIMPUT creation imposes a spectral model to all the photons: if we created the SIMPUT from the whole image, even though counts are normalised and background subtracted, SIXTE would interpret the whole image as a source radiating as described in the spectral model for the cluster.

Because of these two reasons, it was required to cut our input counts maps and parameter maps to include only the area of the source.

This cut requires some really strong hypothesis on where the source brightness as seen on the real data get submerged by background emission. This could be made less impactful on the results remembering that the simulation can only use data that were also available above the background in the original image: so the background limit from the original data analysis should be considered a good estimator to the radius for the cut, while everything much over that limit was not directly derived from the input.

In the end, I chose to cut the images within an elliptical region with a major axis corresponding to the source R_{500} , as estimated in the *Chandra* analysis pipeline. This choice was justified by the fact this radius is an intrinsic physical property of the source as we saw it and is by a good approximation our actual observational limit for clusters in the X-rays. Whether possible I always tried to use $R_{200} \sim R_{500}/0.7$, but it was often larger than the whole *Chandra* sensor.

This might seem like a strong limit to the potential outcomes of simulated images with SIXTE, but the analysis of simulations made with another instrument input map would probably be more useful as a comparing/reference tool of the results, rather than an investigating instrument. On the other hand, a WFI simulation produced starting from simulated objects could be used properly for physical and instrumental limits analysis.

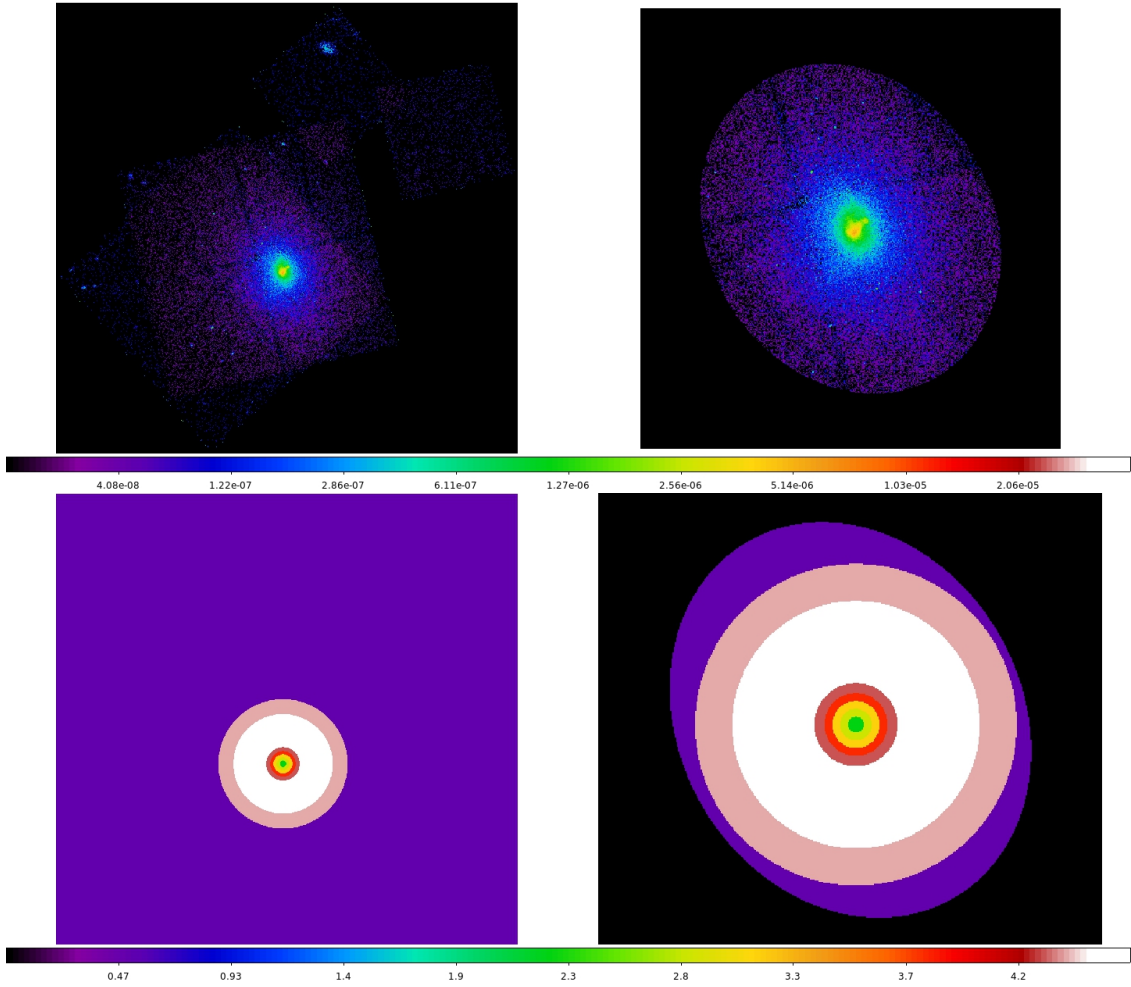


Figure 19: *Top panels:* Abell 1413 full and cut surface brightness map in the left and right panel, respectively. *Bottom panels:* Same as top panels except for the fact that we show the temperature map.

Spectral Models The parameter map is related to the model in the simputmultispec function through the paraNames parameter, while the keywords paramsNumValues and paramsLogScale refer to the number of intervals in which the parameter values are divided between their minimum and maximum and whether these intervals are to be considered on a logarithmic scale or not.

In the case of galaxy clusters, we used an APEC model for their spectrum. This is a numerical model suited for describing collisionally-ionised diffuse gas emission such as the ICM. It has dependencies on the source temperature (in keV), metal abundances (relative to solar abundances), and redshift. We used only the temperature map to describe the parameter distribution of the source. The abundance map had a less impactful effect on the simulation and had less variance on the whole cluster areas, for these reasons we did not use it.

We multiplied the APEC model by a factor n_H , which represent the hydrogen column density between us and the source (in cm^{-2}). This number mostly takes into account the near universe hydrogen absorption so it is by a good approximation only dependent on the source direction, but not on its distance from us.

$$PSD(E) = n_H \cdot APEC(T, z, Z) \quad (17)$$

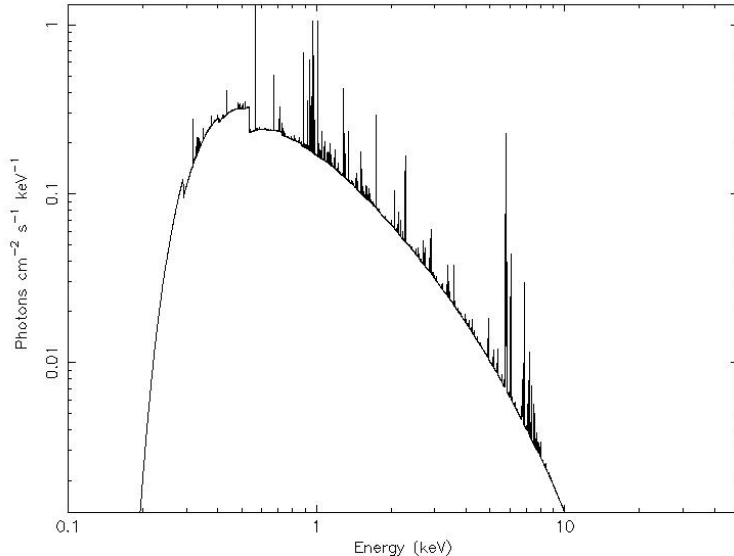


Figure 20: Spectrum of the $n_H \cdot APEC$ model, with $n_H = 8 \cdot 10^{20}, cm^{-2}$, $kT = 5 \text{ keV}$, $Z = 0.4 Z_\odot$ and $z = 0.15$

Fluxes For what concerns the fluxes of sources, while for SIMPUT created starting from simulated objects counts maps it is customary to choose a value for it, In the case of SIMPUT created starting from other instruments counts maps of a real object is important to use the correct flux for the source in the input energy range of choice, as it is an intrinsic property of them.

The count rate can be used as an input in any PIMMS (Portable, Interactive Multi-Mission Simulator) online (with other information such as nh, z, and spectral model) to derive a flux. We referred to NASA/heasrc PIMMS website for our calculations.

Convert From:	Into:					
CHANDRA/ACIS-I Count Rate	FLUX					
Examples of Common FLUX Input/Output Ranges						
Input Energy Range (low-high): 0.7-2.5	<input checked="" type="radio"/> keV <input type="radio"/> Angstroms	Units				
Output Energy Range (low-high): 0.7-2.5	<input checked="" type="radio"/> keV <input type="radio"/> Angstroms	Units				
Source Flux / Count Rate: 0.04	(erg/cm ² /s) (counts/s)					
Galactic nH	Redshift	Intrinsic nH				
1.5e20	(cm ⁻²)	0.1427	none	(cm ⁻²)		
Model of Source:						
<input type="radio"/> Power Law	Photon Index: <input type="text"/>					
<input type="radio"/> Black Body	keV: <input type="text"/>					
<input type="radio"/> Therm. Bremss.	KT: <input type="text"/>					
<input checked="" type="radio"/> APEC	0.4 Solar Abundance	<input type="checkbox"/>	8.00	<input type="checkbox"/>	8.6173	<input type="checkbox"/>
<input type="button" value="Estimate Count Rate"/> <input type="button" value="Reset"/>						

Figure 21: An example of input for the flux estimate of a source as seen by *Chandra* with a Count Rate of 0.0 *cts/sec*

In particular, when using *Chandra* images as input for the `simputmultispec` functions, I derived the source count rate from the original *Chandra* event files using the image display software SAOImageDS9 in the [0.7-2.5] keV energy range, which has the highest effective area for Chandra. This was possible simply by selecting my source region, summing every count within, dividing by the exposure time of the image after subtracting the counts from an equal area region from source emission i.e. the background:

$$ctr = \frac{ct_{src} - ct_{bkg}}{t_{exp}}$$

A more rigorous way to calculate the image count rate could be achieved using a spectral analysis tool such as XSPEC, with its show rate function. This particular process was impossible with the Chandra data reduction and analysis pipeline we used to produce our input maps because the spectra files it produced did not have information on the exposure time, thus not letting XSPEC calculate the rate correctly.

The flux of a source in a band can be estimated also referring to online catalogues, often containing estimates for known sources fluxes in a few energy bands. The cons of this method are it does not refer to the image directly used as an input but only to external data, making the possibility of an inconsistency issue higher. This method does not make it possible to control the energy band when there is not enough data on a particular source from any catalogue.

All these methods gave similar and coherent results for the flux value. If there are any inconsistencies in flux values for the same object in the same band with the same conditions, it may indicate to be an issue with the data used.

3.2.2 Background Simputs

A notable difference with the case of the simple example of section one is that for a complete simulation we also need to produce a SIMPUT file for the background.

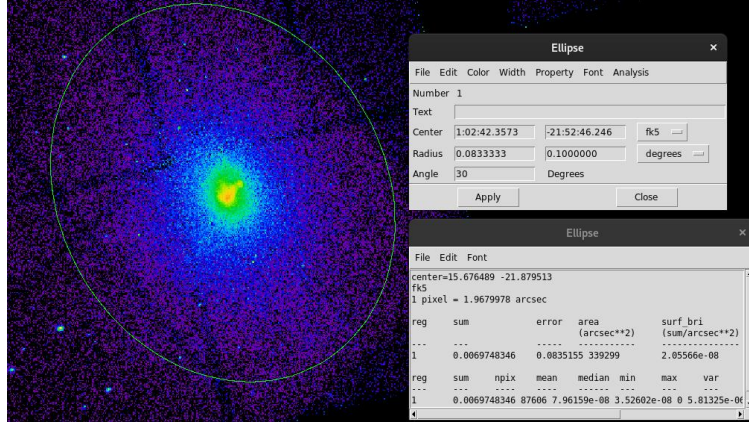


Figure 22: Built in DS9 tools which measure the total counts in the region containing the source and we used for the map cut. The exposure time was known and for this particular image of Abell 1413, made from a merge of two Chandra observations, it was $\sim 115\text{ ksec}$

For my simulations, I chose to create a SIMPUT file for the sky component of the background and one for the particle/instrumental component of the background. These two have the same spectral model and their input counts maps can be created customary or starting from an empty space image of the region of interest.

Below an example of the simputmultispec implementation in the case of a sky background SIMPUT. The particle background SIMPUT would have the same script, with different input count map and parameter maps:

```
#Sky Bkg Simput
pset simputmultispec Simput=./bkg_sky.simput
pset simputmultispec XSPECFile=./bkg_model.xcm
pset simputmultispec ImageFile="./fake_sky_bkg.fits"
pset simputmultispec ParamFiles="./sky_norm1.fits; \
./sky_norm2.fits;./sky_norm3.fits"
pset simputmultispec ParamNames="5;10;12"
pset simputmultispec ParamsLogScale="no;no;no"
pset simputmultispec ParamsNumValues="32;32;32"
pset simputmultispec Emin = 0.5
pset simputmultispec Emax = 10.0
pset simputmultispec srcFlux = 5.252E-14
pset simputmultispec RA=${RA}
pset simputmultispec Dec=${DEC}
pset simputmultispec Elow=0.1
pset simputmultispec Eup=12
pset simputmultispec Estep=0.00025
pset simputmultispec clobber=yes
simputmultispec
```

Background spectral model In particular, the spectral model we used is a combination of three different terms:

$$PSD(E) = n_H \cdot (n_0 \cdot APEC + n_1 \cdot APEC + n_2 \cdot E^{1.42}) \quad (18)$$

As seen when describing the cluster spectral model, the APEC term describes a hot plasma emission. In this case, the two APEC component of the spectral models refers to two different sources contributing to the background of any X-ray observation from a telescope around the Earth: one is an emission at redshift $z = 0$ which we believe comes from the exploded blob of gas in which the Sun was formed, while the other refers to the thermal emission from the Milky Way and from the gas that surrounds it. The former is a low-temperature emission, but because of us being surrounded by it, it cannot be neglected anyway.

The power-law emission term in the model describes the collective emission from each extra-galactic X-ray source that our telescope cannot resolve. Literature shows this whole emission can be properly fit with a power-law emission with norm $n_0 \sim 2 \cdot 10^{-9}$ and exponent $\alpha + 1.42$.

The fact that one of the APECs and the power-law component of the emission are due to extragalactic sources would require us to use a different hydrogen column-density parameter n_H for them, but as the objective of our test did not require precise spectral modelling of the background we used the same value for them and the $z = 0$ component. A simulation concerning the details of sky emission would probably benefit in using a more complex model for the background emission.

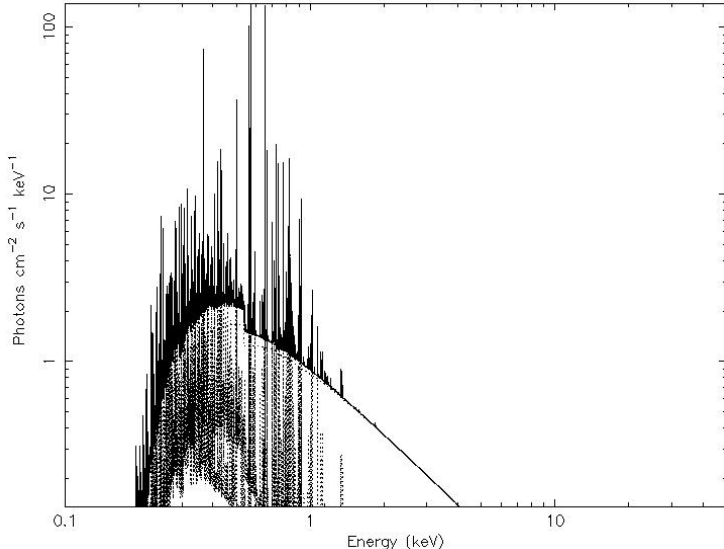


Figure 23: Example of the spectrum from our model, with $n_H = 6.89 \cdot 10^{20} \text{ cm}^{-2}$, $kT_1 = 0.14 \text{ keV}$, $kT_2 = 0.25 \text{ keV}$, $Z_1 = Z_2 = 0.4 Z_\odot$ and $z = 0$

Input maps and fluxes For simplicity, I generated input maps for the two background components using python and I had them have random positive values distributed as a normalised Gaussian branch. Their parameter maps refer to the three normalisations of each of their spectral model components and are also produced in python as a copy of the brightness map multiplied for a constant numerical factor.

The simputmultispec functions for the two backgrounds are created almost in the same way, with the only difference being that the two input counts maps have different normalisations, with a ratio $cts_{bkg}/cts_{par} = 10^{-5}$. This is because while for the sky background we can measure a realistic count rate and then build a realistic count map, to measure the particle/instrumental background we should use a 0-counts map (only

instrumental noise, no sources). Unfortunately, SIXTE at the moment does not permit the creation of a SIMPUT starting from a uniform input map or a map with too small values. For these reasons, we created the particle background input count map similarly to the sky background one, with a realistic ratio.

As for the choice of the spectral model, this method can be considered simplistic but it is also realistic enough for this thesis' objective of creating a working pipeline for simulating images of galaxy clusters as seen from Athena using SIXTE. An analysis that might want to investigate the details of the background could use this pipeline with a more precise spectral model and input map.

For the fluxes, we used for the background the same method as for the cluster: selecting an area as big as the cluster in the input image we measured the count rate in a part of the sky far from the cluster and input it to a PIMMS online service.

As we used maps with different normalisations, we were able to use the same fluxes for the sky background and the particle background component when producing their respective SIMPUT files.

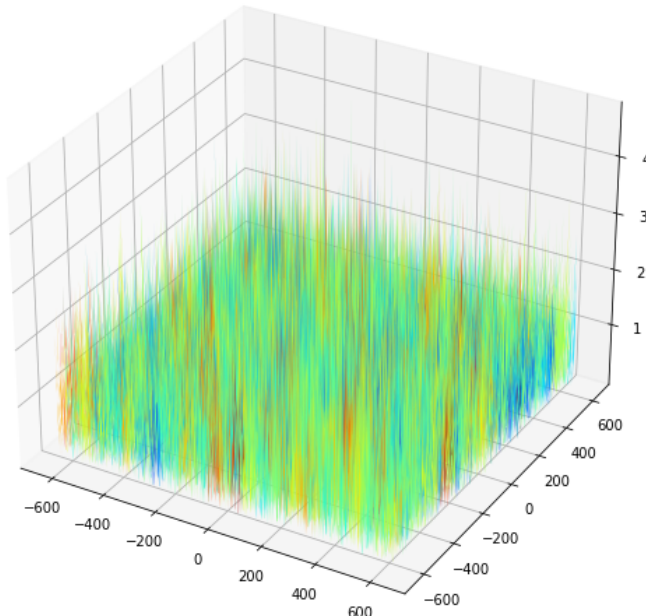


Figure 24: Example of the counts and normalisation map used as an input for the `simputmultispec` SIXTE function with which I created the two background simputs for my simulations. In this case the values are all positives and distributed as a normalised Gaussian with average $\mu = 0$ and standard deviation $\sigma = 1$.

Use of the background SIMPUT files The sky background SIMPUT can be used as a secondary SIMPUT for the complete image simulation, in addition to the cluster SIMPUT and any other eventual SIMPUT.

The particle background SIMPUT is a bit more complicated subject: SIXTE uses an instrument calibration file to model the instrumental background and add it automatically to every simulation, so it is not needed to create a particle background SIMPUT to add to the source complete simulation. Instead, this kind of SIMPUT could be used for example to create a "flat image" to be subtracted from the "complete cluster image" made from the cluster and sky background SIMPUT.

During my subsequent analysis of the simulation results in python, the library pyproffit required explicitly a particle background only image for its brightness modelling.

The spectra derived from the simulations made with only the particle background SIMPUT spectra is also needed to be subtracted to every cluster and sky background spectra to obtain better spectral fits.

At the time of writing this thesis, the official Athena instrument files for the particle background spectra is a constant function for every energy bin. While this is not technically very accurate, it did not seem to create any major issue with the results and anyhow it might be too early in Athena development to create a more precise instrument background model as the telescope is still being developed and we cannot predict every detail in the instrument which could affect the particle background for observations.

3.2.3 Simulation and Imaging

The WFI simulation and imaging scripts for a complete extended source are mostly the same as in the case of the simple point-like source example, but I want to overview the few major differences that make the whole simulation a bit more refined and realistic.

Complete image for data analysis The complete simulation can be constructed using a combination of the cluster SIMPUT with, the sky background SIMPUT (the particle background is added by SIXTE in the script) and an eventual point-like sources SIMPUT. The latter can be built from scratch with a SIXTE script as a catalogue of sources or, as I finally did, someone can simply use a real catalogue as the *Chandra* Deep Field-South Survey as a source of realistic data and create a SIMPUT catalogue using any number of real sources' data.

```
#Complete Image
punlearn athenawfisim
pset athenawfisim XMLFile0=${xml0}
pset athenawfisim XMLFile1=${xml1}
pset athenawfisim XMLFile2=${xml2}
pset athenawfisim XMLFile3=${xml3}
pset athenawfisim RA=${RA}
pset athenawfisim Dec=${DEC}
pset athenawfisim Prefix=../image-
pset athenawfisim Exposure=20000
pset athenawfisim clobber=yes
pset athenawfisim Attitude=../attitude_80ksec.att
pset athenawfisim Simput=../cluster.simput
pset athenawfisim Simput2=../bkg_sky.simput
pset athenawfisim Simput3=../srcs_cat.simput
athenawfisim

ftmerge \
./image_chip0_evt.fits ./image_chip2_evt.fits ./image_chip1_evt.fits ,\
./image_chip3_evt.fits \
./image_combined_evt.fits clobber=yes
```

Particle background image for data analysis For some kind of subsequent analysis, we may be required to produce an image of the only particle (or sky) background. Indeed in my result analysis routine using the python libraries pyproffit and hydromass I had to give as an input a particle background image with the same exposure time of the complete image.

```
#Particle background image for pyproffit
punlearn athenawfisim
pset athenawfisim XMLFile0=${xml0}
pset athenawfisim XMLFile1=${xml1}
pset athenawfisim XMLFile2=${xml2}
pset athenawfisim XMLFile3=${xml3}
pset athenawfisim RA=${RA}
pset athenawfisim Dec=${DEC}
pset athenawfisim Prefix=./evt/bkg_
pset athenawfisim Exposure=20000
pset athenawfisim clobber=yes
pset athenawfisim Attitude=./input/attitude_80ksec.att
pset athenawfisim Simput=./simput/bkg-part.simput
athenawfisim

ftmerge \
./evt/bkg_chip0_evt.fits ./evt/bkg_chip2_evt.fits ./evt/bkg_chip1_evt.fits ,\
./evt/bkg_chip3_evt.fits \
./evt/bkg_combined_evt.fits clobber=yes
```

Particle background image for spectra Below I'm showing the script needed for producing a simulation of the only particle background with a longer exposure time than the complete image, that will be needed for the spectral analysis. Its longer exposure time is justified by the fact that a real spectral observation would be longer than an imaging one and also by the fact that my analysis of temperature profiles is based on the hypothesis that the spectral model for the background was known and constant, as also WFI instrument files I used involved. The longer exposure for the instrumental/particle background only images provided better statistics on each bin, which guaranteed us a result closer to the expected temperature value and made the spectral fit precise enough for the subsequent deprojection of the temperature profile, during the result analysis.

During my test, I found out a longer exposure simulation is really helpful for fitting background spectra from WFI but does not make a big difference in the cluster spectra fitting, so I personally chose to avoid doing it to save time in my simulations. Another user of the pipeline with peculiar aims may find the improvement in cluster spectra fit big enough to need considering it and choose to make also a complete longer exposure simulation. The difference in exposure time between the complete/cluster image and the particle background image does not create introduce any issue in the spectral fits as it only changes the counts' numerosity but not the shape of their spectral distribution function.

```
#Particle Background image for Spectra
punlearn athenawfisim
pset athenawfisim XMLFile0=${xml0}
pset athenawfisim XMLFile1=${xml1}
pset athenawfisim XMLFile2=${xml2}
pset athenawfisim XMLFile3=${xml3}
pset athenawfisim RA=${RA}
```

```

pset athenawfisim Dec=${DEC}
pset athenawfisim Prefix=./bkg_spectra_
pset athenawfisim Exposure=40000
pset athenawfisim clobber=yes
pset athenawfisim Attitude=./attitude_80ksec.att
pset athenawfisim Simput=./bkg_part.simput
athenawfisim

ftmerge \
./bkg_spectra_chip0_evt.fits ./bkg_spectra_chip2_evt.fits ./bkg_spectra_chip1_evt.\
./bkg_spectra_chip3_evt.fits \
./bkg_spectra_combined_evt.fits clobber=yes

```

Exposure Map A factor we did not include in the point-like simple example and which is related to the dithering of the satellite is the exposure map, which describes how long each point of an image was exposed during the observation.

SIXTE gives us simple functions to produce it which only requires information on the instrument files for the satellite and directly output an image, without producing an event file in between.

The image parameters and exposure time are the same as those of the complete and background image and are not related to the simulation physics.

```

exposure_map \
Vignetting=${xmlfile}/athena_vig_15row_20171016.fits \
Attitude=./attitude_80ksec.att \
Exposuremap=./expo_map.fits \
XMLFile="${xml0};${xml1};${xml2};${xml3}" \
fov_diameter=70 \
CoordinateSystem=0 projection_type=TAN \
NAXIS1=1078 NAXIS2=1078 \
CUNIT1=deg CUNIT2=deg \
CRVAL1=${RA} CRVAL2=${DEC} \
CRPIX1=593.192308 CRPIX2=485.807692 \
CDELT1=6.207043e-04 CDELT2=6.207043e-04 \
TSTART=0 timespan=20000.0 dt=100. \
chatter=3 clobber=true

```

Region File During the analysis of the simulation results, I needed a method to remove every point-like source from my complete image, as I would do with real data. For doing this I used the CIAO built-in function, *wavdetect*, which can isolate sources from an image using wavelet analysis.

Below an example of implementation of the function:

```

#Region file creation using CIAO script
punlearn wavdetect
pset wavdetect infile=./image.fits
pset wavdetect outfile=./out_ima.fits
pset wavdetect scellfile=./cell_ima.fits
pset wavdetect imagefile=./ima_ima.fits
pset wavdetect defnbkgfile=./bkg_ima.fits

```

```

pset wavdetect regfile=./reg.reg
pset wavdetect clobber=yes
wavdetect

```

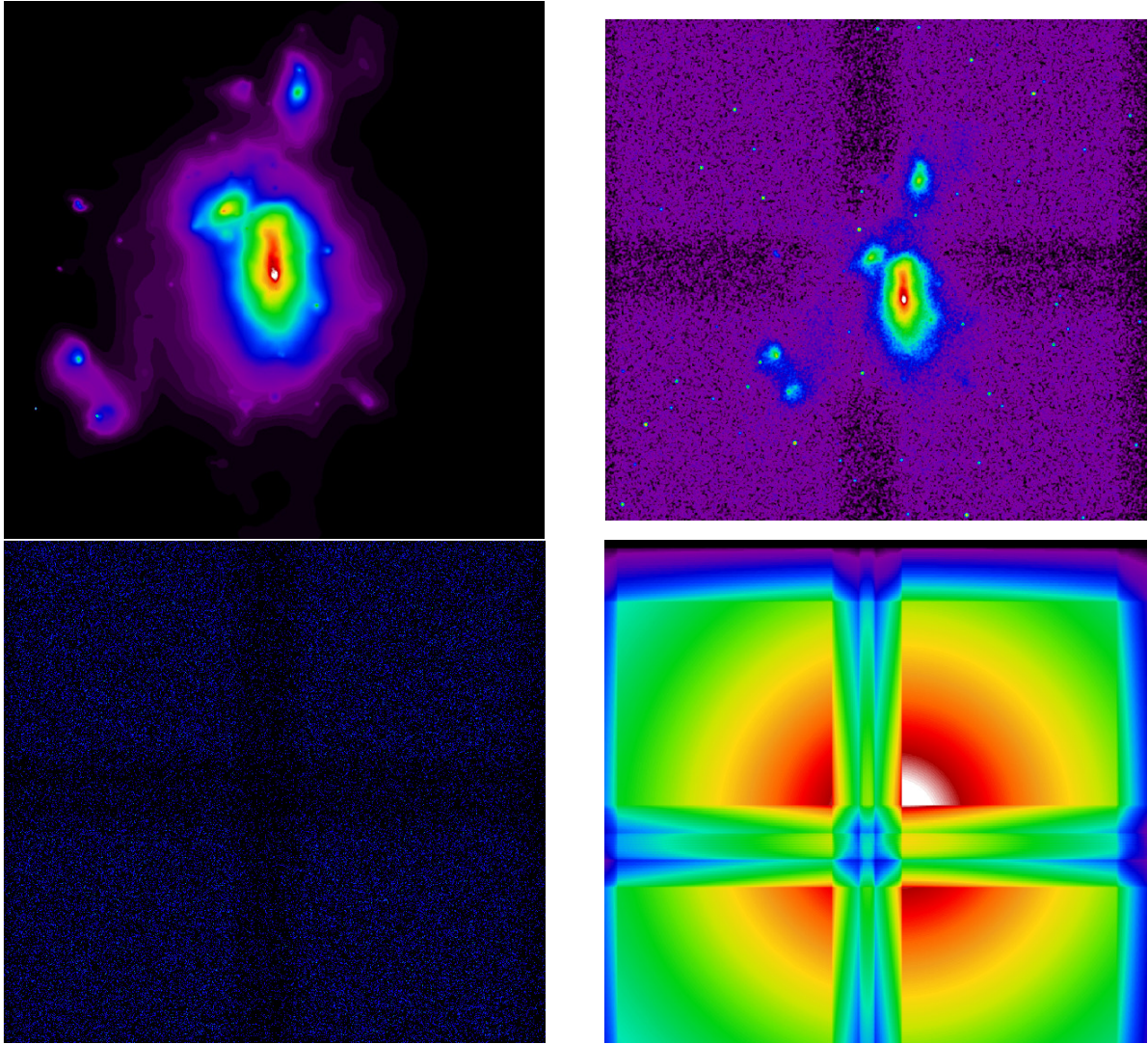


Figure 25: *Top panels:* Input simulation map and outcome of our pipeline in the left and right panel, respectively. The latter has visibly less details and point-like sources and background are visible, with the gap between WFI sensors partially covered thanks to the dithering. *Bottom panels:* an image with only the particle background used for image analysis and the exposure map in linear scale in the left and right panel, respectively. The latter clearly shows how because of dithering the telescope spent the most time on the observation pointing center, in the top-left side, in white.

As the function is not completely reliable in its capability of separating different sources, I checked by eye its results and eventually manually corrected the list of sources that will be removed from the analysis. This also helps in keeping the statistics high in the largest possible fraction of the image.

Furthermore, given the possibility for WFI to see larger substructures surrounding the central parts of galaxy clusters this kind of treatment of the image will be fundamental in recognizing these structures and also comparing the physical analysis of clusters with or without keeping them in the image.

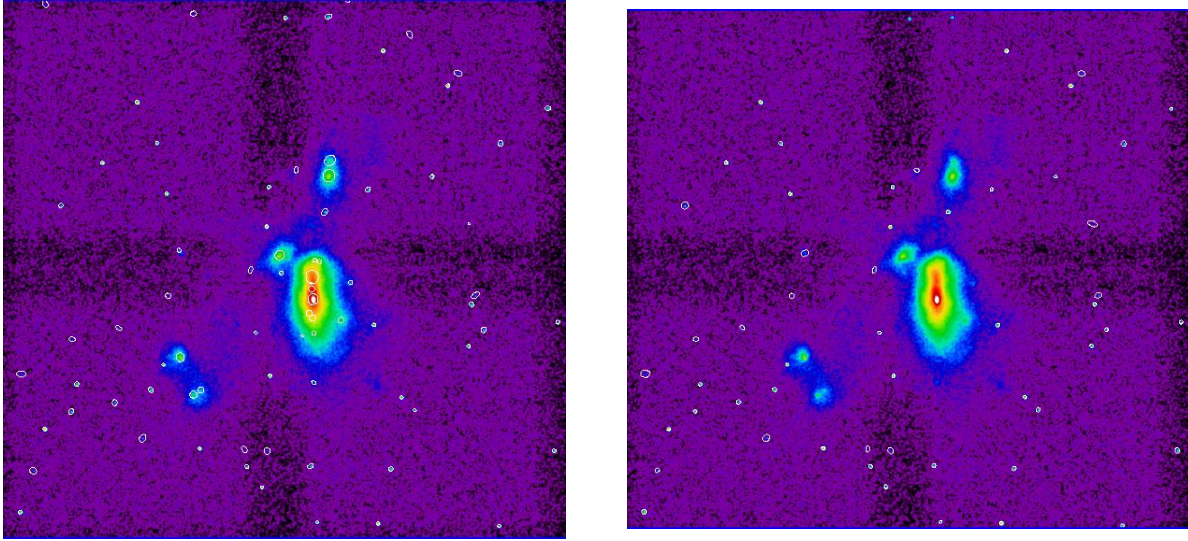


Figure 26: Same simulated object image produced using SIXTE with the regions find using with wavdetect originally and with the regions I manually chose to keep after removing every double pick and deciding not to mask any substructure of the cluster, in the left and right panel, respectively.

3.2.4 Spectra and Temperature Fit

The most articulated section of the pipeline is about the extraction of spectra from the event files of the various simulations. This is because with the addition of the backgrounds to the simulation and using more complex spectral models the fits became harder to achieve.

First, I'm going to explain the SIXTE functions with which we can produce PHA files containing spectral data, and then I'm going to describe the functioning of the xspec script we wrote, with which is possible to fit these spectra to derive a value for the observed temperature of the source.

Spectra The main instrument for the spectroscopy of our event files revolves around the SIXTE function *makespec*, which requires as an input an event file, the path to the directory with the instrument files, and a region within which to extract the photons.

In particular, I extracted spectra from the area occupied by the source to fit the source spectra, and from an outer area far from the source to fit the background. Both from the complete image, which represented the cluster and the sky background, and from the particle background only images with longer exposure time, with which I measured the background spectra to subtract to every other spectrum.

After a few tests, I found out that for a galaxy cluster are consistently useful and functional a few precautions:

- First of all I measured the source spectra using as regions a series of 5-7 annuli centred on the exact position of the source. These coordinates can be observed from the complete image or derived with a script looking for example for the pixel with the peak in counts on an exposure normalised image. While the latter is the most simple and precise method, which I achieved with a python script, the latter can be often useful while analyzing perturbed and asymmetrical objects such as the bullet cluster. As sources are typically brighter in their centre, it is useful to have the annuli thickness increase progressively starting from a lower value near the brightness peak.
- The maximum radius from which is possible to extract spectra of the source with large enough statistics and possibly a good fit is usually derivable by observing on the brightness profile of the source (which I produced in python using pyproffit) at which radius from its centre the source brightness become submerged under their particle background (with the same exposure time as the complete image). An example is shown in **figure 27**. I guess another possible solution could have been to find from the image the radius above which it is impossible to fit the spectra using the cluster spectral model with trial and error, but this would have been time-consuming and less optimal.
- The radii of the annulus from which derive the background spectra far from the source is derivable by observing the brightness profile of the source too. In particular, it is around the radius from the source's centre at which the brightness stops decreasing and becomes constant, i.e. where the sky+particle background is the dominant source. This could be derived without using the brightness profile looking at the exposure time normalised image from the radius around which the counts are constant.
- I found it useful to use the *ftgrouppha* HEADAS function to rebin the spectra to obtain an equally distributed number of counts for the energy bin. In particular the "opt" (optimal) grouptype is based on Kaastra & Bleeker 2016 optimal binning. This essentially grants a better fit at all energies bypassing the fact that we could have a lower count in some bins making a good spectral fit harder to achieve for XSPEC.

Below is an example of a script with which I would extract spectra from two annuli centred on the source from the complete image event files (the scripts for the particle image and the far annulus are completely analogous):

```
#Spectrum extraction radii for annuli
export R0=0.
export R1=$(awk "BEGIN {print .25/60}")
export R2=$(awk "BEGIN {print .75/60}")

#Cluster spectra
punlearn makespec
pset makespec EvtFile=./image_combined_evt.fits
pset makespec Spectrum=./spectra_0.pha
pset makespec RSPPPath=${xmldir}
pset makespec clobber=yes
pset makespec EventFilter={"RA - ${RAS} }**2 + {DEC - ${DECS} }**2 > ${R0}**2 \
&& {RA - ${RAS} }**2 + {DEC - ${DECS} }**2 < ${R1}**2"
makespec
```

```

ftgrouppha infile=./spectra_0.pha outfile=./spectra_0_rebin.pha \
    grouptype=opt respfile=./athena_wfi_SIXTE_v20150504.rmf

pset makespec Spectrum=./spectra_1.pha
pset makespec EventFilter="{{RA - ${RAS}}**2 + {DEC - ${DECS}}**2 > ${R1}**2 \ 
    && {RA - ${RAS}}**2 + {DEC - ${DECS}}**2 < ${R2}**2"
makespec

ftgrouppha infile=./spectra_1.pha outfile=./spectra_1_rebin.pha \
    grouptype=opt respfile=./athena_wfi_SIXTE_v20150504.rmf

```

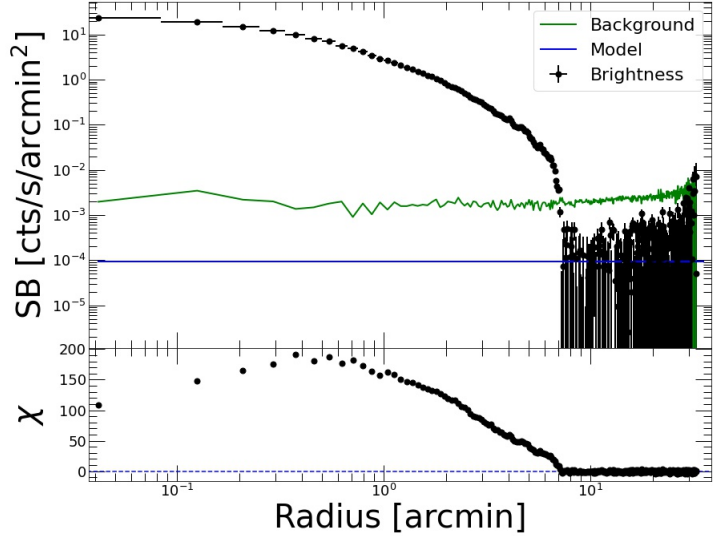


Figure 27: Surface brightness profile where we can see the radius at which the source brightness go below the particle background brightness (in green) at around 5' and the background fit (in blue) which here is taken between 15' and 20'. The χ^2 is shown in the bottom.

ARF correction The only last preparation required before the fit is to use SIXTE_arfgen on each annulus from which the source and background spectra were extracted. This SIXTE function provides a corrected ARF for the decentered source regions calculated starting from the point of view averaged ARF file in the instrument directory for the telescope. Usually, the correction for vignetting is small in between the area of 2-5' occupied by the source, but we found it out to be relevant for the spectral fit success, at larger radii from the cluster above all.

While they are both taken into account in the fit, the reason to correct just the ARF and not the RMF before the spectral fit is that the former is correlated to our estimate to the spectrum continuum component and can change the temperature we measure from its cut-off, especially far from the centre where vignetting gets more intense. RMF, on the other hand, is related to the sensor spectral resolution and so its capability in discerning emission lines, which we do not consider in our fit but are important for other kinds of spectral analysis.

Spectral Fit (XSPEC) To fit the spectra in the PHA file and derive a value for the observed temperature of our source, I developed a script using the X-ray spectral analysis tool XSPEC.

The script makes a fit of the spectra on a spectral model made simply summing the background and cluster model used for the SIMPUT creations, the former multiplied for a scaling factor:

$$PSD(E) = n_H \cdot [A \cdot (n_0 \cdot APEC + n_1 \cdot APEC + n_2 \cdot e^{1.42}n) + n_3 \cdot APEC(T, z, Z)] \quad (19)$$

I briefly summarise how the script works:

1. We start with the cluster component of the spectral model frozen, with 0-value norm and the particle background spectra for this annulus is subtracted to the sky component.
2. We fit the background spectra from the outer annulus using as free parameters its three norms and two temperatures. This will give us a background temperature and fit for the outer region of the image.
3. We freeze the background components and thaw the cluster component of the spectral model.

Then for each source annulus:

3. We multiply the background component scaling factor for the area ratio between the outer background annulus and the current source annulus. This is to take into account the lower number of counts from the background we expect in a smaller area and which should scale linearly with region area.
4. We subtract the particle background spectra and we fit it with the cluster model, deriving the source temperature and abundance while the background component is fixed. The cluster free parameters are the temperature, metals abundance, and norm.

During the development of this pipeline, we found out that the energy range choice was crucial for the quality of WFI spectra fit of clusters. We always had to be sure to include in this range the temperature around which we expected the exponential cut-off to be, but we also found out that, considering a range too large, the fit was too hard for the software to achieve and resulted in giving physically absurd results, if not checked.

5. We save the fit parameters we need and their errors into a file for use in any subsequent analysis.

In particular, for my analysis of the galaxy clusters mass profiles, I saved as an output the cluster temperature and metals abundance from each annulus' fit. While the first quantity is directly needed for the mass derivation, the second was kept as a free parameter for the fit to work more smoothly and with fewer limitations. Making sure the value of Z was almost constant and around the expected value of 0.3 – 0.4 gave us another precious probe for the quality of our spectral fits when analyzing the clusters' temperature profiles.

With the simulation event files we produced and using the images and spectra we derived from that, we can now analyze our source directly. This will be explained in detail in the next section of this work.

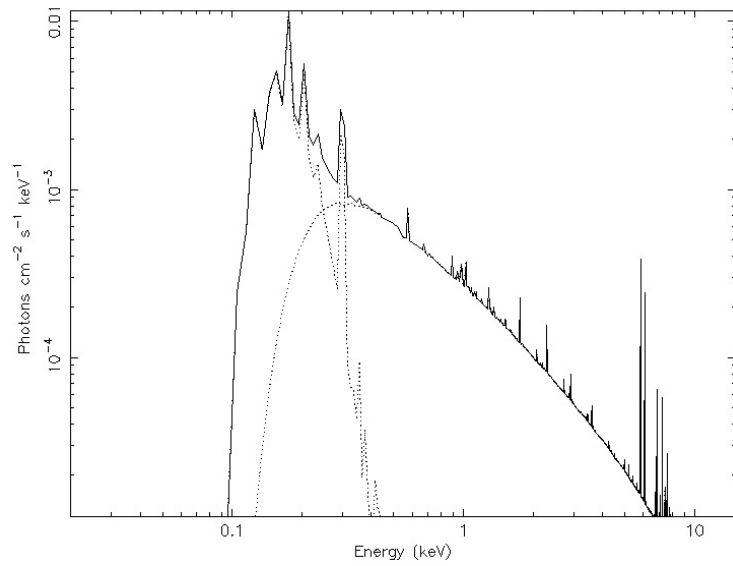


Figure 28: Example of the spectrum of our cluster model taken from an annulus from 5' to 6' from the source. It has $A = 0.114$, $n_H = 1.81 \cdot 10^{20} \text{ cm}^{-2}$, $Z = 0.4 \cdot Z_{\odot}$, $z_0 = z_1 = z_2 = 0$, $n_0 = 0.355$, $n_1 = 3.4 \cdot 10^{-6}$, $n_2 = 5.6 \cdot 10^{-6}$, $n_3 = 1.31 \cdot 10^{-3}$, and $z_3 = 0.1436$

4 Profiles and science using the pipeline outputs

In this section of the thesis, I explain how I used the **products of the simulation pipeline** to study the physics of galaxy clusters.

In particular, I built a code with which extracts observed brightness, density and temperature profiles of simulated observation from the images and spectra I produced using SIXTE. These profiles were later deprojected using a **non-parametrical forwarding method** that also gave as an output a **deprojected radial mass profile**: the final object of our scientific analysis for this project.

As for the pipeline, developing this analysis procedure was mostly based on a bottom-up understanding of the different technical instruments at our disposal and we proceeded to test our results with increasingly complex analysis.

I will describe here the whole analysis process and the choice we made, while often dwelling on the tests and calibrations we had to consider to make sure of the accuracy of our results. In particular, the **comparison with *Chandra* observations** was an important calibration process, with which we confirmed that our pipeline lead us to produce consistent and realistic observations and analysis of an object, starting from a simple count-map. With that, I've been able to evaluate a systematic bias in my SIXTE simulations results to consider in their analysis.

Instead of choosing to calibrate our pipeline comparing a CIAO analysis of *Chandra* image with the analysis of SIXTE simulated images using the *Chandra* image as input, someone may wonder if I might have chosen to compare our SIXTE simulations with a simulated object instead. The problem, in that case, is that we would have had as an input something different from a count map, which is the actual form of real data, and we would have worked with a cluster only map, instead of a complete image such as Chandra's.

In **section 5**, I will extensively talk about the results of the Chandra comparison and the analysis of SIXTE simulation of simulated objects.

Python, pyroffit and hydromass We decided to build our analysis around the use of **python**, structuring our scripts in **jupyter-notebooks** because of its increasing use in astrophysics, its open-source nature and its shrinking limitations due to performance thanks to the increasing power of computers.

The two Python libraries we worked with for deriving the galaxy cluster mass have both been created by Dr. Dominique Eckert and are named **pyroffit** and **hydromass**, respectively. The former was mostly used for calculating the source brightness and density profile, while the latter was involved in the deprojection of the temperature profiles and in calculating the mass radial profile of our objects. While pyroffit is already available online and fully documented³³, hydromass is still undocumented and in the last part of its development, but it was graciously provided for this work by its creator with a few example notebooks. This meant for us that instead of working with a manual for all the functions in hydromass we had to retro-engineer some of them paying much attention to unit measures and the structure of each input and output.

Hydromass and pyroffit have many functions in common and we could consider the former as an extension of its older sister, in some way. This meant for us that their functioning was often interlaced and some of their results could be interchanged and compared in the code.

³³see [39]

4.1 Brightness Profiles

The very first step of the analysis consists in producing the source brightness profile, with which derive the density profile, needed for the mass evaluation.

To do this, we begin loading in a python structure our three simulated images using the *pyproffit*.*Data* function, including informations about:

- the *complete image*, simulated using simplicities of the cluster, sky background and point-like sources. This will be the main subject of our whole analysis;
- the *particle background image*, of which counts will be subtracted from the complete image;
- the *exposure map*, centred on the source coordinates, which pyproffit uses to correct for the vignetting and normalise the complete image.

Unit measure The brightness profile is calculated by the *pyproffit*.*Profile* function in units of $cts/s/arcmin^2$ by summing the number of counts in a sequence of concentric rings centred on the source, divided by its exposure time. This process does not take into account the effective area of the detector, making its result instrument-dependant: if we compared a *Chandra* and Athena brightness profile of the same object with the same exposure time, we expected the former would measure a much lower brightness than the latter, in these units.

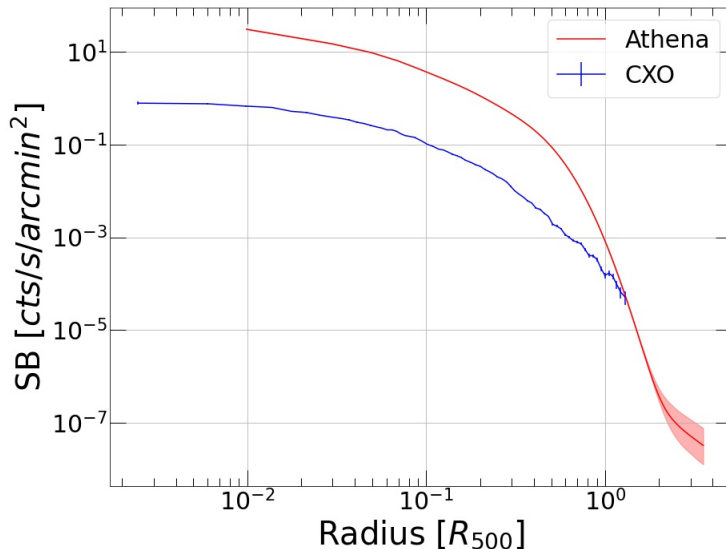


Figure 29: Comparison between the brightness profiles for the same object, Abell 1413, as measured from *Chandra* (CXO) with an exposure time of $\sim 90\ ksec$ and measured from WFI (Athena) in $\sim 20\ ksec$, in blue and red, respectively.

This consideration might sound prosy, but it mattered a lot during the development of this code when we could not figure out the cause for a large systematic bias we observed in our mass profiles comparison between *Chandra*'s and SIXTE's results at every radius. This happened in a later stage of the project and while we were looking for a plausible explanation of that results in any part of the pipeline, we noticed that even though we were comparing simulated WFI observations with a lower exposure time than the *Chandra*

images, with $t_{Ath} \sim 0.2 t_{CXO}$, we observed very close brightness profiles at all radii, when we would have expected a ratio between two and three orders of magnitudes between them, despite the different exposures³⁴.

In the end, it turned out that in that version of the pipeline we were measuring wrongly the source flux: we were deriving the source count rate from the *Chandra* spectra using XSPEC function *show rate*, not noticing these files did not have information on the exposure time of the data. This is the reason we switched to measuring count rates directly from the event files filtering for the energy range.

Observation centre choice The source position can be derived with a pyroffit function using a criterion of choice or directly given as an input to the code. As it proved to be reliable, in most cases we decided to make the software find the source centre defined as the point with peak brightness around the pointing coordinates. Just for a couple of complex objects, such as the bullet cluster, we had to indicate the coordinate we thought could better represent the centre for our analysis.

There are many possible reasons because which choose one or another substructure as its centre in the case of a complex object, but in my case, it was almost always because when observing real objects we had to compare our simulated images analysis with *Chandra*'s and we had to match all their parameters.



Figure 30: X-ray image of the bullet cluster in the [0.5-2.5] keV band. This system is formed by two sub-clusters that have interacted in the past and are now separating. We found out that with this kind of double-peaked system, even though the right structure is rightfully the brightest, sometimes the pyroffit. Profile function chose the left-substructure brightness peak as the centre and we had to manually choose the coordinates to pick. Probably the error is due to the method with which the function searches for the brightness peak, which it might consider to be the middle of a bell-shaped curve and not at one of the many peaks of a multinomial curve.

4.1.1 Background and Point-like sources

The brightness profile of a cluster is used to derive its density profile through the properties of the bremsstrahlung emission from the ICM; and the density profile is one of the two ingredients to derive the cluster mass profile under the hypothesis of hydrostatic equilibrium, which is the physical quantity under investigation in this project.

³⁴To be precise, here I'm talking about the comparison between deprojected brightness profile, while this section still regards the production of observed profiles. Anyhow the unit measure and overall brightness profile values are not modified during the deprojection for most of the objects and also the observed values order of magnitudes can be considered indicative of the true values.

Because of the significance of the cluster galaxy cluster's brightness profile in the mass derivation, we are particularly interested in isolating it from that of the background components and from that any point-like source or substructures surrounding the source.

Background subtraction As already mentioned, we built a data structure containing between other, the particle background image, of which counts the *pyproffit.Profile* function automatically subtracted the complete image³⁵.

Typically this brightness profile is not constant, but it grows slightly at larger radii. This is because this component on the background is linked to observations of unfocused photons which did not pass through the telescope mirrors and did not suffer any effect linked to vignetting, but their counts are artificially boosted by the exposure map correction, especially further from the image centre.

The remaining component of the background of which brightness profile we want to remove from that of the image is the sky background. As its sources come from photons interacting with the telescope mirrors and are thus affected by vignetting, the exposure correction makes its brightness profile almost constant, we do not need to simulate a specific image for it and we can fit it with a constant value to subtract the overall brightness profile.

Figure 31 shows a typical spectrum extracted using pyproffit, before and after subtracting the sky background:

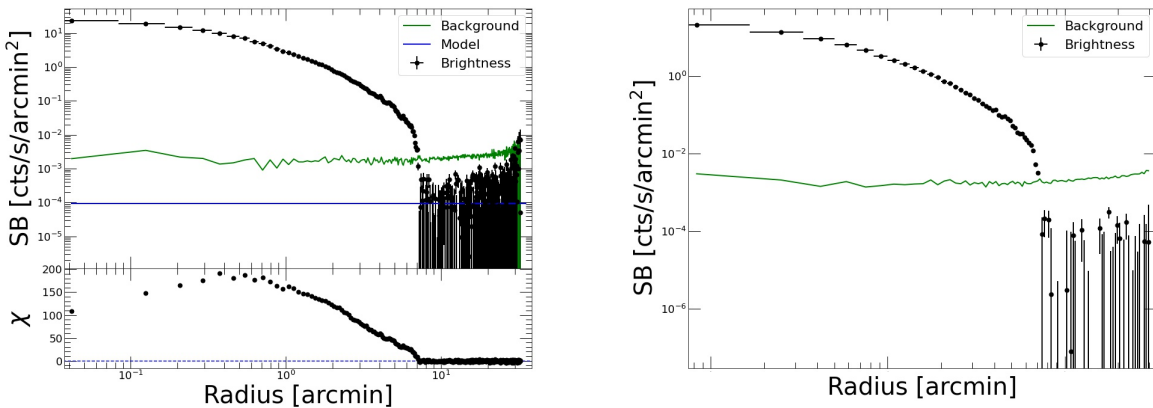


Figure 31: *Left panel:* Complete image brightness profile (in black), already corrected for the exposure and from which the particle background (shown in green) was already subtracted. In blue is shown the best fit for the remaining component of the background, accounting for the sky emission. Below that is shown the χ^2 of the fit as a function of the radius. *Right panel:* the final brightness profile (in black) from which also the sky background was removed.

Point-like sources and substructures As mentioned in the last section of the thesis describing the pipeline, we can use the CIAO function wavdetect to create a region catalogue file indicating a list of objects positions and areas to remove from the image in this way.

³⁵One could argue that the particle background image we simulated and the particle background component in our simulated observation should not strictly be the same as they depend on the many casual unfocused detections of the instrument which do not pass through its mirror. It's not a topic on which this project wanted to focus on, but one might measure that anyhow their difference is zero at all radii with a good approximation.

Pyroffit simply let us remove these regions from the input files even before extracting a brightness profile for them using the attribute `regions("region/file/path/file.reg")` for the data structure containing them.

In **figure 32** is shown the brightness profile from the same WFI simulation based on a *Chandra* image shown in **figure 31**, from which were not removed the point-like sources around the clusters.

These sources' influence made the observed cluster brightness profile less smooth. This might directly affect the density profile derivative and, even though we found out their presence did not change the overall mass profile drastically, when the sources were not masked the mass profile production algorithm tended to work slower and produce rougher deprojected profiles around the radii at which the point-like sources were located.

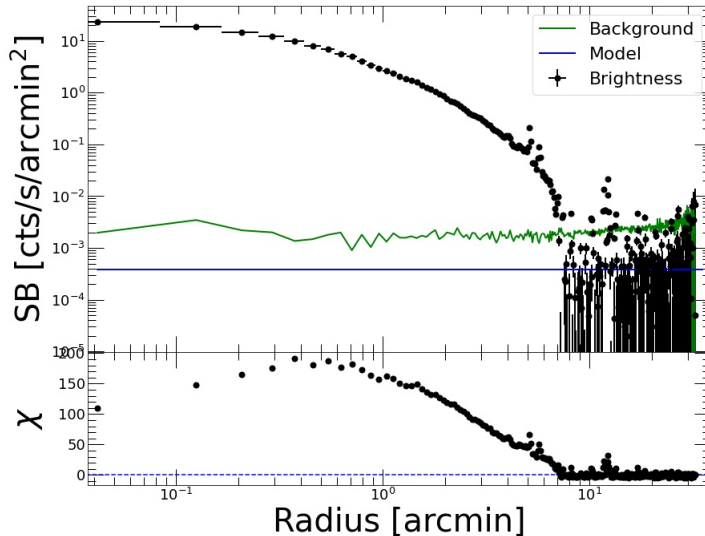


Figure 32: Brightness profile of the same simulated object shown in **figure 31**, with un-masked point-like sources around the cluster. Their presence is visible at around 5" and 10", where unusual brightness peaks are visible.

Removing regions was a particularly interesting feature for this project since we started working with simulated clusters and we thus had at our disposal as input maps with infinite resolution, no background and data from the only clusters and the larger substructures surrounding it. With that, we were finally able to verify the possibility for WFI to observe directly the sub-structures brightness and explicitly measure their brightness influence in the overall mass estimate for the cluster in its outer regions!

The results of this analysis are extensively discussed in the next section of this work.

4.1.2 Analysis of toy-model objects

In the early stage of the analysis development, before thinking about the quantitative results and the comparison between *Chandra* and WFI simulated images, we worked with toy-model objects to better understand the functioning of the scripts measuring the brightness profile, with all the parameters mentioned above

Namely, we analyzed the brightness profiles of a point-like source with a power-law spectral model and an extended source checking if the results of our simulation respected our expectation for their brightness profiles.

We also used these tests to understand qualitatively how interacted the flux from the SIMPUT creation function, the values on the input counts and parameter maps, the exposure time, the parameters of the function with which we calculate the brightness profile and this profile shape and height at its maximum. The number of these interacting terms, the many processes in which they are convoluted and on which the participants do not make them relate linearly between each other, but for example, we found out that the brightness profile did not seem to be influenced noticeably by the norm of the input counts map, while its value at all radii increased uniformly with increasing exposure time and flux.

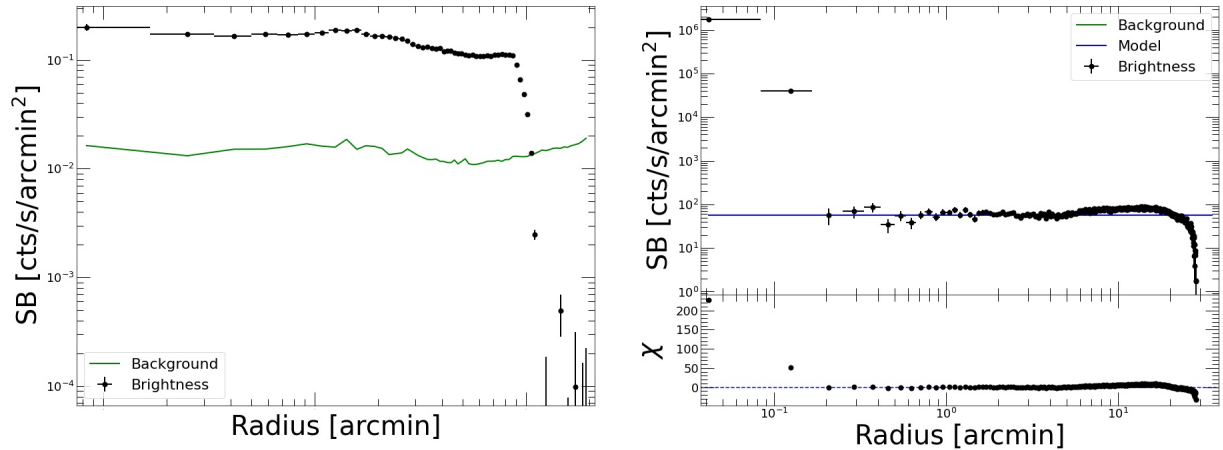


Figure 33: Brightness profiles of the extended constant-brightness circular source and of the point-like source are shown in the left and right panel, respectively. While for the former is visible how the brightness stays around the same value for all its length, dropping after its border; for the latter is appreciable how the point-spread function of an unresolved source make it look like a slightly larger object on the instrument sensor, which still shortly disappear under the background.

This is not shown here, but we also tested how an error on the source coordinate choice would have influenced the brightness profile and we found out that because of the almost circular nature of these sources such an error would have caused visible oddities on the profiles, such a "centre" less bright than its surrounding in the case of the point-like source and a smooth descending profile on the border for the constant brightness source. This can be translated for a more realistic object with similar effects on its centre and outer region, which we tried to monitor in our analysis.

4.2 Temperature and abundance profiles

As explained in the previous section, from the fit of the energy spectrum extracted from a series of concentric annuli centred on the source, we derived a radial profile for the observed temperature.

Like the observed brightness profile, the temperatures we can directly measure from our simulated images are not those we directly compared from the profiles derived from the real *Chandra* images using CIAO, but it still gave us a diagnostic instrument to analyze the quality of our pipeline results.

First of all, since the beginning of the pipeline development and while working with input maps derived from *Chandra* observations, we produced all our cluster simpups using temperature maps as a parameter

file. In particular, we decided to use simple temperature maps formed of concentric annuli in which the circularly-averaged temperature was restrained within a certain value range.

This choice might seems too gross, as it required an assumption on the temperature radial symmetry in our sources, but it allowed us to better compare our input values from the map with our spectral fit results, which we used to produce a radial temperature profile, as shown in **figure 34**:

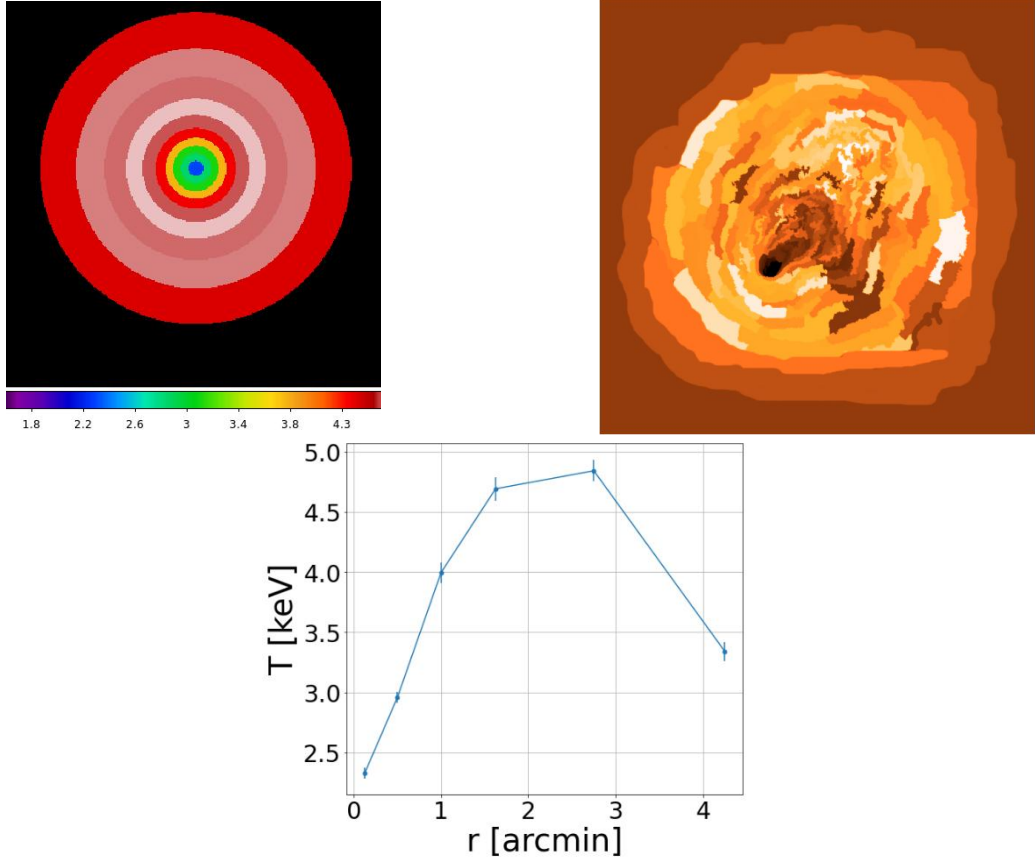


Figure 34: *Top panels*: comparison between two temperature maps for different objects. Simple radially symmetric maps we produced from *Chandra* data of Abell 133 for our comparisons and a more complex mosaic map in which each cell is in the same temperature range in the left and right panels, respectively. *Bottom panels* temperature profile for Abell 133 derived from the simulated image that received as an input the map showed on the top left. It is visible that within a reasonable margin this profile follows the map values.

After the first phase of the pipeline development with *Chandra* comparison was ended and we started working with simulated clusters, we also started using more realistic temperature maps with a mosaic distribution and with which it was much harder to directly relate the temperature profile.

4.2.1 The elephant in the room: WFI vs X-IFU

While we can consider ourselves completely satisfied with the brightness profiles we obtained with our simulations, it must be clear and repeated that WFI is not an instrument designed with the idea of measuring spectra with superior precision and we can imagine it always used in combination with Athena's other instrument: X-IFU.

X-IFU has a smaller field of view, but a larger spectral resolution than WFI and even if they have comparable effective areas at all energies, its properties would make spectroscopies much easier than how it would be only using the imager for measuring energies.

In the development of this pipeline and the analysis code, we had to work many times on the details of the temperature detections because we found a few different times in situations in which small changes could give us a remarkably better spectral fit and hence a much more precise temperature profile or one that could reach larger radii with its outer bins.

We did achieve our objective to create a rightful pipeline for simulating WFI observations and an analysis routine that gave us remarkably precise mass profiles, but if in the future this kind of work could be expanded to build a similar project for X-IFU we could expect much more exciting results from our simulations of Athena future possible observations of galaxy clusters. In this future we would probably produce a large field observation of a cluster with WFI at first, to later make many different observations in smaller areas of interest using X-IFU and merge their results to analyze the source as best as possible.

Toy-model analysis: flat temperature profile In figure 35 is shown as an example that might give a better insight into the complexity in extracting a precise temperature profile using WFI, that also shows another reason because of which we analyzed temperature maps with radial symmetry instead of working with even simpler toy models as we did with the flat brightness profile.

We produced a simulated image for a source with a flat temperature map of $r = 10'$ as an input and a flat count map of the same size. We would expect to derive from that a flat temperature profile at $\sim 15 \text{ keV}$ through the spectral fit of this simulation, but instead, we found a profile with almost correct results just in the intermediate area between $3'$ and $7'$, with incompatible values at the centre and edges of the map.

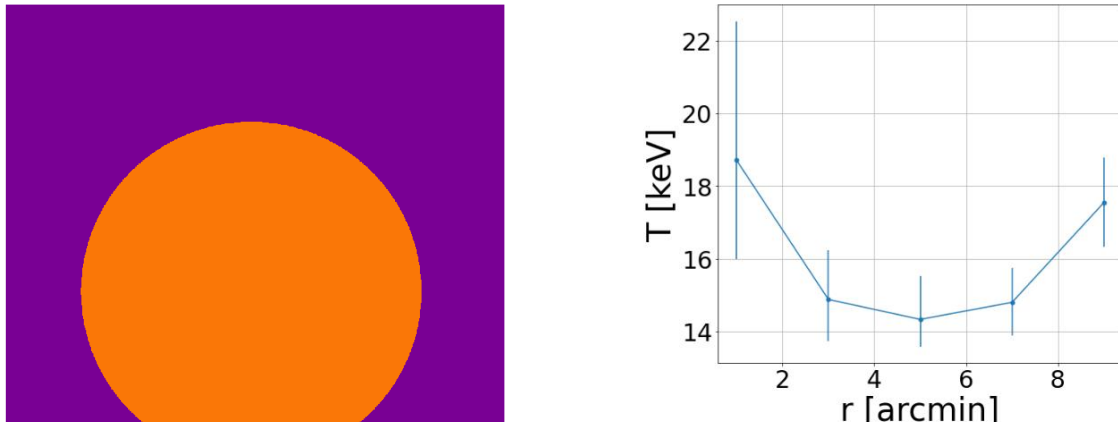


Figure 35: Simple flat circular temperature map at $\sim 15 kT$ and the temperature profile derived from the spectral fit of the simulated image produced with that map as an input in the left and right panel, respectively.

This particular case, which one could expect to be the most simple, could be affected by a multitude

of issues regarding the computational work during the simulation pipeline or the spectral fit and for what concerns the outer edge of the profile, there could be an issue with the fit on their boundaries.

In any case, this simple toy model showed us how the temperature profile relation with the input temperature maps could not be simply studied with a scaling complexity as in the case of the brightness profile and that we needed to produce more realistic objects to analyze.

4.3 Deprojection and Forward Method

After storing the images in a data structure and using them to calculate the observed brightness profile and fitting the spectra to calculate an observed temperature profile, we have finally reached the point in which we can deproject those profiles and calculate a radial mass profile for our source.

The hydromass library comes in very handy for this purpose, as it deprojects³⁶ and calculate the mass profile all with one operation.

4.3.1 Instrumental corrections and cosmology

The last few steps before the final calculation are the correction of the brightness and temperature observed profiles for the PSF and taking into account the cosmological model and the instrument calibration file referring to the effective area.

Cosmological model choice As for the cosmological model, we used the *astropy.cosmology* class to choose the values of the densities values for matter and cosmological constant.

These parameters influenced primarily the fine definition of distance from our source and hence our estimates for its size. Because of that, when comparing our WFI profiles with *Chandra* analysis we had to match their cosmological models. In particular our *Chandra* data were analyzed under the assumption of a **Flat λ CDM cosmology** with:

$$\begin{cases} \omega_{\Lambda,0} = 0.7 \\ \omega_{m,0} = 0.3 \\ \omega_{b,0} = \omega_{m,0} - \omega_{DM,0} = 0.06 \\ H_0 = 70 \text{ km/s/Mpc} \end{cases} \quad (20)$$

After the calibration phase of the project, when we started analyzing WFI simulated observations of simulated clusters, we continued using this cosmological model as it was compatible with the one used by the 300project³⁷, which referred to the 2015 Planck results³⁸ for their parameter choice.

The focus of this was not to evaluate the relation between the cosmological parameters and the cluster x-ray mass³⁹, but one might use the pipeline we developed just with that purpose as the simulations do not require any assumption on the sources' redshift or the cosmological model and their analysis can use them as parameters for the deprojection.

³⁶Pyprofitt documentation [39] clarify this is achieved.

³⁷see [1] as a reference

³⁸see [32]. In this review of their results, the Planck Collaborations showed that their evaluation was still compatible with a λ CDM model.

³⁹As it was described in works such as [49] and [7]

PSF correction An important step for the deprojection of the profiles is linked to the characterization of the WFI point-spread function.

As already explained, each instrument PSF varies as one gets further from the sensor centre, with its full-maximum half-width increasing. With our latest information, we expect WFI point-spread function to be remarkably stable, staying between 5" and 15" from the centre to a region at 30' far from it. I'm telling this again because anyone might probably want to correct for the PSF their profiles with different functions at each radius, but pyroffit does not have yet a way to receive as an input a PSF Fits file with images of the function at different radii and in different energy bands⁴⁰. Because of this, we had to model the psf with a single function, found fitting the PSF profile at the centre of the WFI calorimeter. What we found is a **King function** with equation:

$$\left(1 + \frac{r^2}{r_0^2}\right)^{-\alpha} \quad (21)$$

with $r_0 = 0.0883981'$ and $\alpha = 1.58918$.

This might seem like a big source of inaccuracy, but we can take into account the stability of WFI's PSF at larger radii considering our results. Anyhow with months passing, the publication of hydromass coming soon along with the continuing publication of updated Athena calibration files, we know this PSF issue will be taken care of.

Pyroffit handle the **PSF correction** of each profile building a so-called *mixing matrix*, which describe the leaking of photons between each annulus and the other. An example is showed in **figure 36**.

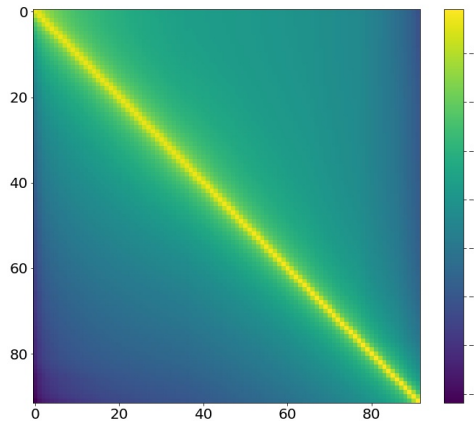


Figure 36: In this matrix is shown how big is the fraction originating at each annulus that is recorded on any annulus

The correction is easily achieved calling a method for the brightness and temperature profile and specifying the fitting function and pixel size. For example:

```
spec_data.PSF(pixsize=2.5/60., psffunc=fking)
```

⁴⁰More precisely, pyroffit has got a way to read a file as PSF, even with many images in it, but it does not have a way to know its pixel size implemented yet. See the section about pyroffit.profextract module in [39] for more information.

ARF and RMF Whilst extracting spectra we had the opportunity to generate corrected ARF files for each bin using the *SIXTE_arfgen* function to consider the vignetting effects, as the response of the detector decreased further from its centre, during the analysis and deprojection process pyroffit could consider the two response file just in one point, as for the PSF.

Furthermore, as already mentioned many times, both SIXTE documentation, pyroffit and hydromass and WFI calibration files are still being developed at the moment and SIXTE implementation of new calibration files is not direct.

Because of these reasons, we decided to stick to a single functioning version of each software and instrument calibration file, using for the data analysis the same ancillary response file and response matrix file. None of the software or calibration files received a major release during our work, but we expect them to come in the future⁴¹.

Pyroffit requires information on the two response files for converting the counts used to calculate the brightness profile into an emissivity measure. It does so⁴² calculating a numerical conversion factor, derived through XSPEC. In particular, the python code asks XSPEC to simulate an absorbed $pabs^*APEC$ model with an emission measure of 1 and derive the corresponding count rate. A linear proportion gives us the count rate-to-emissivity conversion factor.

This operation is made under the hypothesis of working with profiles already corrected for vignetting, as we are. This implies the count rates are rescaled to equivalent on-axis count rates and that an on-axis effective area of the telescope, as our is, have to be used for this conversion.

4.3.2 Forwarding method and Mass profile derivation

Hydromass gave us a few possible ways to derive a mass profile, both **parametric** and **non-parametric**, the forward method.

A parametric solution would assume a priori the density profile shape, which in the case of a galaxy cluster could reasonably assume to follow a Navarro-Frank-White profile⁴³ or more probably an Einasto profile⁴⁴, as these are the two shapes that better fit our actual observation of relaxed clusters⁴⁵.

A hypothesis on the shape of the gravitational potential of the galaxy cluster could be used for any kind of analysis of simulated WFI data, but because with this project we aimed to explore the outer regions of galaxy clusters, which we never observed before, it could be problematic to assume their density profile, especially at larger radii. Because of that we finally decided to use the non-parametric forward method to measure $M(r)$.

Forward method In the **forward method**, the hydrostatic equilibrium equation is solved fitting functional forms to the deprojected gas density and temperature profiles with no assumptions on the shape of the gravitational potential, while taking into account projection and PSF effects.

The computation is based on a Markov chain Monte Carlo algorithm (MCMC) which is completely managed by the library and based on the manipulation of functions from the pymc3 library⁴⁶. As a rule

⁴¹In particular SIXTE received an update during 2021 which did not influence our workflow, pyroffit was updated a few times for minor changes which did not influence our results either and WFI calibration files received a single release involving new ARFs. These files, released on the 18th of February 2021 have been differentiated between *field of view averaged*, *on axis* and *averaged within 5'*, but have not yet been included in the SIXTE instrument directory for WFI as their last release from 11th of November 2021, see [46]

⁴²here I'm using as a source of information pyroffit documentation, as comparing the code of its method `pyroffit.deprojection.cal.emissivity`, applied to a brightness profile object, works as hydromass' method `hydromass.Mhyd.emissivity`, applied to a data structure containing information between others, on the brightness profile.

⁴³see [28]

⁴⁴see [42]

⁴⁵see [50]

⁴⁶see [38]

of thumb, we decided to write our code not interfering with the computation, only choosing the maximum number of samples from the before taking into account the estimate of the posterior; and the maximum number of tunings for each iteration, which are various kinds of parameter adjustment that the code used to find a better solution faster reducing initial randomity.

As we expected to work with a solution with a regular and monotonous profile, we chose to use a lower number of tunings, 100 in most cases; and because we tried to maximise the accuracy of our results while keeping the computation cost and time low, we chose to use a larger but contained number of samples, between 1000 and 2000, in regard of the complexity of the cluster.

Diagnostics from mass radial profile observation The production of the mass profile is a step in our analysis code during which we decidedly do not have many ways to interact with the code, but it being the last part of this code and of the overall simulation process, we could analyze its results to be sure there was no evident error during the previous steps. This even before an eventual comparison with *Chandra*'s analysis of the same objects.

In particular, the few physical assumptions that needed to always be true and could be violated by a fallacious numerical solution are two:

- the cumulative mass profile $M(R) = M(r < R)$ must be a monotonously increasing function of radius at all radii, for obvious reasons.

This condition was not always achieved at all radii with the analysis of the most perturbed objects such as the bullet cluster. Usually, if there was no error in the code, this kind of unphysical results could be corrected by changing the MCMC parameters and with a longer computation.

- Hydromass calculate together with the total cumulative mass profile, also the cumulative baryonic mass⁴⁷ profile of the cluster. This simply by multiplying the density profile (which is derived from the gas emission) and the spherical volume at each radii⁴⁸.

The second assumption we always want to be true by simply watching our profiles is that the total mass must always be greater than the baryonic mass, for obvious reason, but we also want to see a baryonic fraction M_b/M_{tot} close to the cosmological values of $\sim 20\%$ in the case of the flat ΛCDM model. This is because, as already said, clusters can be considered to be cosmological probes, especially far from their centre and from the regions which might be interested in the turbulent motion of matter.

Figure 37 shows an example of a cumulative mass profile for simulated WFI observation of Abell 1413, created using *Chandra* data as an input, with a plot representing the comparison with its baryonic fraction and the expected one. This case does not show any pathological features and could probably be compared with the *Chandra* analysis of the same objects without any issues.

⁴⁷To be precise, it is the gas mass profile as we're not considering the mass in stars, which we expect to be a negligible fraction of the total for our interests anyhow.

⁴⁸This requires a hypothesis on the density distribution shape, but we consider the effect of the morphology of the cluster negligible in the order of magnitude estimate of this mass for most clusters.

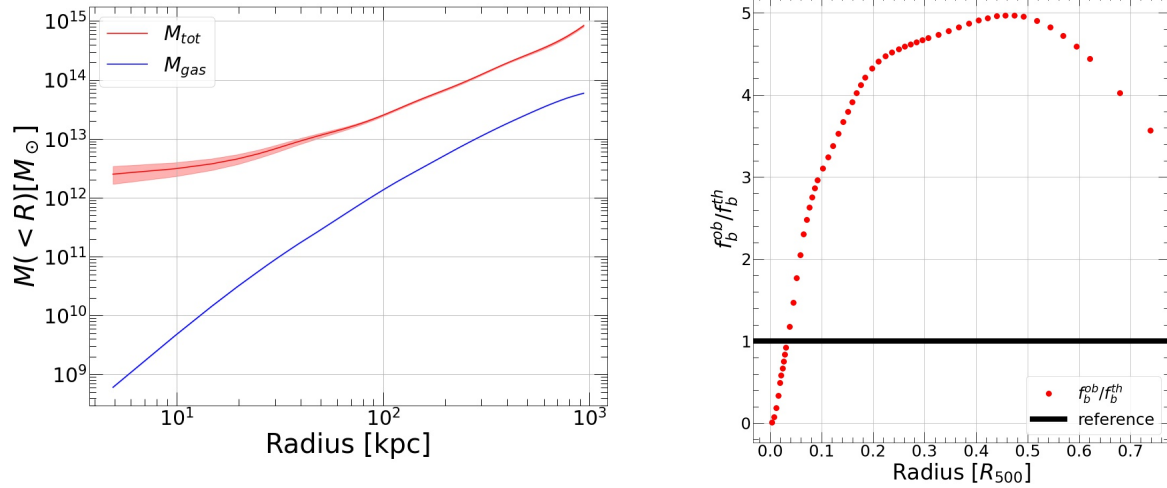


Figure 37: Cumulative total mass profile and gas mass profile as a function of the radius for Abell 1413 and its barionic mass fraction in the left and right panels, respectively.

4.4 Comparison with *Chandra* analysis

Between other things, in the next and last section of the thesis, I will show the results of the comparison between simulated WFI images of galaxy clusters and *Chandra* analysis for the same objects.

Now I want to show instead what considerations I took into account to compare profiles derived by different instruments and using different numerical methods and I will also try to explain how working with *Chandra* comparisons helped the development of the analysis code.

4.4.1 Choice of the sample

When developing this code and with the whole public *Chandra* data archives at our disposal⁴⁹ we tried to understand if there were any rational criteria to choose the objects for our calibration through comparison.

Because the aim of this thesis was not to modify SIXTE or find any precise results about the physics of clusters, we did not need a large population of galaxy clusters for our comparison.

With our small group of fewer than 10 objects we could have wondered whether it was better to analyze only the most symmetric and relaxed objects as we would expect them to be closest to the hydrostatic equilibrium condition in all their volume, and hence the one with the easiest to calculate mass profile with our algorithm. This was not the case, as works like the analysis of the HERitage project from the CHEX-MATE Collaboration from 2021⁵⁰ showed indisputably that the galaxy cluster population of the universe is very diverse there are not more relaxed, symmetric and unperturbed objects than perturbed and complex ones. Choosing to analyze just the formers would create a bias in our calibration which could have made it less consistent and less ready to analyze one of the many more structured objects.

Because of this, we decided to analyze objects with different shapes, from relaxed to interested in mergers; at different redshifts, between 0.057 and 0.87; and fluxes, between $\sim 10^{-10}$ and $\sim 10^{-13} \text{ erg/cm}^2/\text{s}$.

⁴⁹see [2] and [9]

⁵⁰see [47]

In the end, we were able to find a diverse and high-quality sample of observations with the only real selection we decided to apply was to use mosaic *Chandra* ACIS-I observations with the longest exposure time possible and the same instrument setting (VFAINT). This caution was needed to be sure of the quality of the observation, as a higher statistic was needed to be sure to compare our simulated images profiles to the largest radius possible with the limited *Chandra* real observations.

A few *Chandra* observations were discarded during the project, despite respecting our criteria, because of three main possible reasons:

- They presented evident instrumental defects on their images. This problem happened more often with recent *Chandra* images as ACIS-I CCDs developed some damages during the years.
- There was some flare or large unresolved source covering the cluster.
- Because simulating WFI images using them produced unluckily observations with the cluster between the four chips of the imager. In this kind of situation, an artificially high exposure time was needed to see the object exploiting the satellite dithering.

Comparing lengths As already mentioned, matching the cosmological model used for *Chandra* and SIXTE analysis assured us we were using the same definition of redshift z and hence that the two analyses used the same conversion factor from angular size to real size of the objects and could be compared directly on the same plot.

This also meant for us that even if *Chandra* and SIXTE profiles had points calculated on different radii, we could fit each profile with linear interpolations between each of their points and then calculate a ratio between the two results in any position, as shown in the example in **Figure 38**.

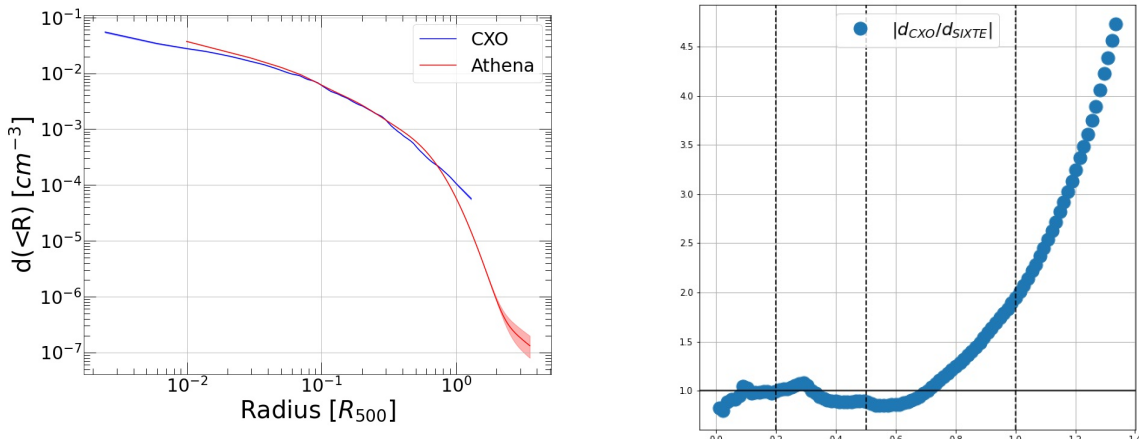


Figure 38: *Left panel*: example the comparison between the deprojected mass profile for Abell 1413 derived from *Chandra* data and the WFI simulation based on the same data. It is clear the difference between the "smooth" shape of the SIXTE profile, derived with a forward method, and the "edgy" profile from CIAO analysis of *Chandra* data, derived with a parametric method. *Right panel*: profile ratios between the two as a function of the radii.

Comparing deprojected profiles As already mentioned, our code based on the use of hydromass handles the brightness and temperature profile through a non-parametric forward method. On the other hand, the routine we used to analyze *Chandra* data and based on the software CIAO deprojects the observed profiles using a parametric algorithm.

The reason because of which we chose to compare the results of these two codes despite this difference is because of three main reasons:

- Some works compared the mass profile derived from *Chandra* and XMM-Newton observations using many different kinds of algorithms and stated that, at least up to our actual observational limit around R_{500} , the different mass estimates are negligible. **Figure 39** shows a plot from Bartalucci, Arnaud, Pratt & Le Brun⁵¹ and shows how values of M_{500} derived with different methods all lies within a $\sim 10\%$ range around the $M_{500}^{Y_X}$ reference value:

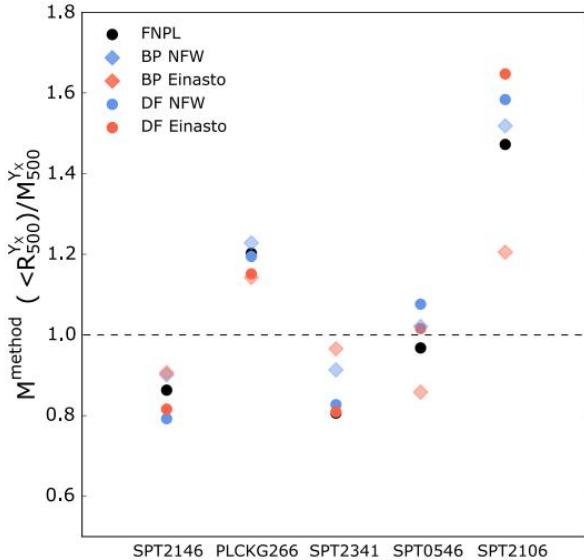


Figure 39: In this plot from [5] are compared the ratios between the the estimates for M_{500} obtained with different methods and $M_{500}^{Y_X}$. The listed methods are distinguished in forward non-parametric-like (FNPL), backward parametric (BP) and direct fits (DF) of Nafarro-Frank-White (NFW) and Einasto models. The work from which this plot comes from emphatise the consistency of this results in the radial range of the temperature profiles for most sources.

- The analysis pipeline for *Chandra* data and based on CIAO with which we worked is a well-known instrument already being used in many scientific contexts linked to *Chandra* analysis for many years and we can reliably consider its results as correct.
- As already stated, we decided to develop a code with the least amount of constraint on the cluster structure, because Athena and this kind of simulated observation could analyze the outer regions of these objects, which has never been seen before and on which we do not have a precise model yet.

⁵¹see [5]

Comparing brightness and temperature profiles The comparison between *Chandra*'s and WFI's deprojected brightness and temperature profiles was of particular interest for the calibration of our pipeline and calibration code. This is because these two types of profiles were similar to their observed counterparts, on which we could directly interact in many parts of the pipeline and analysis code. This was not the case for the density profiles and mass profiles, which were derived indirectly and with less interactable parameters for us to handle.

During many steps of the development, we found ourselves adjusting parts of the pipeline in the function of these plots, often finding issues with parts of the code we thought to be a long time correct.

In the case of the temperature profile, which had few and large bins and the largest error bars, we tried to check if the temperature values were compatible with those from *Chandra* analysis for sources with or without the sky background. This keeping in mind the known issue with the temperature real values, which is consistently different between *Chandra* and XMM-Newton measurement and thus made us a bit cautious while trying to calibrate our results in the function of *Chandra* temperature profiles. We decided a WFI simulated profile within a $1 \sim 1.5 \text{ keV}$ range from the *Chandra* analysis's results could be considered correct. In general, when we found any issue with the deprojected profile, they were traceable to a spectral fit issue, which made us review our fitting XSPEC code, or to any issue related to the instrument calibration file choice or PSF fit.

In **Figure 40** is shown example a temperature profiles comparison is shown. Here is interesting to note that the behaviour of the two profiles at larger radii is different, with Athena measurement in the observed kT values decreasing steadily. This is partly due to the fact we produced our simulations using cut *Chandra* images as an input, but also by the fact that our analysis often had different binning than *Chandra* analysis and hence they measured spectra and temperature in different regions, with a bin central radius value close one to the other. In general, we decided that this difference at larger radii was not an issue if the observed temperature profile of our simulation was consistent with the input map at the same radii.

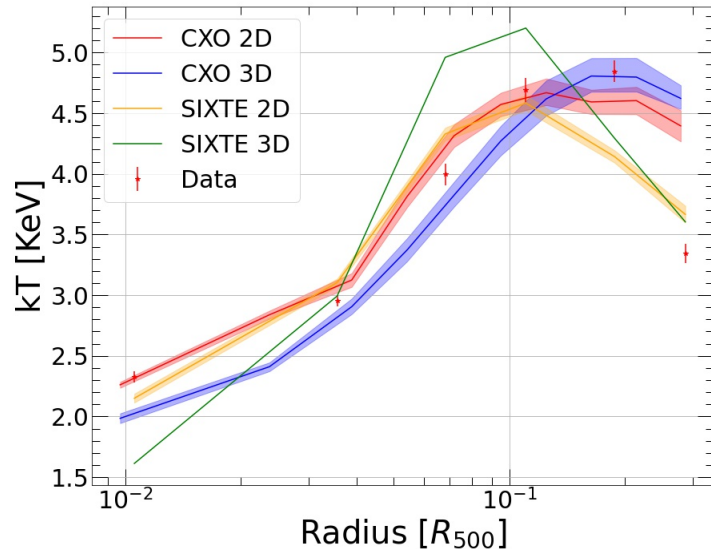


Figure 40: Temperature comparison between *Chandra* observed (CXO-2D) and deprojected (CXO-3D) temperatures and their analogous from our simulation (ATHENA-2D/3D) for Abell 133.

As far as the brightness profile is concerned, we often checked the behaviour of the profiles in three different regions:

- At lower radii, because WFI has a lower central PSF than ACIS-I, we expected the brightness from our simulations to have a steeper slope. This is because a larger point-spread function overlaps more bins, increasing the counts more than if it was thinner. When this condition was not respected we checked if it was connected to the PSF fit, the source centre choice or the input parameters for the SIMPUT creation, such as the source flux/
- In the intermediate range of the profiles, we always tried to check whether the profiles had the same slope, as this influenced directly the density and mass profile. This could be easily checked by analyzing if the ratio between the two profiles was constant at all radii.
- At higher radii the deprojected profiles suffered from the fact that working with input images from *Chandra*, the maximum radius at which the source was still visible is relatively low, often below $\sim 0.8 R_{500}$ and while our forward code was able to extrapolate the brightness profile even up to $\sim 1.2 R_{500}$ it was not a fit of the actual observed counts and often showed incoherent behaviours.

Anyhow WFI profiles at higher radii were still useful probes of the pipeline behaviour, where they were still comparable with *Chandra* profiles. For example, when WFI profiles were too steep at these radii it was a hint the brightness was probably over-subtracted and that we had to check the background flux and its image.

This figure shows a plot from an early version of the comparison between the deprojected brightness profile of Abell 133 as derived from *Chandra* data (CXO) and a WFI simulated image (Athena) in which some suspect effects of probable issues with the pipeline are visible:

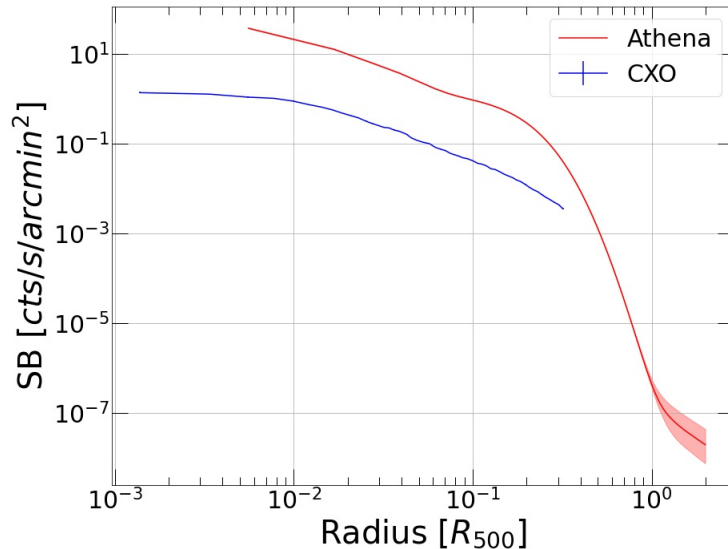


Figure 41: In this example is visible how at lower radii, below $\sim 2 \cdot 10^{-2} R_{500}$ the Athena profile become steeper because of WFI larger PSF but is also visible how in this case the profile was probably over-subtracted of the background as for $r \gtrsim \sim 2 \cdot 10^{-1} R_{500}$ it decreases more rapidly than *Chandra*'s profile.

4.5 Bottom line of the pipeline and analysis code development

The third and fourth sections of this thesis have been a long and dense technical review of most, but not all, passages of the actual form of the pipeline, at the time of writing this master thesis.

Here I have been trying to explain the logic and functioning of each part of the simulation and analysis codes, with their limitations and the logic behind the choices I made.

This is just a summary of the results of development that lasted more than 10 months and it was not supposed to show all the solutions that have been tried and discarded for every problem, but only the solutions that lead to the final version of the code.

This whole project was developed with the scientific goal of analyzing the mass profile of galaxy clusters at outer radii with Athena-WFI simulations. In the next section, I will show and analyze my results in this regard, but as the simulation pipeline and analysis codes I developed could be used in many other case scenarios, I uploaded them on a GitHub page with a manual and a few example⁵².

At the moment, a couple of students involved in thesis projects linked to Athena have already used it and, if the interest grows, I will keep it updated with the last calibration files and software releases for anyone to use in the future, maybe trying to make it give more consistent results.

⁵²see [30]

5 Results

In the first part of this final section of the thesis, I will show the **results** of our **calibration process**, based on the comparison between *Chandra* analysis of real observations and the analysis of simulated WFI observations of the same objects made using *Chandra* data as an input. Then, in the second part, I will show the results of the **analysis** I made on a small group of simulated clusters produced in the context of the **300project**⁵³ and gracefully given us by Dr Elena Rasia.

All the plots are averaged on our whole samples, but in the appendices of the Thesis are shown the single results for each comparison and simulation. The use of an average does not simply have the advantage of synthesising the results in a more approachable expression but is a necessary passage needed to describe as a whole the many possible diverse profiles of a galaxy cluster, which as already stated, may largely vary in their shapes and relaxations⁵⁴.

The profiles are normalised on their own M_{500} and/or R_{500} . Because I could not normalise each length and mass for two values at the same time, the M_{200} and R_{200} values shown are derived as $7/10 M_{500}$ and $7/10 R_{500}$. This approximation is good on average but does not fit each singular object's properties. Anyhow, it was displayed just as an intuitive indication of the radii reached with our analyses.

The reason behind this analysis I want to stress out again the fact that the problem of the mass estimate of galaxy clusters is an active field of research for modern cosmology, not only linked to their X-ray observation; but with this master thesis project, I did not intend to produce a precise or extensive physical analysis on that topic. My project mainly consisted in producing a piece of software that could generate and analyze a realistic simulated observation from Athena WFI and could be used to preview future physical insight Athena could give us after its launch and its capabilities.

Nevertheless, the physical application of this code I'm showing is not just an example of the use it could be applied to, as it shows some of the reasons for which the development was needed. It is not just a demonstration of the code's performances and its capabilities but an explicit preview of the possible results that could be obtained using it with a larger data sample and more rigorous analysis.

Another important fact to note again here is that the calibration process was necessary to us to make sure we were developing a functioning simulation pipeline, but it suffered to some complications probably linked to the quality and shape of the current WFI instrumental calibration file and the current state of the software used in the pipeline, particularly SIXTE, which is still under development and not fully documented yet. This thesis' aim was not to solve the calibration files and software actual deficiencies either: I only tried to produce a functioning pipeline with the current technologies and information.

The results are positive and speak for themselves, but the whole pipeline will probably be updated in the future and will probably benefit from more realistic pieces of information about WFI specs. I tried to keep the code version-independent and instrument-independent in this optic.

⁵³see [1]

⁵⁴see again as a reference on the large variance in the galaxy cluster population [47], but it is also interesting to see how even recent papers such as [48], which analyze single perturbed objects find highly unanticipated results regarding the cluster's mass profile. In the case of this article from Umetsu, Ueda, Hsieh et al. from March 2002, the authors found out that the mass estimates for Abell 370 from its Chandra observation and weak-lensing measures differ by about 50%! This is extraordinary and can be linked to the peculiarity of this cluster and shows again how the high variability in clusters need us to analyze a large sample to understand their common features and their physics.

5.1 Chandra Comparison

In the case of our Chandra comparison, it is immediately noticeable both from the comprehensive plots and the single comparisons how we could not reach R_{500} with most of *Chandra* observations.

In particular, watching the single source comparisons in the **Appendix A** we see the original Chandra analysis often could reach a radius around R_{500} with the brightness profiles (and hence the density profiles), but their temperature profiles do not reach such radius. *Chandra* analysis could overall produce a mass profile up to a fraction of R_{500} .

The actual image we used as an input for our WFI simulations put a strong limit on the radii we could reach with their analysis because even when our python code could extrapolate a continuation for the observed profiles during the deprojection at larger radii than the maximum observed, our simulations did not have at their disposal data on the regions the Chandra telescope did not capture photons from: we cannot simulate the regions of an object which are not visible in the input image. Moreover, even if our analysis code extrapolated some of the deprojected profiles at larger radii than the Chandra analysis could when comparing the two results we could only calculate the ratio of the profile values at radii for which analysis had a solution. Hence the less penetrative Chandra analysis often limited the maximum radii reachable with our comparisons.

This issue should reasonably not be caused by the quality of the particular Chandra images we used for our comparison as they were selected for being unperturbed and very clear and all had a long time exposure of at least 90 $ksec$, so we can consider them to be the best possible *Chandra* results at our disposal.

It can not be caused by the cut we did on the Chandra counts map used as an input for our simulations either, as we always applied it to a region with a radius at least larger than R_{500} with the exact objective of seeing at least as far as the Chandra original analysis.

The inaccuracies found with our calibration could be possibly addressed in the code implementation or in the instrumental calibration files we've had at our disposals. We expect them to be reduced in the future when this issue will be addressed.

This overall difficulty in comparing for all the different objects our simulation analysis results with that of the original *Chandra* data at any larger radius of interest as R_{500} or R_{200} (the former close to the actual observational limit and the latter close to clusters virial radius) led me to the choice of averaging the *Chandra* and WFI profiles ratios of all objects at all radii and then calculate the average value of this curve at all radii. But I also tried to evaluate it between 0.3 R_{500} and 1 R_{500} for density and below 0.65 R_{500} for temperature.

The choice of the **boundaries** for the second and third radii intervals might seem arbitrary, but are linked to my attempt of considering a region within which the comparison between *Chandra* and simulated WFI data was not affected by the instrument differences:

- Because of the difference between the central PSF value of *Chandra* and WFI I expected the counts below a certain radius to be enhanced for *Chandra*, which systematically showed a steeper brightness, density and mass profile below a certain radius. This does not affect the spectroscopy and thus the temperature profile.

Observing the different objects I chose to consider radii larger than 0.3 R_{500} to avoid the region within which I think this effect was relevant.

- Between the few objects of which Chandra analysis could see at radii larger than R_{500} there are some perturbed and asymmetric objects and between them the bullet cluster, which is formed by two sub-clusters moving apart. Considering for the brightness analysis radii greater than R_{500} would mean, with my restricted Chandra observation sample, to consider a large bias from this cluster's brightness and density profile which is not representative of the whole and diverse cluster population.
- When considering the temperature profile I found out that the analysis of WFI simulated objects could reach larger radii than most of their Chandra counterparts. In these cases, the binning choice

and actual shape of the temperature radial profile from *Chandra* data used as an input parameter map for the simulation influence drastically and in some uncontrolled ways the profile ratios at radii which I found out to be for most objects larger than about $0.65 R_{500}$.

This is more evident observing how the last points in the single source comparisons showed in Appendix A tend to diverge from the profile seen in *Chandra*.

Average densities ratio In the case of the **average density ratio** we can see how with the notable exception of Abell 2204⁵⁵, most WFI analyses had a density profile close to the *Chandra*, particularly below $0.6 R_{500}$.

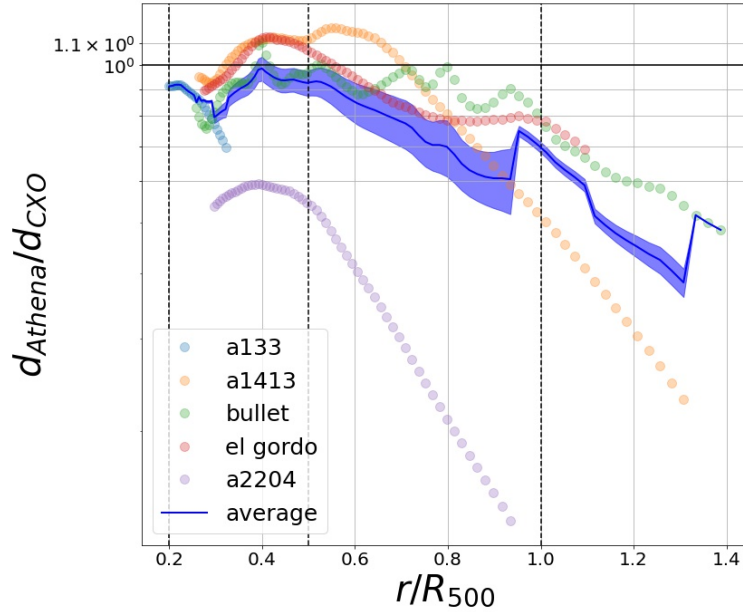


Figure 42: Profiles of the ratio between *Chandra* and simulated WFI density profiles. The blue polygon represents the average value and its 1σ dispersion.

As a whole, the average density ratio was found to be below 1 for many but not each object even when not considering the central regions affected by the different PSF effects and the profiles at larger radii. Excluding the obvious outlier, we would get much closer to unity, but this would create a selection bias in our sample.

$$\begin{cases} d_{CXO}/d_{Ath} = 0.793 \pm 0.029 & \text{for all } r \\ d_{CXO}/d_{Ath} = 0.832 \pm 0.012 & \text{for } 0.3 < r/R_{500} < 1.0 \end{cases} \quad (22)$$

⁵⁵For what concerns Abell 2204 by a best-educated guess, as I did not find any error in its simulation, is that it is a very concentrated object with a peak brightness within 6-12'', the PSF effect influenced the central parts of the object and as a result whole estimate for its density profile and its deprojection

Average temperature ratio The **temperature ratios** show a much more diverse situation, with ratios below and above the average value.

As a whole, this affected the average ratio to be close to unity but with a large 38% variance considering all radii.

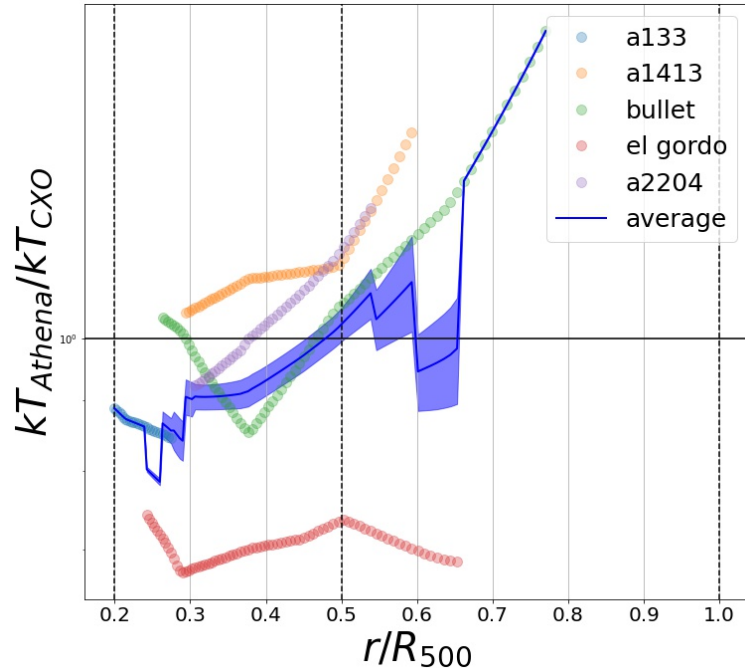


Figure 43: Ratio profiles of the *Chandra* and simulated WFI temperature profiles. The blue polygon represents the average value and its 1σ dispersion.

Interestingly enough, the average on a restricted radii interval made the average go further from unity but decreased its error. This might be due to El Gordo being an outlier⁵⁶ or might represent a systematic underestimate of the temperature with our simulation pipeline⁵⁷.

$$\begin{cases} kT_{CXO}/kT_{Ath} = 0.993 \pm 0.385 & \text{for all } r \\ kT_{CXO}/kT_{Ath} = 0.834 \pm 0.011 & \text{for } 0.3 < r/R_{500} < 0.65 \end{cases} \quad (23)$$

Average mass ratio The limited radio reachable by most of the temperature profiles of *Chandra* datasets have the side effect to also impose a limit to most of *Chandra* **mass profiles** and hence to our comparison with WFI simulated profiles and what I expect to be the effect of different PSF between *Chandra* and WFI is still visible in these profiles at lower radii. Nonetheless, it is interesting to see that this time again, the scatter of different mass profile ratios is almost equally distributed below and above unity, meaning that

⁵⁶This might come from the fact that El Gordo is a particularly disturbed cluster, which is visible despite its high redshift because of its large mass. A lower density of counts give us less spectral information and hence make the temperature derivation much harder

⁵⁷The latter hypothesis might sound unfounded as we would expect to be close to unity analyzing data based on the same image, but other users implementing my pipeline found out the same temperature bias.

we do not observe any appreciable bias in our simulation results and the average mass ratios is still around unity for most radii.

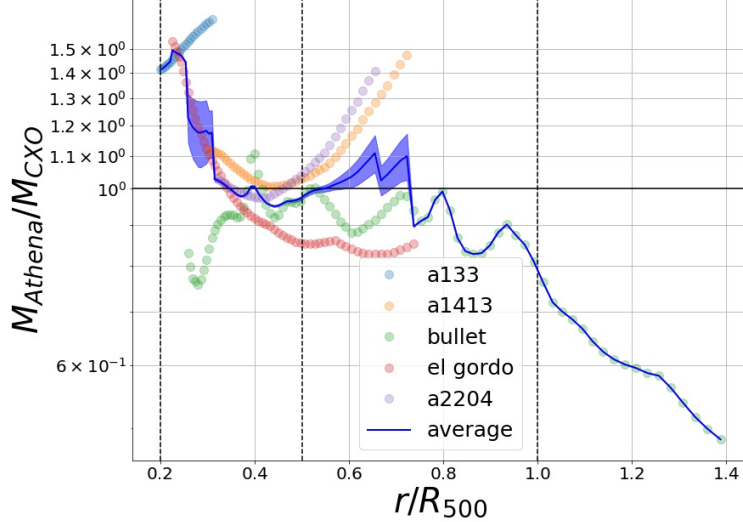


Figure 44: *Chandra* and simulated WFI mass profiles ratios. The blue polygon represents the average value and its 1σ dispersion.

The average ratio in a restricted range of radii has still a value around unity, but with a lower error. The average with radii restricted between $0.3 R_{500}$ and $1 R_{500}$ has a lower value, probably because of the outlining bullet cluster profile at larger radii. This would also explain how the average with radii restricted between $0.3 R_{500}$ and $0.65 R_{500}$ was not affected by it.

$$\begin{cases} m_{CXO}/m_{Ath} = 1.000 \pm 0.062 & \text{for all } r \\ m_{CXO}/m_{Ath} = 0.9835 \pm 0.0055 & \text{for } 0.3 < r/R_{500} < 1.0 \\ m_{CXO}/m_{Ath} = 1.006 \pm 0.002 & \text{for } 0.3 < r/R_{500} < 0.65 \end{cases} \quad (24)$$

This is overall a splendid result, which gave us an almost unbiased systematic error linked to the pipeline accuracy in evaluating every system mass, especially at larger radii which will be the main region of interest for Athena, when it will work alongside *Chandra* and XMM-Newton.

With the certainty of the quality of our simulations, we considered the 6% accuracy of our mass calibration at all radii as the top systematic error for all mass estimates in our analysis of simulated clusters. This error could be reduced with a larger *Chandra* observations sample but is already enough to prove our point and show the potentiality of this pipeline in the analysis of cluster mass profiles at larger radii as we will demonstrate with the analysis of the simulated clusters profiles.

If we prepared a more rigorous analysis with a larger sample we could have also thought of using the reduced radii interval average ratio uncertainty as a systematic error related to the calibration but in our example, it is sufficient to show how even our worst-case estimates with no hypothesis gave us yet a small baseline calibration error.

5.2 Simulations

With our calibration completed, we finally managed to analyze a small sample of simulated clusters given to us by Dr Elena Rasia and produced with cosmological structure formation simulations by the 300project⁵⁸ for a ΛCDM universe. As already explained, with this analysis we wanted to **foreshadow** the possible results regarding the outer regions of galaxy clusters: whether Athena could see them, if it could see the **faint substructures and clumps** of gas falling into them and whether the **hydrostatic equilibrium hypothesis** holds or not for them.

Seeing the sub-structures As expected with its large **effective area**, the first results we achieved was to find out that Athena could effectively capture photons from the outer regions of clusters, being able to measure their brightness over the background as far as to R_{200} . This is observable indirectly from the analysis of the profiles, but also directly from the comparison between the input maps and the simulated WFI images.

Figure 45 shows an example of a simulated cluster (with its substructure) as seen from Athena WFI. This object simulated observation was obtained using the same flux and background flux of Abell 1413 with which we analyzed the *Chandra* observation. The main difference is that, as for the WFI simulation based on the *Chandra* observation, we produced this image with a 20 ksec exposure time, while the original mosaic picture from *Chandra* for Abell 1413 lasted around 115 ksec. This is not to be considered unique, as we found out analogue results for all our simulations: WFI could see the substructures and the outer regions of the central core of clusters with an exposure time fraction of what *Chandra* and XMM-Newton would need to see just its innermost and more luminous regions.

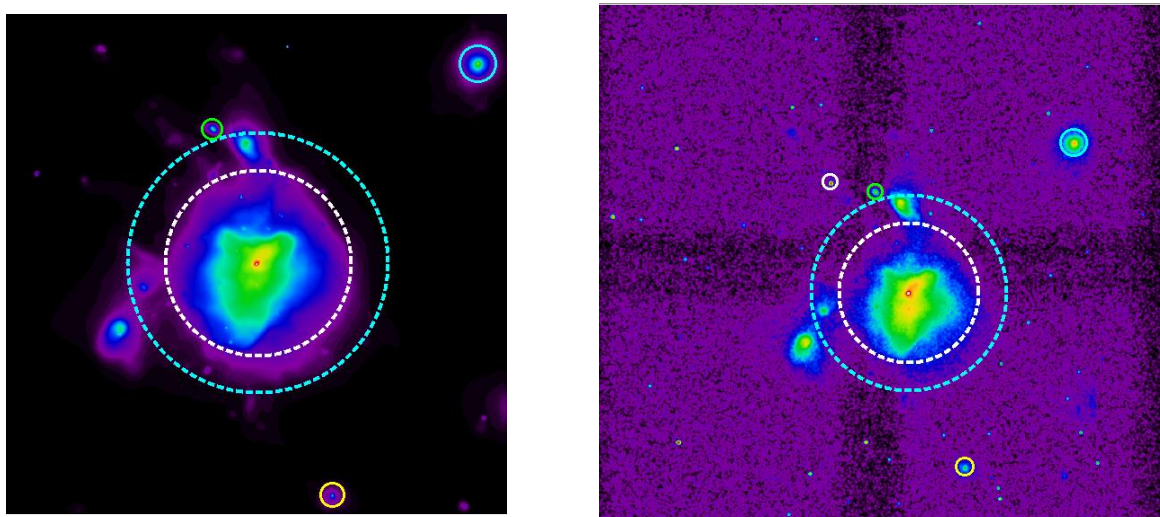


Figure 45: Simulated cluster input map with no background and the simulated WFI image of that cluster made using the same flux and background flux used for the analysis of simulated Abell 1413 images in the *left* and *right panel*, respectively. It is evident how the substructures are still visible in the WFI image even at larger radii. It's also interesting to note how even the smaller structures in the original Image did suffer from an artificial deformation due to the PSF. The circles surrounding them have the same physical size between the two pictures, while having different radius on the simulation and on the simulated image. The dashed white line represent the source's R_{500} and the dashed blue line represent its R_{200}

⁵⁸see [1]

Figure 45 also shows an example of how the stability of WFI's **PSF** grants us the possibility to tell apart larger clumps from point sources' PSF. See for example how the clump on the top right of the image and the smaller clump in the yellow circle on the bottom almost kept their original proportions relative to the central object even if they are at the border of the WFI 70'-sided calorimeter, while the point-like sources we added to our simulation with a custom SIMPUT file kept their size regardless of their position on the image.

The only ambiguity could be generated by something like the smaller clump in the green circle on top of the cluster. In the image, it has a size similar to the width of the PSF at the same radii, as it can be seen comparing it with the point-like source in the white circle I placed on its left. Probably this kind of small clump could be distinguished just with a redshift measurement or by trying to see it with another telescope such as *Chandra*, with a smaller central PSF width.

Mass profiles The **main scientific goal** I've tried to accomplish with this project is to observe the **mass profile** of galaxy clusters, especially in their **outer regions**, and try to understand whether the hydrostatic equilibrium hypothesis holds there or how big could be the deviation from it.

To do this the first analysis I did on my sample of simulated WFI images was to compare the average M_{500} value we derived for them with its known true value.

Despite one of the simulations being an outlier for which was not possible to extract an estimate for its M_{500} and although the different objects have different shapes and relaxations, the average ratio between the observed values of M_{500} and their true values was incredibly close to unity, with an error of just around 3.6%, which added to the systematic error from the *Chandra* comparison gives us a 9.6% error on the average mass estimate, with a 0.08σ tension from the expected value.

$$M_{500}^{obs} = 1.008 \pm 0.036 \pm 0.06 M_{500}^{true} \quad (25)$$

Again, this meant for us that on average we could measure the total cluster mass independently from their peculiarities with good approximation, but this does not apply to a single object in general, as they are very diverse. Our results are shown in **Figure 46**.

Substructure contribute As already explained, current researches are using numerical simulations to evaluate how large could be a **non-thermal pressure term** linked to the turbulent motion of the gas in perturbed clusters and in the region in which clumps falls into them and how this pressure term could affect the hydrostatic equilibrium and hence the cluster total mass X-ray measure⁵⁹.

To investigate the possible influence of the observation of the faint substructures on the total mass estimates, I produced WFI simulated images of the same clusters of which I had already analyzed the mass profiles masking out from their input map the larger substructures surrounding the clusters.

The results are interesting because the mass profiles for images with masked substructure had again a very good estimate for the average measured to observed M_{500} ratio, with a slightly higher value and yet another uncertainty of around 3%, not considering the systematic calibration error of around 6%. This corresponds to a tension of 0.005σ from the expected value, slightly bigger than in the previous case.

$$M_{500}^{obs,nosubs} = 1.048 \pm 0.0315 \pm 0.06 M_{500}^{true} \quad (26)$$

⁵⁹see [15]

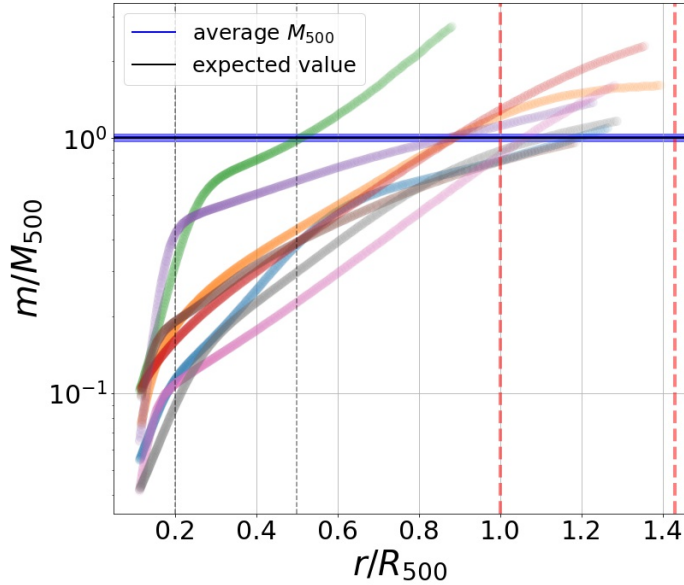


Figure 46: WFI M_{500} and M_{500} true value ratio. Each simulated object mass profile is derived from the analysis of its WFI simulated image.

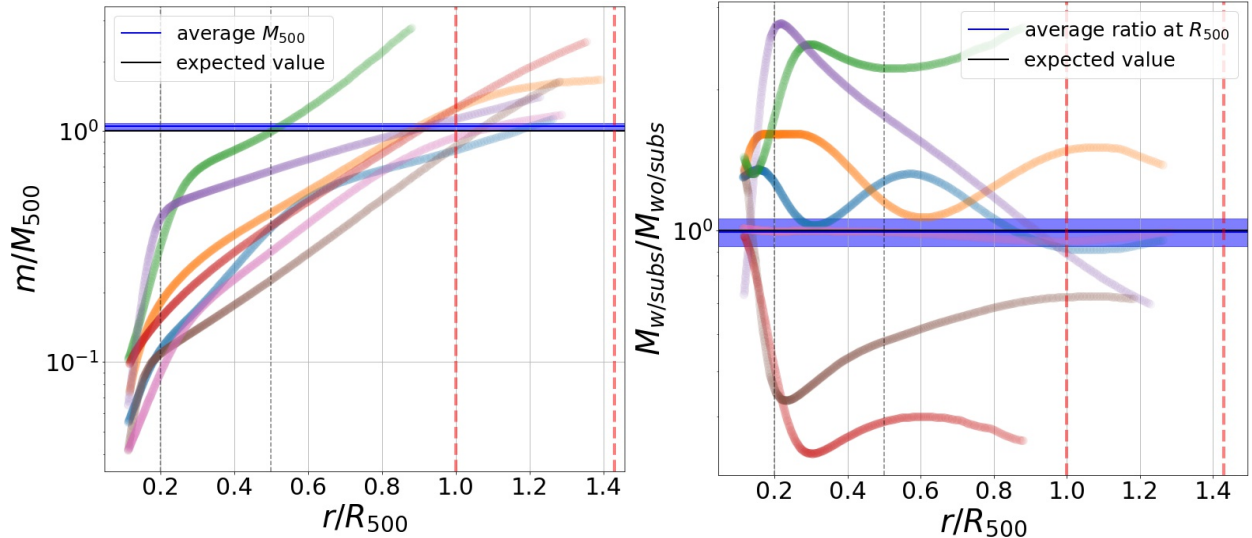


Figure 47: On the left panel are shown the mass profiles for simulated cluster with masked out substructure. On the right panel the ration between the mass for the same objects in the case with or without considering substructures.

Comparing the M_{500} estimates with the substructures visible or masked, we find that on average their ratio is very close to unity at their R_{500} , but we can also see in **Figure 47** how these ratios are very diverse between different sources and varies a lot at different radii. Nonetheless, it is interesting to see that they seem to converge when approaching larger radii, even though the most perturbed objects showed diverging ratios and some of their anal did reach R_{500} with a resulting overall dispersion of around 18%.

$$M_{500}^{w/\text{subs}} = 0.993 \pm 0.067 \pm 0.116 M_{500}^{w/o/\text{subs}} \quad (27)$$

Barionic fraction Another important factor to keep in mind when analysing galaxy cluster outer regions is their relation to the **universe's large-scale structure**. A first way to check whether our results are compatible with estimates for some cosmological parameters is to compare their **gas fraction** f_{gas} at larger radii with the **baryonic fraction** in the universe Ω_b/Ω_m .

What we found is that our simulated images' fraction of gas as a function of radii have diverse profiles depending on the peculiarities of each source, but above R_{500} they still show on average to have a gas fraction compatible with the many expected value of 0.20 ± 0.4 .

We also checked if the results were noticeably influenced by the choice of masking out or not the possible substructures and clumps surrounding the cluster, finding out that in the first case the discrepancy between our result and the expected value was about 1.5σ viewing the substructures and 2σ masking them out the image. This shows again indicatively how observing the faint and less luminous object around a cluster not only improve its total mass estimates but also its performance as a cosmological probe.

$$\begin{cases} f_{\text{gas}}(R_{500}) = 0.227 \pm 0.017 \\ f_{\text{gas}}^{w/o/\text{sub}}(R_{500}) = 0.234 \pm 0.017 \end{cases} \quad (28)$$

In **Figure 48** are shown the different gas fraction profile for the simulated WFI images of the simulated clusters, its average value at their R_{500} and the expected cosmological value for Ω_b/Ω_m :

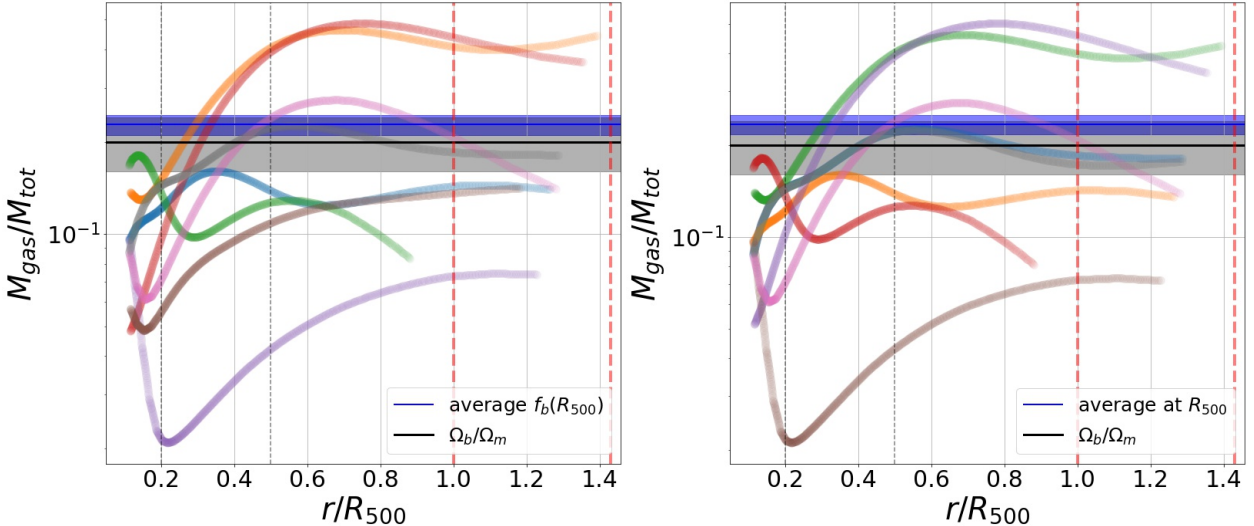


Figure 48: Gas fraction for our simulated images with the substructures is visible and the same profiles for the simulated images with the substructures masked out in the left and right panel, respectively.

6 Conclusion

The **discrepancies between galaxy cluster mass estimates** based on observations in different bands is a yet open topical issue of modern astrophysics, that links our understanding of their dynamics and structure to the measure of cosmological parameters. The 3σ tension found by the Planck collaboration between its estimates for σ_8 from the CMB power spectrum and the cluster number counts underlines how crucial this measurement is.

The measurement of the cluster mass in **X-ray** relies on the assumption that the ICM is in **hydrostatic equilibrium** with the gravitational potential generated by the cluster total mass. The validity of this assumption is fundamental to understand the origin of this tension, as the cluster mass measurements are calibrated on X-ray. The picture is not clear. The X-ray masses should be at least 50% biased higher to account for the 3σ tension. The comparison with weak lensing measurements finds generally the X-ray masses to be on average only 15% **bias** at R_{500} [37], suggesting that the **non-thermal pressure** support is high at such radius. Furthermore, recent studies based on the **baryon fraction** [15] finds that on average the non-thermal support is of the order of few percents, suggesting that there may be also systematic in the lensing. Moreover, the measurement of the baryon fraction at R_{500} for many cluster yields values which are close to the cosmological value. For these reasons, it is fundamental to address the systematic in the mass measurements performed using X-ray in the **outer parts**. The study of these regions have always been hampered by the intrinsic difficulty of observing them. That is, the emission of the cluster at R_{500} is very faint. Furthermore, the emission is often affected by the presence of **point-like sources** and which masking is often difficult due to instrumental effects.

In this context, **Athena** will be a game changer as it will allow us for the first time to measure the properties of the ICM with high precision, giving us the possibility to investigate this topic.

With this thesis project, I **developed and calibrated a simulation pipeline** with which is possible to produce mock Athena-WFI X-ray observations of galaxy clusters using the ray-tracing simulation software SIXTE.

I have **analyzed** the physical properties of galaxy clusters from cosmological simulations, with particular attention to their radial mass profiles and their outer regions, which we will directly see for the first time thanks to the Athena telescope, with its unprecedented specs.

Our **calibration** consisted of the comparison between *Chandra* observation analysis made with CIAO and the analysis of WFI simulated image produced starting from the very same *Chandra* images. What we found is that as expected with WFI we could observe larger brightness than *Chandra* with a fraction of the exposure time and that our mass estimates differ with their comparison by a factor between 0.5 and 6%, depending on whether we decide to consider a restricted range of radii or all of them, hence ignoring the instrumental effects affecting the ratios. We used the largest of these discrepancies as a **systematic error** for all our subsequent analyses to check whether our worst possible results with no supplementary hypothesis could give us coherent results when analyzing simulated objects of known mass.

Analyzing simulated WFI observations of **simulated objects** of known properties we appreciated, the capabilities of the imager, which showed us most of the faint **clumps and substructures** surrounding the clusters and it was also clear how WFI's stable **PSF** made it easier for us not to mistake point-like sources close to the sensor edge for larger substructures in the cluster potential. All of this for sources with fluxes comparable with those of real objects and backgrounds we analyzed in our *Chandra* comparison, but with a fraction of the **exposure time** needed to *Chandra* to see just the central part of the cluster.

We found out that our simulated WFI images estimated correctly the M_{500} of our clusters on average, with an uncertainty of less than 10% even considering the systematic comparison error both considering or not the emission from the substructures and clumps eventually surrounding the clusters. This distinction did not affect our gas fraction f_{gas} estimates, which proved in both cases to be consistent with the actual

estimates for Ω_b/Ω_m , making clear one more time that galaxy clusters' outer regions can be used as a **cosmological probe** for the density values of the universe.

We also showed how the **average ratio** between M_{500} estimates for our objects These results are coherent with the work of *Eckert, Gherardini, Ettori et al. from 2019*, in which comparing the results of their numerical simulation with that of other previous researches, they predicted that a **non-thermal pressure** support term linked to turbulence could influence the mass estimate for a factor below 15 – 20%.

With a larger sample of clusters and smaller systematic error from the *Chandra* comparison calibration we might have found even tighter error bars for our results, but we can consider ourselves satisfied with this result as it demonstrates the possibilities this pipeline could grant with a more sophisticated analysis of the simulation results.

If this result was confirmed with higher precision, it would prove how even the most perturbed and turbulent cluster outer regions would not deviate from the hydrostatic equilibrium enough to justify the mass bias observed with weak-lensing measures and above all Planck 3σ tension with a correction on the X-ray mass profiles we could justify with Athena observations.

In any case, with this thesis, I **produced** and **released** a **functioning calibrated** piece of **software** with which might be possible to **foreshadow** many different **Athena physical results** not only regarding the galaxy clusters or their mass.

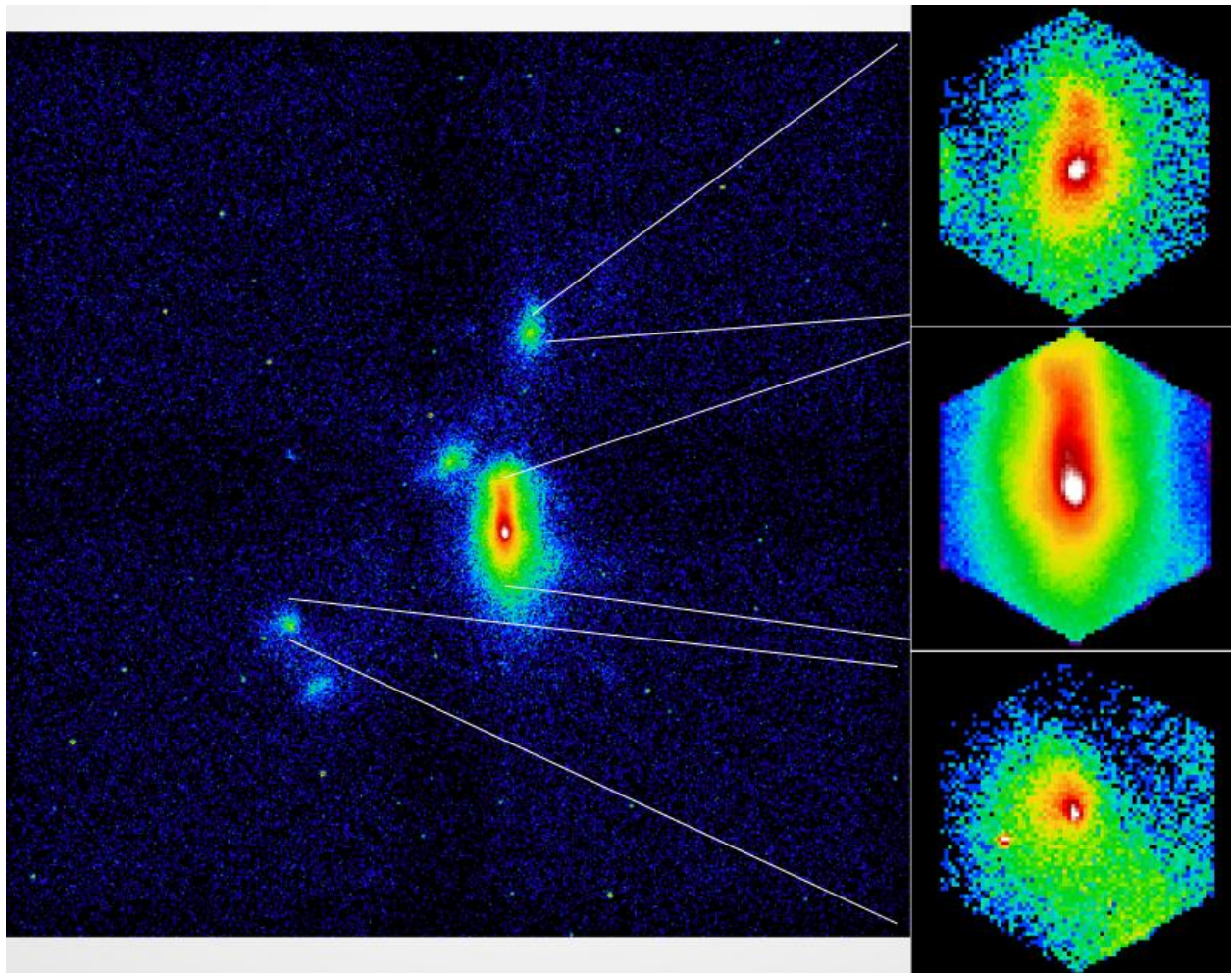
This code could be also used as a baseline to produce an analogue pipeline for simulating realistic simulated **X-IFU** spectra. Such a development would allow us to analyze much more accurate spectra from our simulated objects and hence derive a more precise temperature profile for them, but also analyze the emission from the faint substructures and **dark matter filaments**, if we worked with data from simulations that also included considerations on the matter composition and not only on its mass.

This code could be also used as an important **planning toolkit**. In the next few years, before Athena will be launched, we will have at our disposal X-ray data from thousands of clusters thanks to the **E-Rosita full-sky survey**, but also another large of weak lensing measurement for the same kind of objects thanks to the **Euclid project**, which will open us the door for a large collection of multi-wavelength observations.

If we start building a **follow-up observational strategy** for Athena, we will be able to predict how long should be our exposure time to see a source as a function of its flux and the condition of its surroundings and also think about any possible localised long exposure X-IFU observation we might want to take of some point of interest of any source.

The last **figure** of this thesis with which I want to close the discussion about my project is a *simulated composite mock-up observation of a simulated cluster* with some substructure surrounding, made of a WFI 20 ksec image and 3 20 ksec X-IFU observations.

With Athena, we will be able to see more than we were ever able to do with our current telescopes, extract spectra and capture X-ray photons which are still invisible to us now, and we might understand something more of the elusive largest self-gravitating structures in the entire universe. This is a preview I was able to show you with the result of my work and the help of my supervisors.



Bibliography

This is a complete list of the sources I've been using during the drafting of this text. I separated them into a few different categories according to their form and of the use I made of them.

Reviews and **books** have been my main source of general information, with the latters often being more updated than the formers, while also being restricted to a smaller range of topics. In particular, the review from Pratt, Arnaud Biviano et al. and *a panchromatic view of clusters of galaxies and the large-scale structure* from Plionis, Lopez-Cruz and Huges were the most fundamental sources of information about the mass estimation and measurement for galaxy clusters, both theoretically and numerically, with its influence on the cosmological parameters.

The two **Theses** I cited both contained nice reviews of the topic galaxy clusters and they both showed me how I could write this thesis, while also being useful sources of information about the topic of galaxy clusters and X-ray astronomy in general (both of them) and the use of SIXTE (Cucchietti, Kaastra, Monfardini et al.).

Between the many **Articles** I cited there are some of the most fundamental works on the topic I talked about in this thesis, from the density profile of clusters and the Y_X proxy, to their mass profile estimates. In particular, the work from Vikhlinin, Pointecouteau, Pratt and Eckert have been the most influential to the knowledge on which this thesis is based.

Other articles I cited could be linked to recent researches of which topic I did not talk about directly, but that I needed to cite as a baseline for my discussion or as examples about results within the topic of galaxy cluster physics, astronomy and their mass profile. In this category, we can certainly note the Planck collaboration results, which I also used as a reference for cosmological parameters, the CHEX-MATE results within the context of the HEritage project and the CCCP results on lensing.

The remaining references I've cited in this bibliography are the papers presenting the software I've been using and the **online resources**, such as the *Chandra* Data Archive and NASA's HEASARC WebPIMMs, that I've been constantly used to produce and analyze my data both from real sources and simulated objects.

I want to thank again my relator and supervisor Dr Iacopo Bartalucci for helping me constantly during the year I've been working on this thesis project and for presenting me generously and continuously the many sources here listed (up until March 2022!). They showed me how vast and lifeful is the field of x-ray astronomy and galaxy cluster physics. This is a complete list of the sources I've been using during the drafting of this text. I separated them into a few different categories according to their form and of the use I made of them.

Reviews and **books** have been my main source of general information, with the latters often being more updated than the formers, while also being restricted to a smaller range of topics. In particular, the review from Pratt, Arnaud Biviano et al. and *a panchromatic view of clusters of galaxies and the large-scale structure* from Plionis, Lopez-Cruz and Huges were the most fundamental sources of information about the mass estimation and measurement for galaxy clusters, both theoretically and numerically, with its influence on the cosmological parameters.

The two **Theses** I cited both contained nice reviews of the topic galaxy clusters and they both showed me how I could write this thesis, while also being useful sources of information about the topic of galaxy clusters and X-ray astronomy in general (both of them) and the use of SIXTE (Cucchietti, Kaastra, Monfardini et al.).

Between the many **Articles** I cited there are some of the most fundamental works on the topic I talked about in this thesis, from the density profile of clusters and the Y_X proxy, to their mass profile estimates. In particular, the work from Vikhlinin, Pointecouteau, Pratt and Eckert have been the most influential to the knowledge on which this thesis is based.

Other articles I cited could be linked to recent researches of which topic I did not talk about directly, but that I needed to cite as a baseline for my discussion or as examples about results within the topic of

galaxy cluster physics, astronomy and their mass profile. In this category, we can certainly note the Planck collaboration results, which I also used as a reference for cosmological parameters, the CHEX-MATE results within the context of the HEritage project and the CCCP results on lensing.

The remaining references I've cited in this bibliography are the papers presenting the software I've been using and the **online resources**, such as the *Chandra* Data Archive and NASA's HEASARC WebPIMMs, that I've been constantly used to produce and analyze my data both from real sources and simulated objects.

I want to thank again my relator and supervisor Dr Iacopo Bartalucci for helping me constantly during the year I've been working on this thesis project and for presenting me generously and continuously the many sources here listed (up until March 2022!). They showed me how vast and lifeful is the field of x-ray astronomy and galaxy cluster physics.

Reviews

- [21] Kravtsov A., Borgani S. *Formation of Galaxy Clusters*. *Annual Reviews of Astronomy and Astrophysics* vol. 50 (2012), pp. 353–409.
- [22] M. Birkinshaw. *The Sunyaev-Zel'dovich Effect* (1998). URL: [arXiv:astro-ph/9808050](https://arxiv.org/abs/astro-ph/9808050).
- [36] Possel M. *A Beginner's Guide to Working with Astronomical Data* (2019). URL: [arXiv:1905.13189](https://arxiv.org/abs/1905.13189).
- [37] Pratt G. W., Arnaud M., Biviano A. et al. *The galaxy cluster mass scale and its impact on cosmological constraints from the cluster population*. *Space Science Reviews* vol. 215 (2019), p. 25.
- [41] Reiprich T. H., Basu K., Ettori S. et al. *Outskirts of Galaxy Clusters* (2013). URL: [arXiv:1303.3286](https://arxiv.org/abs/1303.3286).

Articles

- [1] 300project Collaboration. “**The Three Hundred project: a large catalogue of theoretically modelled galaxy clusters for cosmological and astrophysical applications**”. *Monthly Notices of the Royal Astronomical Society* 480 (2018), pp. 2898–2915.
- [4] ArnaudK. A. “**XSPEC: The First Ten Years**”. *Astronomical Data Analysis Software and Systems V, A.S.P. Conference Series* 101 (1996), p. 17.
- [5] Bartalucci I., Arnaud M., Pratt G. W. & Le Brun M. C. “**Resolving the hydrostatic mass profiles of galaxy clusters at z 1 with XMM-Newton and Chandra**”. *Astronomy & Astrophysics* 617 (2018), A64.
- [7] Borgani S. & Guzzo L. “**X-ray clusters of galaxies as tracers of structure in the Universe**”. *Nature* 409 (2001).
- [12] Dauser T., Falkner S., Lorenz M. et al. “**SIXTE – The Generic X-ray Instrument Simulation Toolkit**”. *Astronomy & Astrophysics* 630 (2019), A66.
- [13] DES Collaboration. “**Dark Energy Survey Year 3 Results: Cosmology from Cosmic Shear and Robustness to Data Calibration**” (2021). URL: [arXiv:2105.13543v1](https://arxiv.org/abs/2105.13543v1).
- [14] DES Collaboration. “**Dark Energy Survey Year 3 Results: Cosmology from Cosmic Shear and Robustness to Modeling Uncertainty**” (2021). URL: [arXiv:2105.13544](https://arxiv.org/abs/2105.13544).
- [15] Eckert D., Ghirardini V., Ettori S. et al. “**Non-thermal pressure support in X-COP galaxy clusters**”. *Astronomy & Astrophysics* 621 (2019), A40.
- [16] Eckert D., Jauzac M., Shan H. Y. et al. “**Warm-hot baryons comprise 5-10 per cent of filaments in the cosmic web**”. *Nature* 16058 (2015).
- [17] Hoekstra H., Herbonnet R., Muzzin A. et al. “**The Canadian Cluster Comparison Project: detailed study of systematics and updated weak lensing masses**”. *Monthly Notices of the Royal Astronomical Society* 449 (2015), pp. 685–714.

- [19] Kaastra J. S. “On the use of C-stat in testing models for X-ray spectra”. *Astronomy & Astrophysics* 605 (2017), A51.
- [20] Kravtsov A. V., Vikhlinin A. & Nagai D. “A New Robust Low-Scatter X-ray Mass Indicator for Clusters of Galaxies”. *Astrophysical Journal* 650 (2006), pp. 128–136.
- [23] Mantz A. B., Allen S. W., Glenn Morris R. et al. “Weighing the giants—V. Galaxy cluster scaling relations”. *Monthly Notices of the Royal Astronomical Society* 463 (2016), pp. 3582–3603.
- [24] Nagai D., Vikhlinin A. & Kravtsov A. V. “Testing X-Ray Measurements of Galaxy Clusters with Cosmological Simulations”. *Astrophysical Journal* 655 (2007), pp. 98–108.
- [25] Nandra N., Barcons X., Barret D. et al. “The Hot and Energetic Universe” (white paper). URL: https://www.the-athena-x-ray-observatory.eu/images/AthenaPapers/The_Hot_and_Energetic_Universe.pdf.
- [28] Navarro J. F., Frenk C. S. & White S. D. M. “A Universal Density Profile from Hierarchical Clustering”. *Astrophysical Journal* 490 (1997), pp. 493–508.
- [29] Ota N., Nagai D. & Lau E. T. “Constraining hydrostatic mass bias of galaxy clusters with high-resolution X-ray spectroscopy” (2018). URL: [arXiv:1507.02730v3](https://arxiv.org/abs/1507.02730v3).
- [31] Planck Collaboration. “Planck 2013 results. XX. Cosmology from Sunyaev–Zeldovich cluster counts”. *Astronomy & Astrophysics* 571 (2014), A20.
- [32] Planck Collaboration. “Planck 2015 results. XIII. Cosmological parameters”. *Astronomy & Astrophysics* 594 (2016), A13.
- [33] Planck Collaboration. “Planck 2018 results. VI. Cosmological parameters” (2020). URL: [arXiv:1807.06209v3](https://arxiv.org/abs/1807.06209v3).
- [35] Pointecouteau E., Arnaud M. & Pratt G. W. “The structural and scaling properties of nearby galaxy clusters: I - The universal mass profile” (2005). URL: [arXiv:astro-ph/0501635v1](https://arxiv.org/abs/astro-ph/0501635v1).
- [40] Rasia E., Ettori S., Moscardini L. et al. “Systematics in the X-ray cluster mass estimators”. *Monthly Notices of the Royal Astronomical Society* 369 (2006), pp. 2013–2024.
- [42] Retana-Montenegro E., Van Hese E., Gentile G. et al. “Analytical properties of Einasto dark matter haloes”. *Astronomy & Astrophysics* 540 (2012), A70.
- [43] Laura Salvati, Marian Doussis, and Nabila Aghanim. “Constraints from thermal Sunyaev-Zel’dovich cluster counts and power spectrum combined with CMB”. 614, A13 (June 2018), A13. DOI: [10.1051/0004-6361/201731990](https://doi.org/10.1051/0004-6361/201731990). arXiv: [1708.00697 \[astro-ph.CO\]](https://arxiv.org/abs/1708.00697).
- [47] The CHEX-MATE Collaboration. “The Cluster HERitage project with XMM-Newton: Mass Assembly and Thermodynamics at the Endpoint of structure formation”. *Astronomy & Astrophysics* 650 (2021), A104.
- [48] Umetsu K., Ueda S., Hsieh B. et al. “Line-of-sight Elongation and Hydrostatic Mass Bias of the Frontier Fields Galaxy Cluster Abell 370” (2022). URL: <https://arxiv.org/abs/2203.03647>.
- [49] Vikhlinin A., Kravtsov A. V., Burenin R. A. et al. “Chandra Cluster Cosmology Project III: Cosmological Parameter Constraints”. *Astrophysical Journal* 692 (2009), pp. 1060–1074.
- [50] Vikhlinin A., Kravtsov A. V., Forman W. et al. “Chandra Sample of Nearby Relaxed Galaxy Clusters: Mass, Gas Fraction, and Mass-Temperature Relation”. *Astrophysical Journal* 640 (2006), pp. 691–709.

Theses

- [6] Bignamini A., Tozzi P. & Borgani S. “The Swift-XRT Survey of Groups and Cluster of Galaxies”. *Università degli Studi di Trieste, Dipartimento di Fisica*, A.A. 2008/2009.
- [11] Cucchetti E., Kaastra J., Monfardini A., Pajot F. & Pointecouteau E. “De l’astrophysique des amas de galaxies à la physique des microcalorimètres en rayons X: performances scientifiques et calibration du X-ray Integral Field Unit de la mission Athena”. *l’Université Toulouse*, A.A. 2018/2019.

Books

- [3] Arnaud K., Smith R. & Semiginowska A. *Handbook of X-ray Astronomy*. Cambridge University Press, 2012.
- [8] Carroll S. M. *Spacetime and Geometry, an introduction to general relativity, seventh edition*. Pearson, 2016.
- [34] Plionis M., Lopez-Cruz O. & Huges D. *A Pan-Chromatic View of Clusters of Galaxies and the Large-Scale Structure*. Springer, 2008.

Online Resources

- [2] *ACCEPT: Archive of Chandra Cluster Entropy Tables*. URL: <https://web.pa.msu.edu/astro/MC2/accept/>.
- [9] *Chandra Data Archive*. URL: <https://cda.harvard.edu/chaser/dispatch0cat.do>;jsessionid=oN88vGbwMpupAcesi3nCydTG2qKnJAw2R_.lcda2.
- [10] *CIAO Website*. URL: <https://cxc.cfa.harvard.edu/ciao/>.
- [18] *Hydromass, Python Package*.
- [26] *NASA's HEASARC: Tools - WebPIMMs*. URL: <https://heasarc.gsfc.nasa.gov/cgi-bin/Tools/w3pimms/w3pimms.pl>.
- [27] *NASA/IPAC Extragalactic Database*. URL: <https://ned.ipac.caltech.edu/>.
- [30] *Pipeline GitHub project page*. URL: https://github.com/RAGilardi/AthenaWFI_Sixte_Pipeline.
- [38] *PyMC3, Probabilistic Programming in Python Documentation*. URL: <https://docs.pymc.io/en/v3/>.
- [39] *Pyroffit, Python Package Documentation*. URL: <https://pyroffit.readthedocs.io/en/latest/index.html>.
- [44] *SIXTE Manual*. URL: <https://www.sternwarte.uni-erlangen.de/research/sixte/index.php>.
- [45] *Sixte Presentation Webinar*. URL: https://api.cloud.ifca.es:8080/swift/v1/AC0/Webinar/200511SIXTE_Webinar.mp4.
- [46] *SIXTE Website*. URL: https://www.sternwarte.uni-erlangen.de/research/sixte/data/simulator_manual_v1.3.11.pdf.

Appendices

A *Chandra* comparison plots

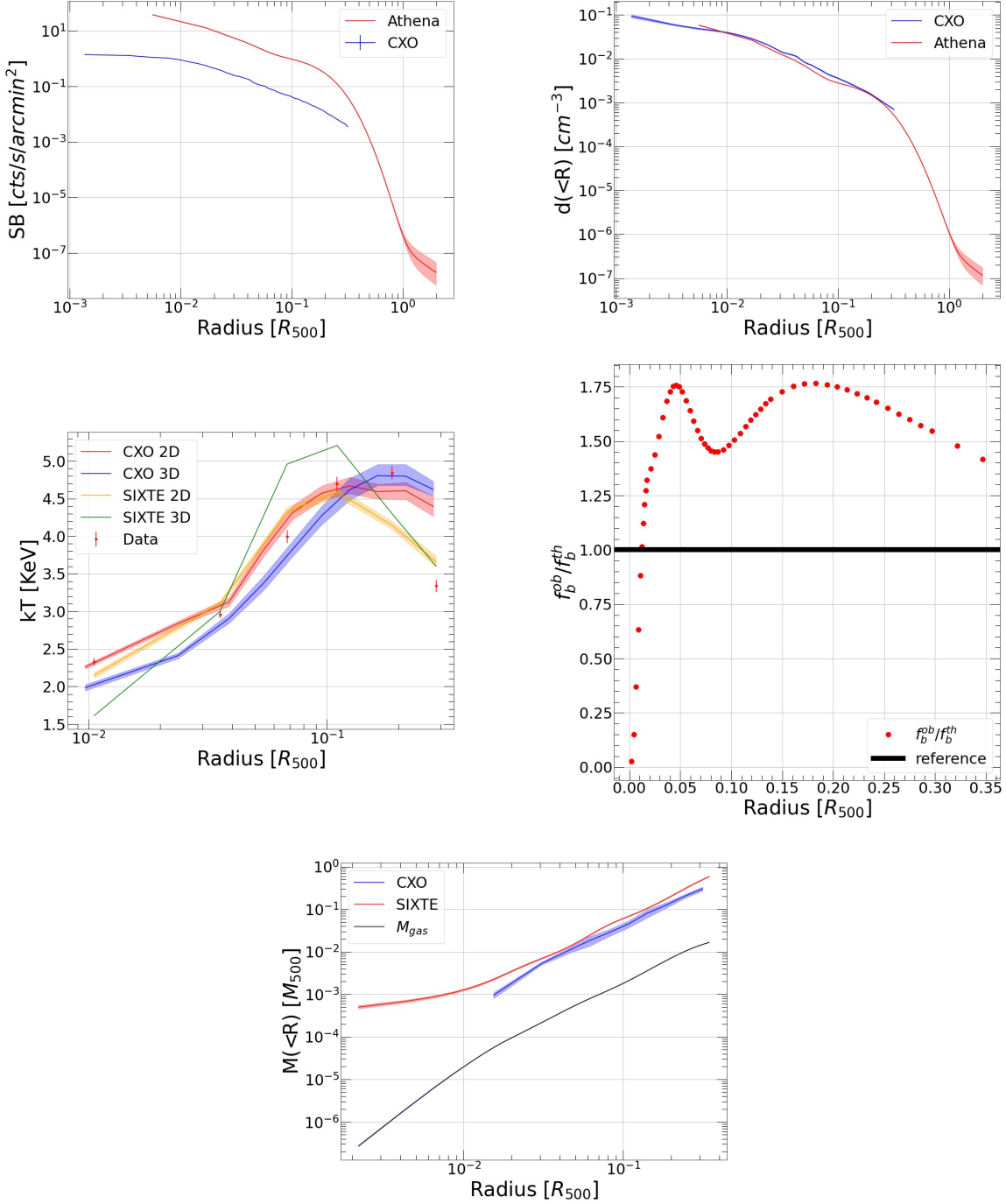


Figure 49: Abell 133: $z = 0.056$, $M_{500}^{CXO} = 2.84 \cdot 10^{14} M_{\odot}$, $R_{500}^{CXO} = 9.82 \cdot 10^2 \text{ kpc}$,
 $T_{exp}^{CXO} \sim 110 \text{ ksec} = 5.5 T_{exp}^{Ath}$

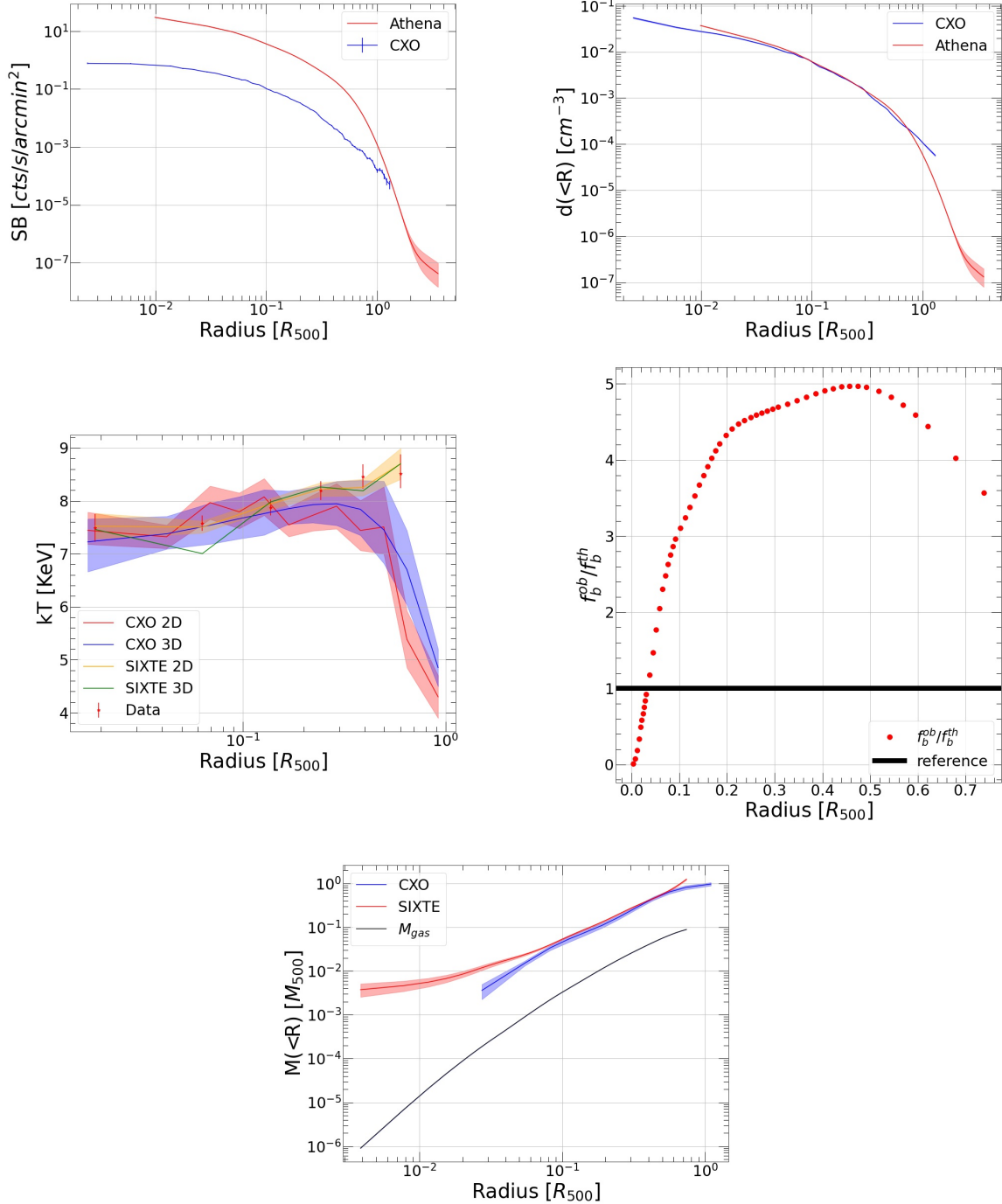


Figure 50: Abell 1413: $z = 0.144$, $M_{500}^{CXO} = 6.70 \cdot 10^{14} M_\odot$, $R_{500}^{CXO} = 1.27 \cdot 10^3 kpc$, $T_{exp}^{CXO} \sim 115 ksec = 5.75 T_{exp}^{Ath}$

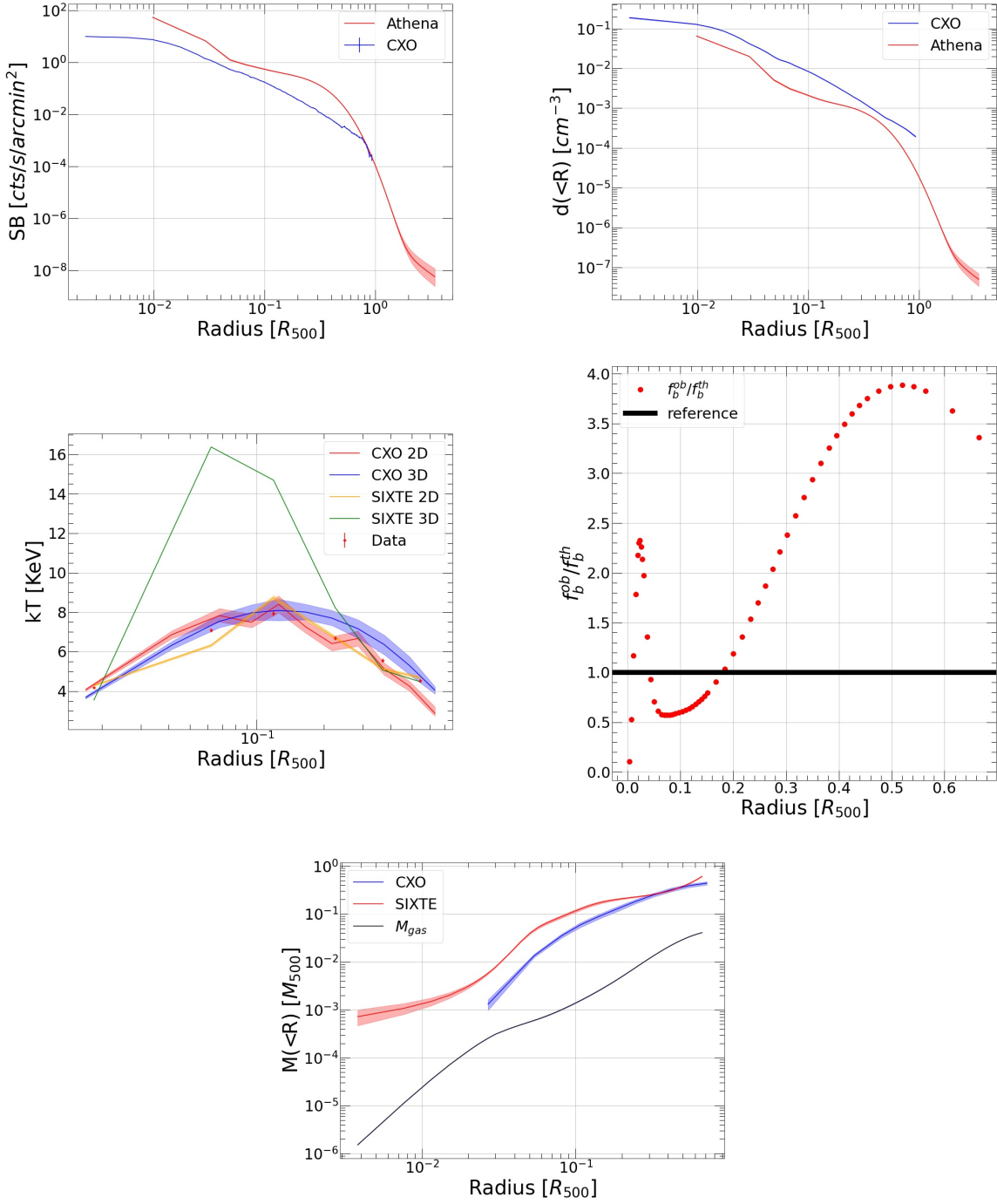


Figure 51: Abell 2204: $z = 0.152$, $M_{500}^{CXO} = 8.26 \cdot 10^{14} M_\odot$, $R_{500}^{CXO} = 1.36 \cdot 10^3 \text{ kpc}$, $T_{exp}^{CXO} \sim 90 \text{ ksec} = 4.5 T_{exp}^{Ath}$

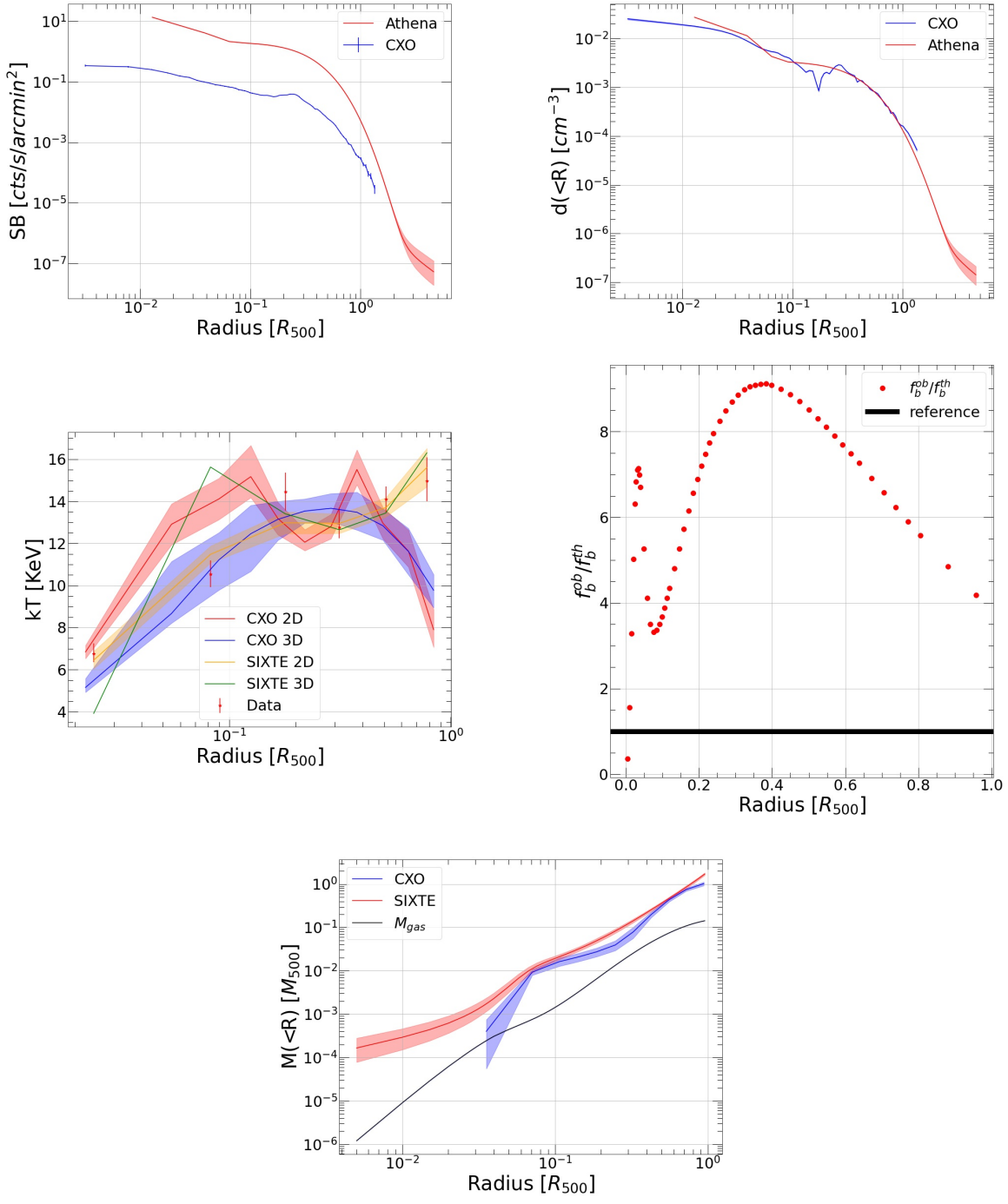


Figure 52: Bullet cluster: $z = 0.297$, $M_{500}^{\text{CXO}} = 1.95 \cdot 10^{15} M_{\odot}$, $R_{500}^{\text{CXO}} = 1.71 \cdot 10^3 \text{ kpc}$, $T_{\text{exp}}^{\text{CXO}} \sim 297 \text{ ksec} \sim 25 T_{\text{exp}}^{\text{Ath}}$

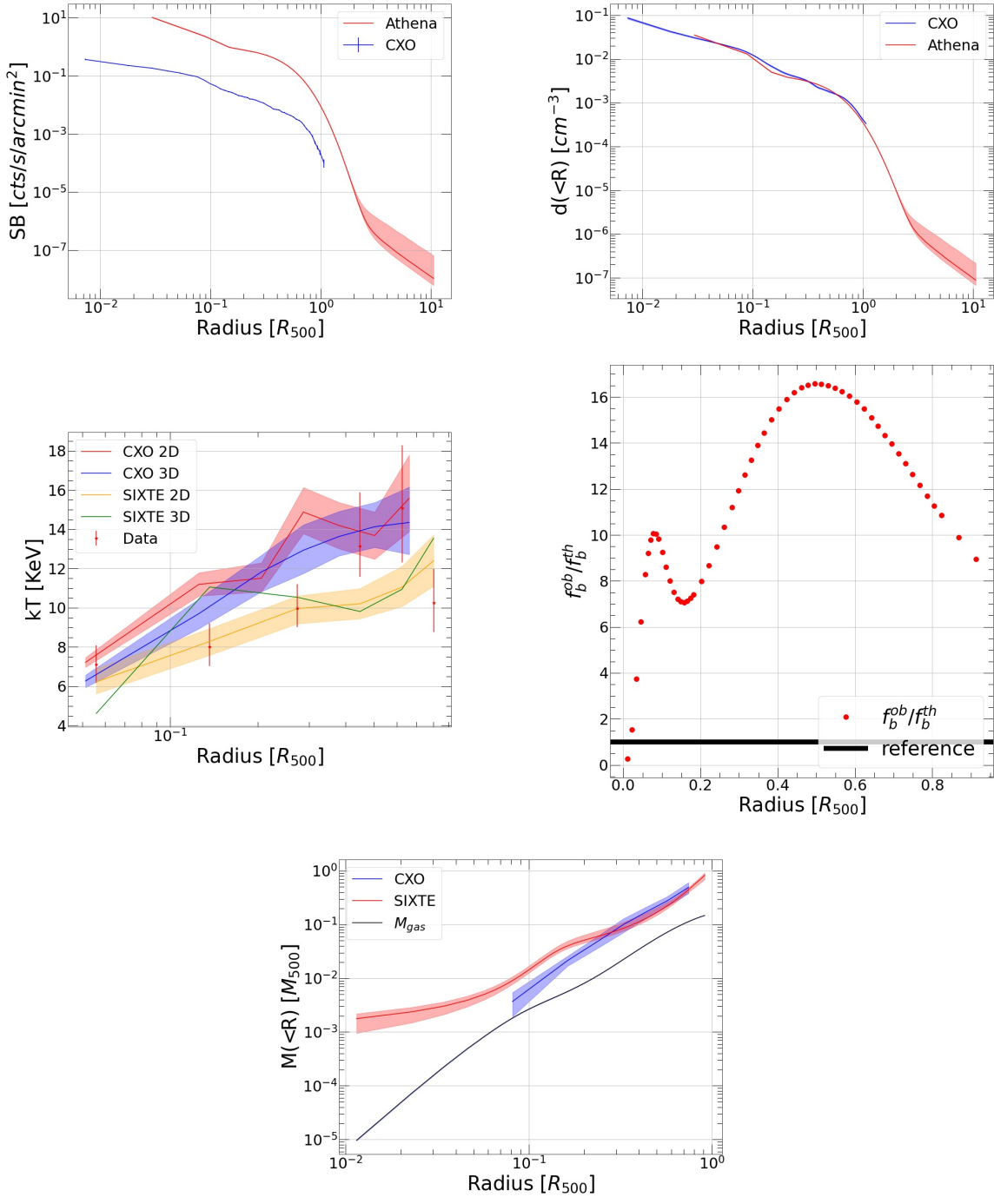


Figure 53: El Gordo: $z = 0.87$, $M_{500}^{CXO} = 1.68 \cdot 10^{15} M_{\odot}$, $R_{500}^{CXO} = 1.30 \cdot 10^3 \text{ kpc}$,
 $T_{exp}^{CXO} \sim 300 \text{ ksec} = 25 T_{exp}^{Ath}$

B Simulated clusters plots

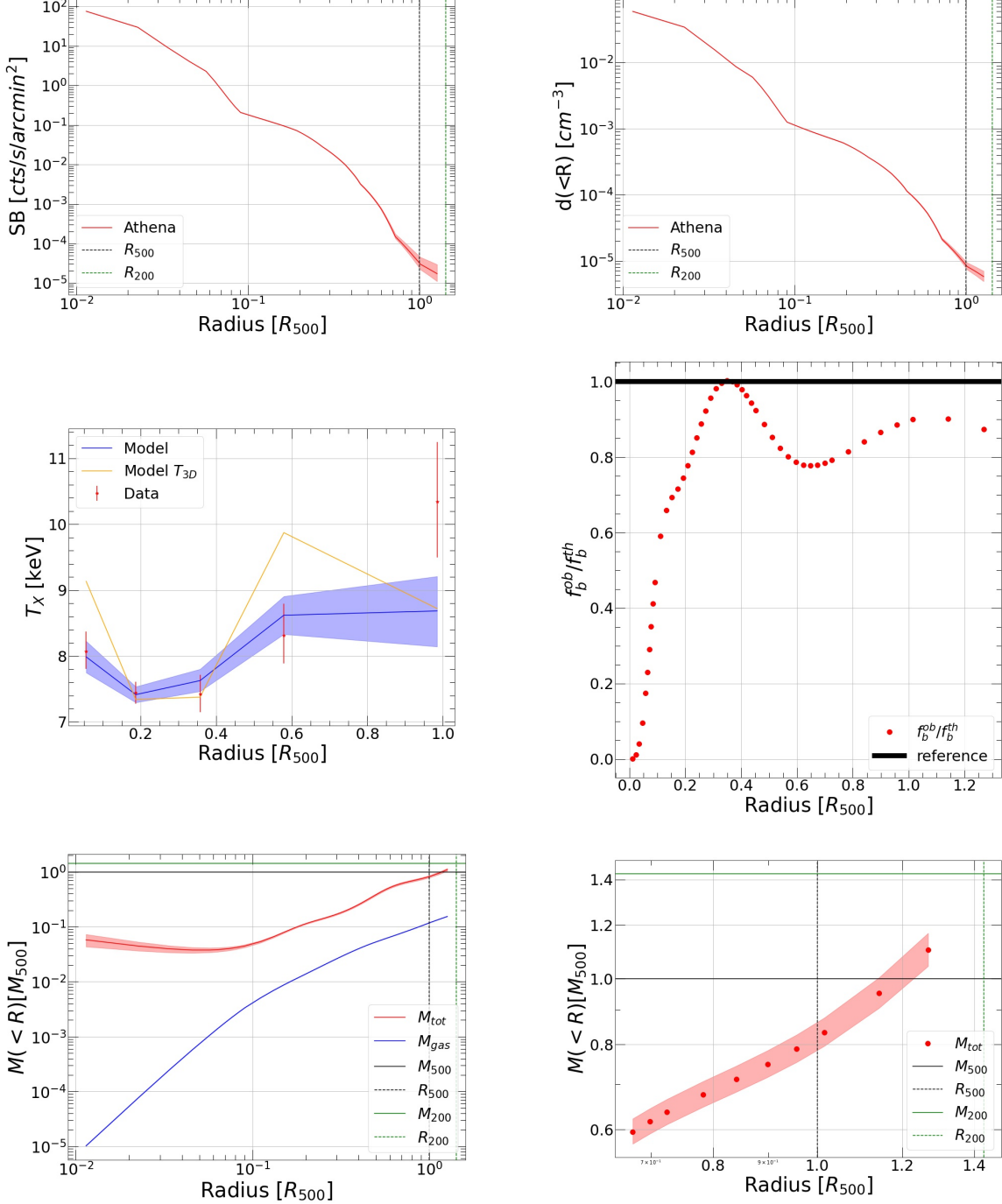


Figure 54: Simulated Cluster 01: $z = 0.33$, $M_{500}^{CXO} = 6.095 \cdot 10^{15} M_\odot$, $R_{500}^{CXO} = 1.30 \cdot 10^3$ kpc, $T_{exp} = 20$ ksec

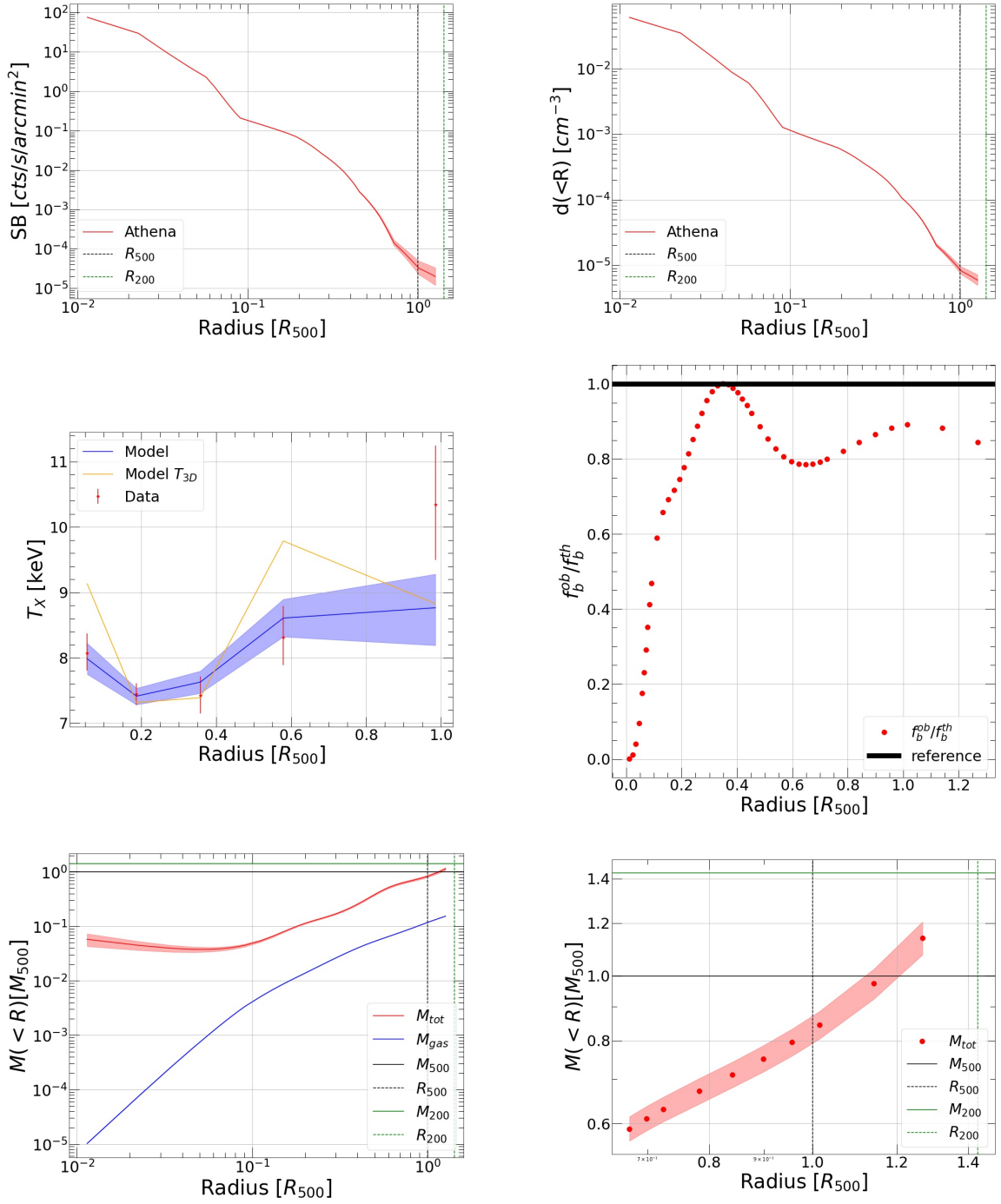


Figure 55: Simulated Cluster 01 (masked sub-structures): $z = 0.33$, $M_{500}^{CXO} = 6.095 \cdot 10^{14} M_\odot$, $R_{500}^{CXO} = 1.30 \cdot 10^3 \text{ kpc}$, $T_{exp} = 20 \text{ ksec}$

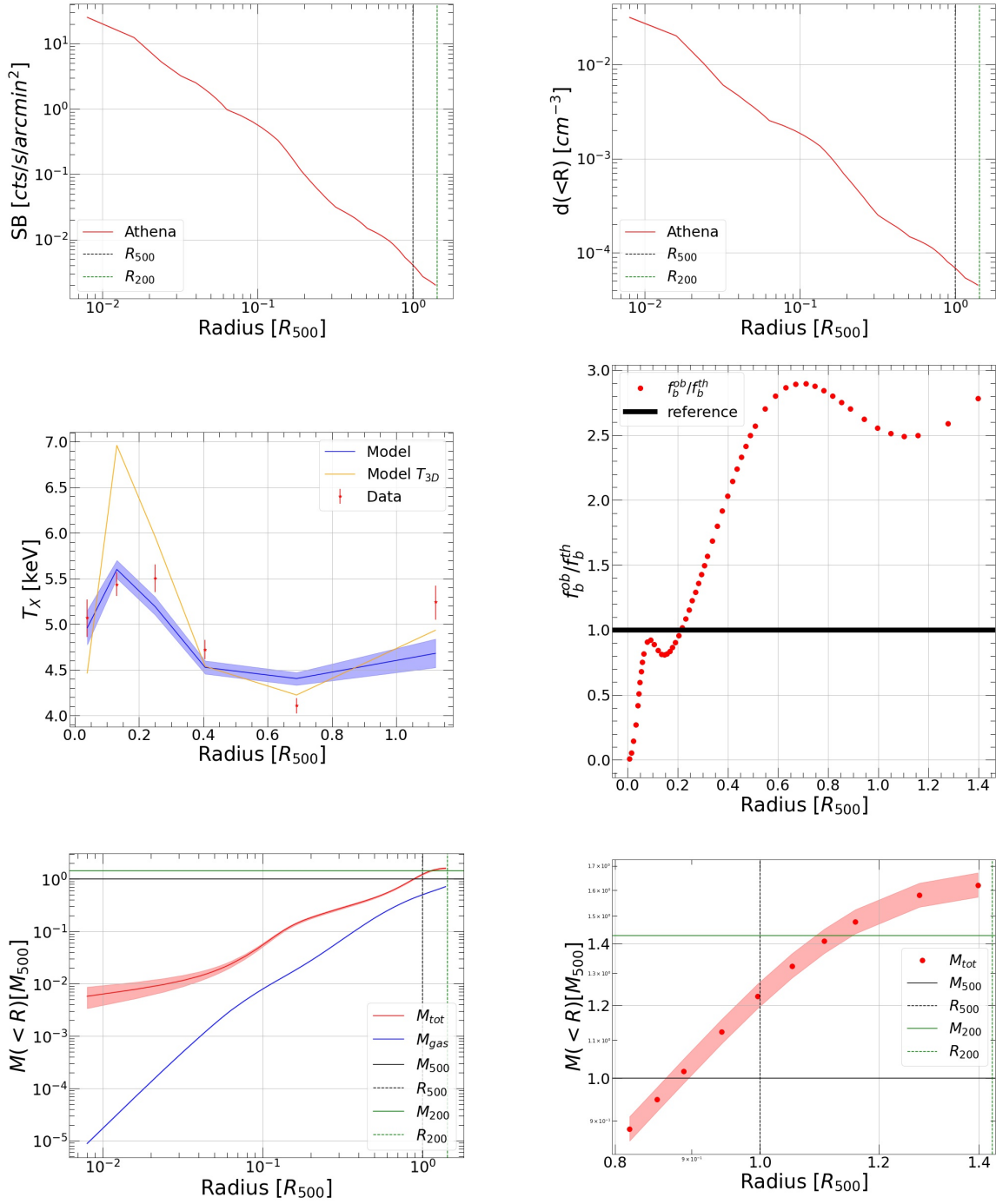


Figure 56: Simulated Cluster 02: $z = 0.33$, $M_{500}^{CXO} = 5.508 \cdot 10^{14} M_\odot$, $R_{500}^{CXO} = 1.16 \cdot 10^3 \text{ kpc}$, $T_{exp} = 20 \text{ ksec}$

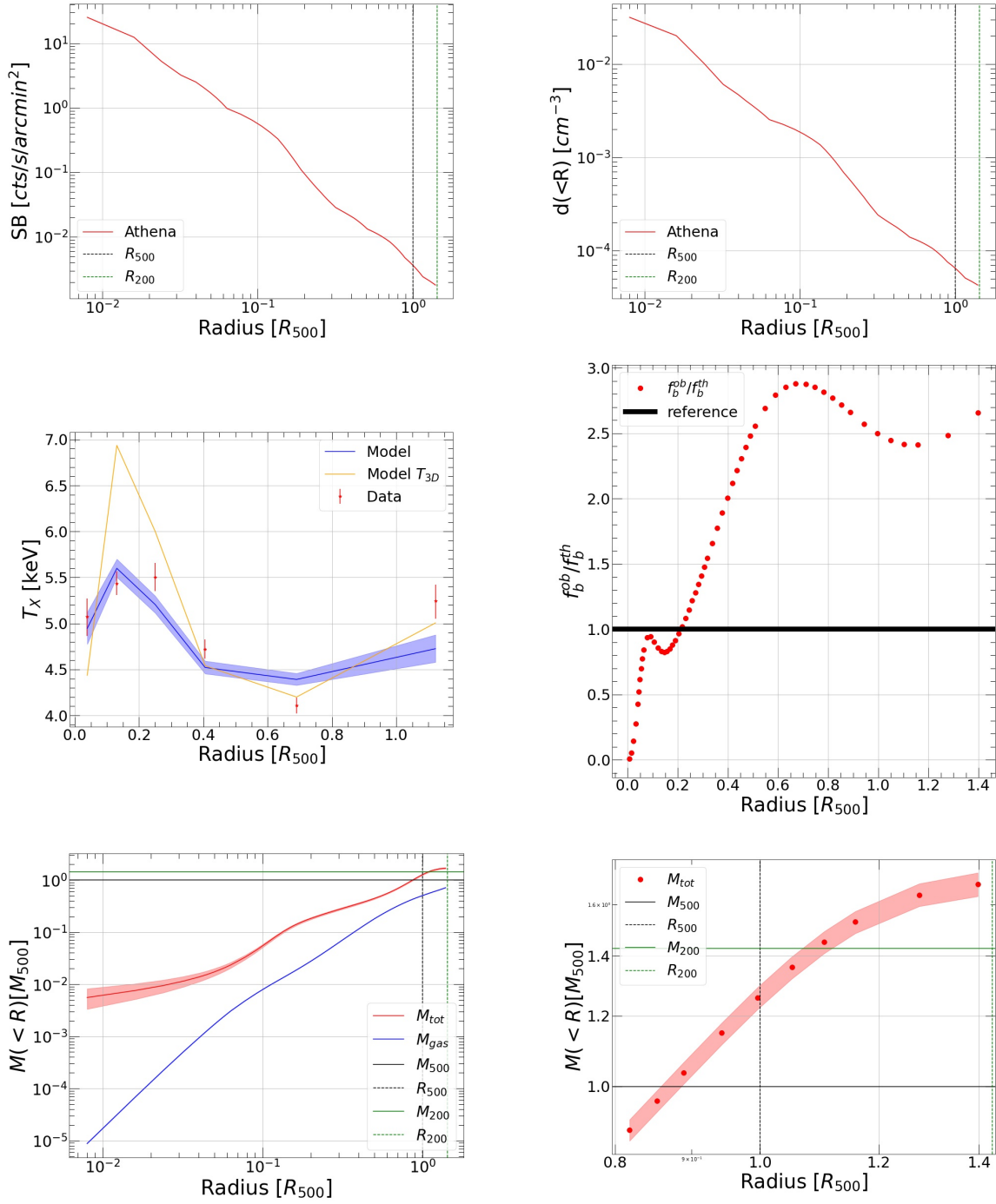


Figure 57: Simulated Cluster 02 (masked sub-structures): $z = 0.33$, $M_{500}^{CXO} = 5.508 \cdot 10^{14} M_\odot$, $R_{500}^{CXO} = 1.16 \cdot 10^3$ kpc, $T_{exp} = 20$ ksec

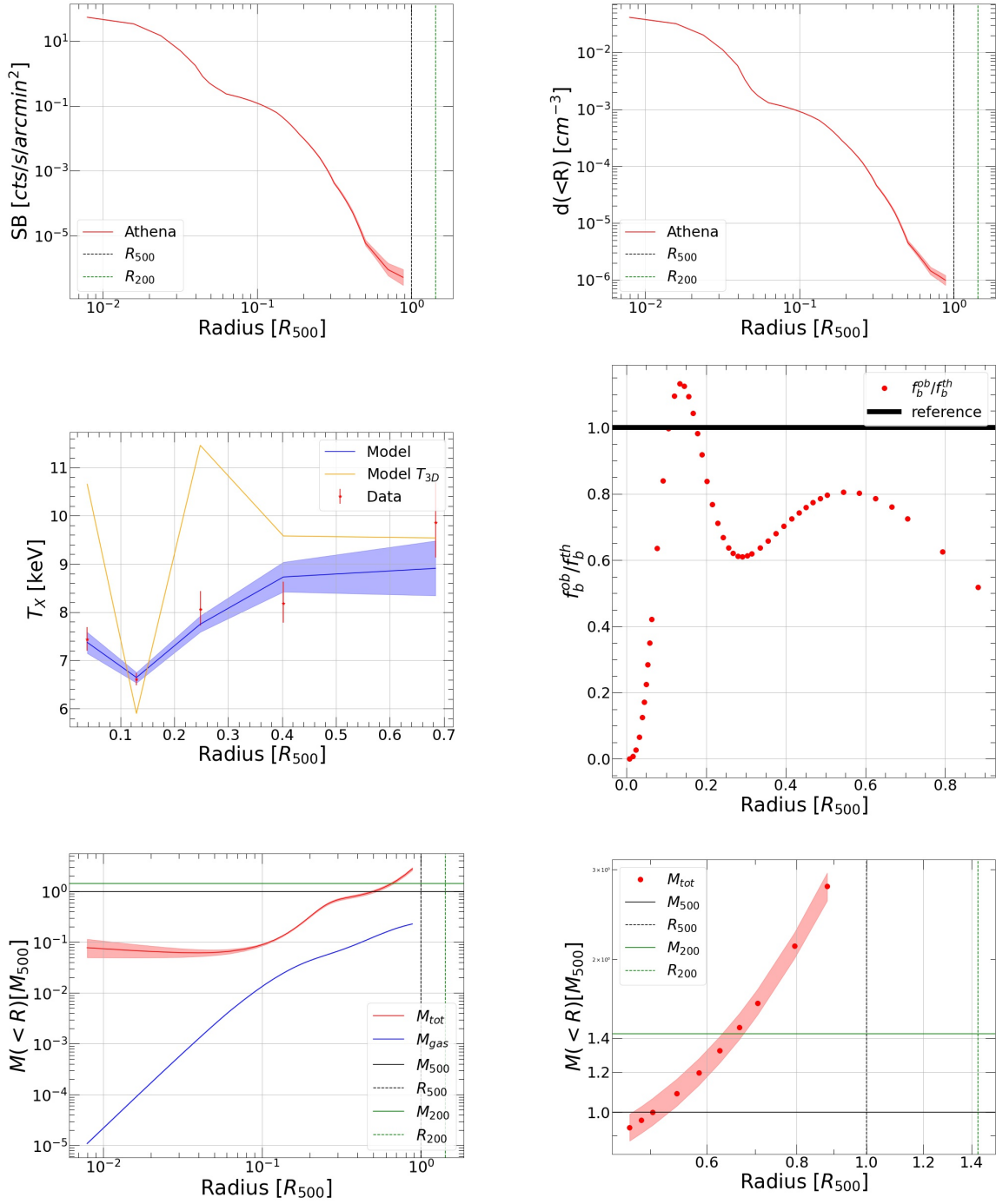


Figure 58: Simulated Cluster 03: $z = 0.33$, $M_{500}^{CXO} = 5.644 \cdot 10^{14} M_\odot$, $R_{500}^{CXO} = 1.17 \cdot 10^3 \text{ kpc}$, $T_{exp} = 20 \text{ ksec}$

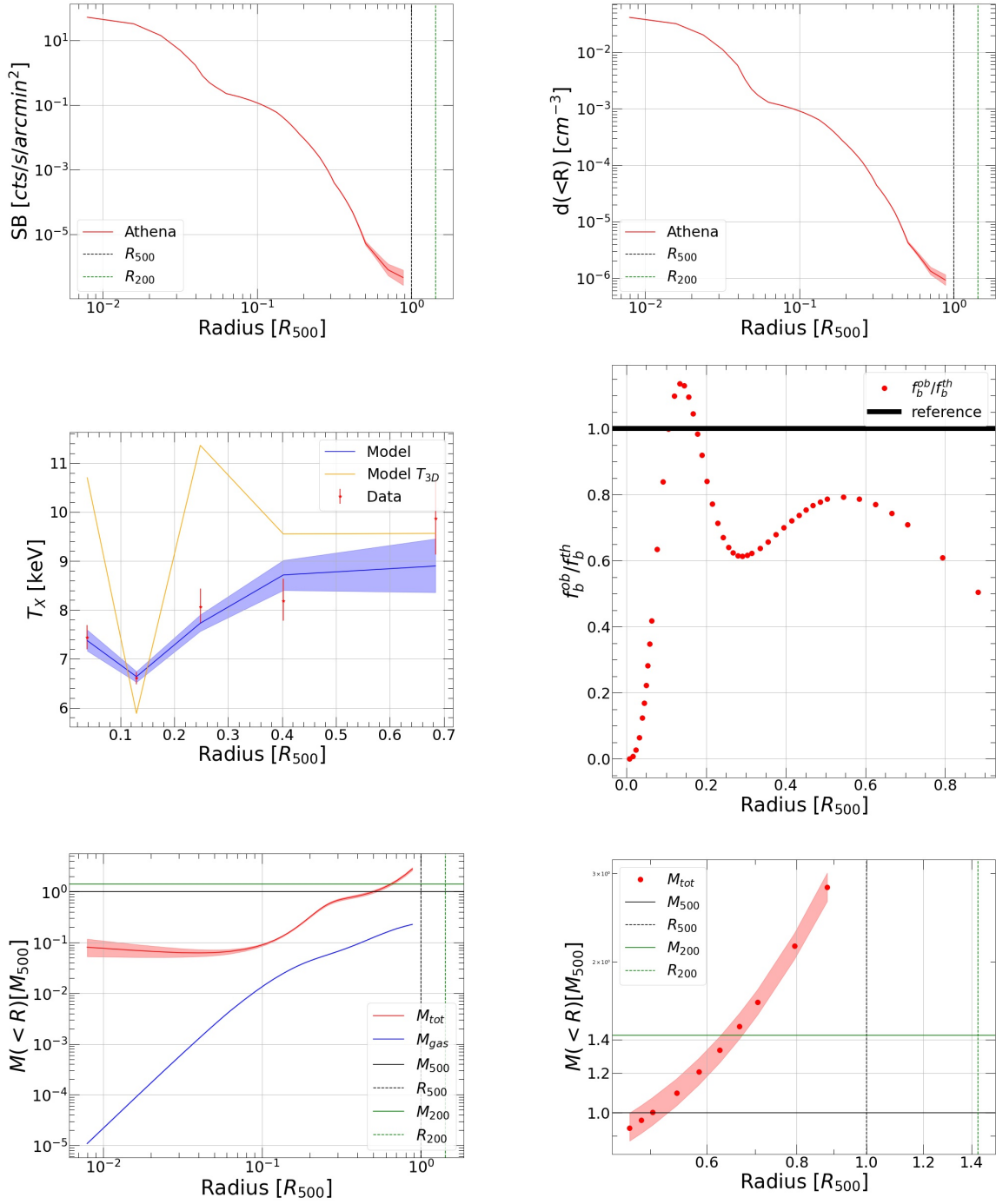


Figure 59: Simulated Cluster 03 (masked sub-structures): $z = 0.33$, $M_{500}^{\text{CXO}} = 5.644 \cdot 10^{14} M_\odot$, $R_{500}^{\text{CXO}} = 1.17 \cdot 10^3 \text{ kpc}$, $T_{\text{exp}} = 20 \text{ ksec}$

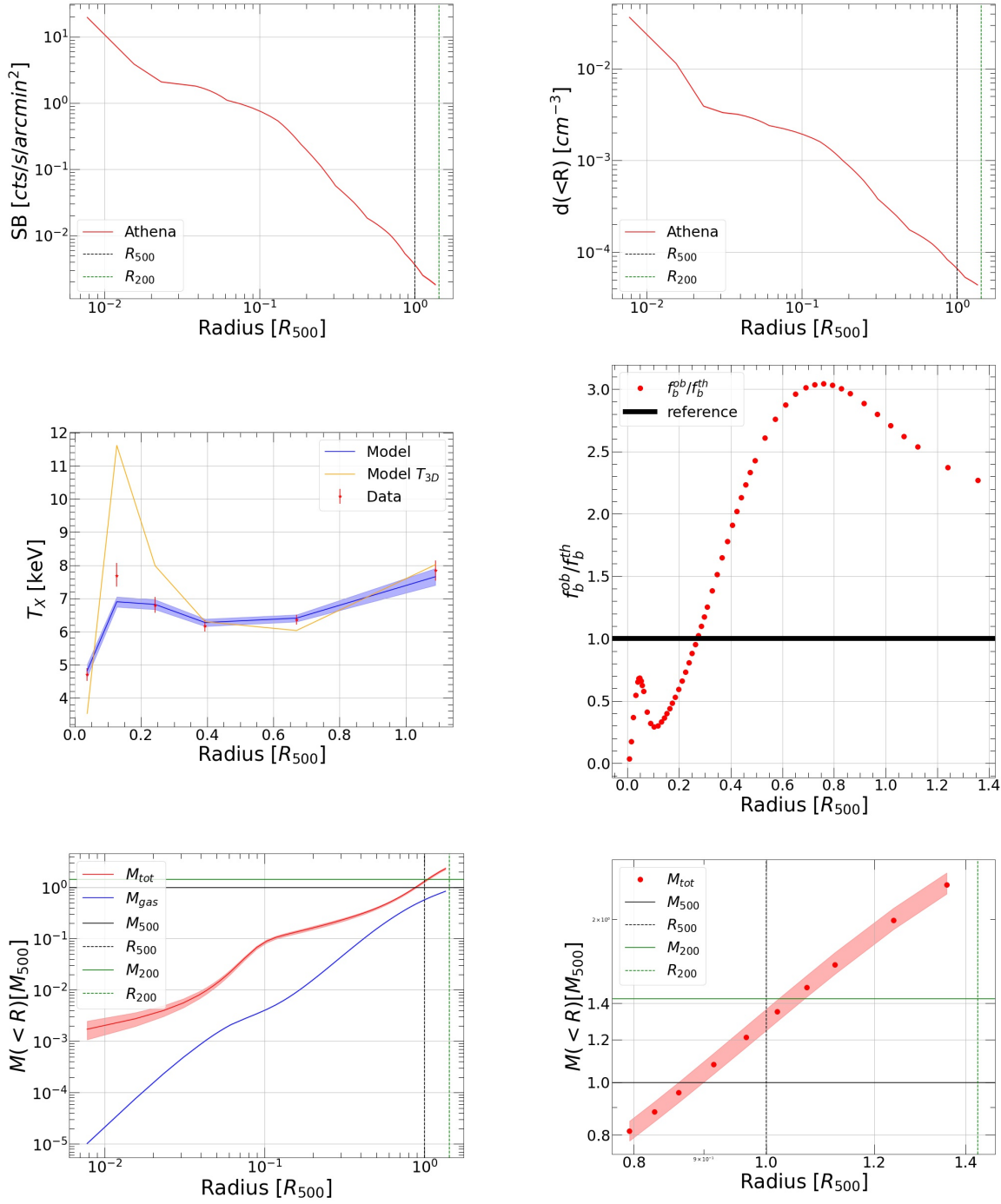


Figure 60: Simulated Cluster 04: $z = 0.33$, $M_{500}^{CXO} = 6.024 \cdot 10^{14} M_\odot$, $R_{500}^{CXO} = 1.20 \cdot 10^3 kpc$, $T_{exp} = 20 ksec$

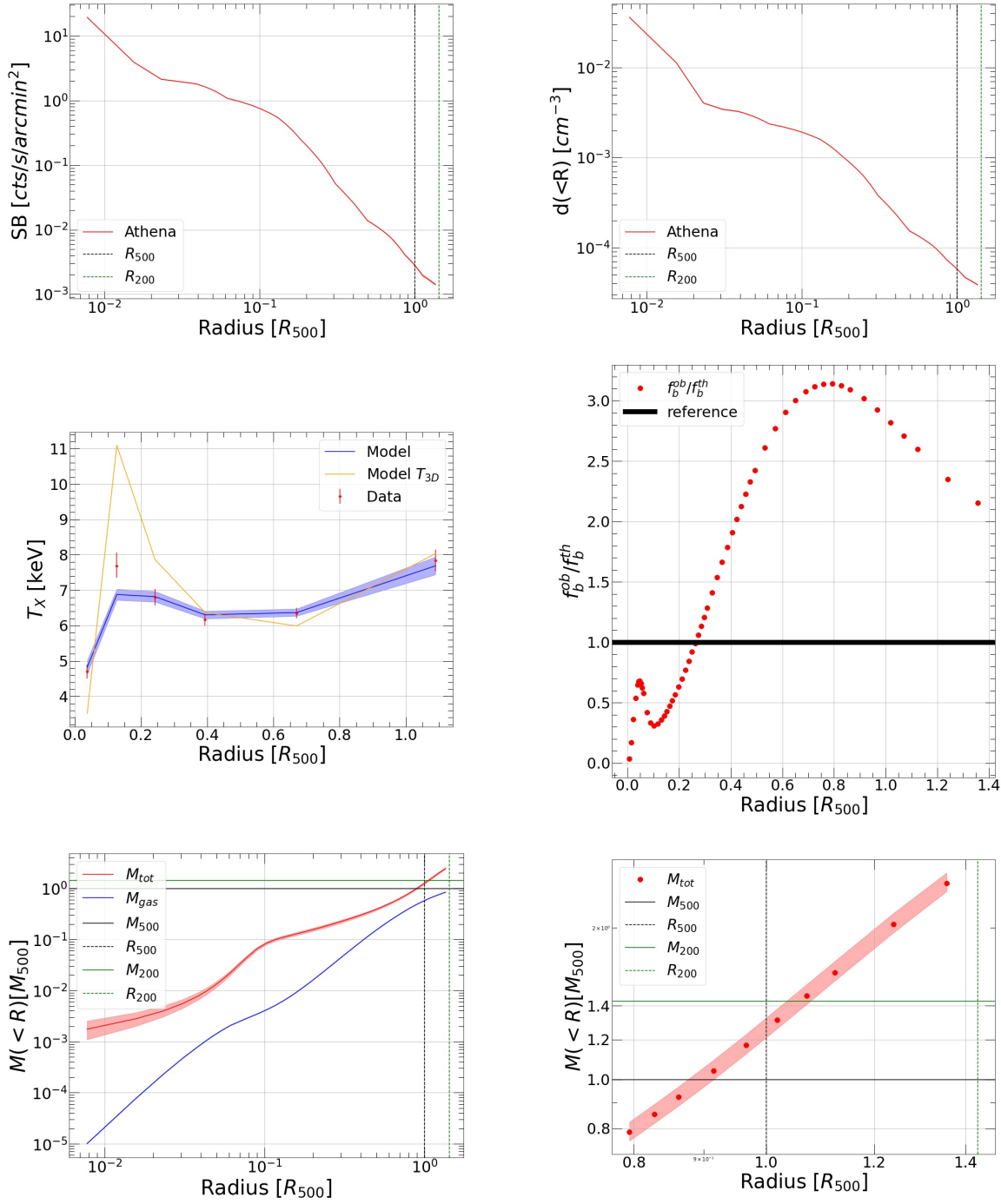


Figure 61: Simulated Cluster 04 (masked sub-structures): $z = 0.33$, $M_{500}^{CXO} = 6.024 \cdot 10^{14} M_\odot$, $R_{500}^{CXO} = 1.20 \cdot 10^3$ kpc, $T_{exp} = 20$ ksec

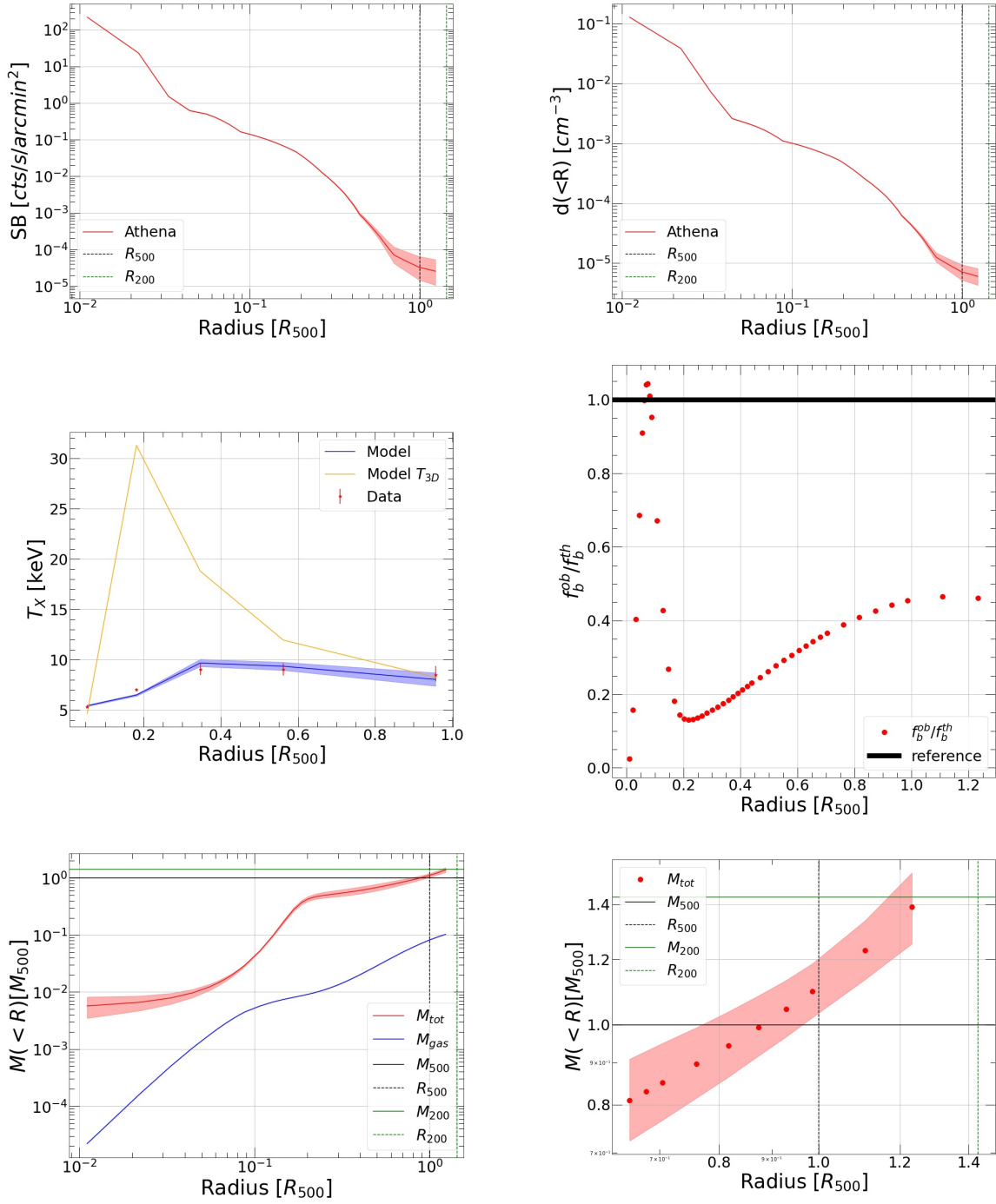


Figure 62: Simulated Cluster 05: $z = 0.33$, $M_{500}^{CXO} = 6.644 \cdot 10^{14} M_\odot$, $R_{500}^{CXO} = 1.24 \cdot 10^3 kpc$, $T_{exp} = 20 ksec$

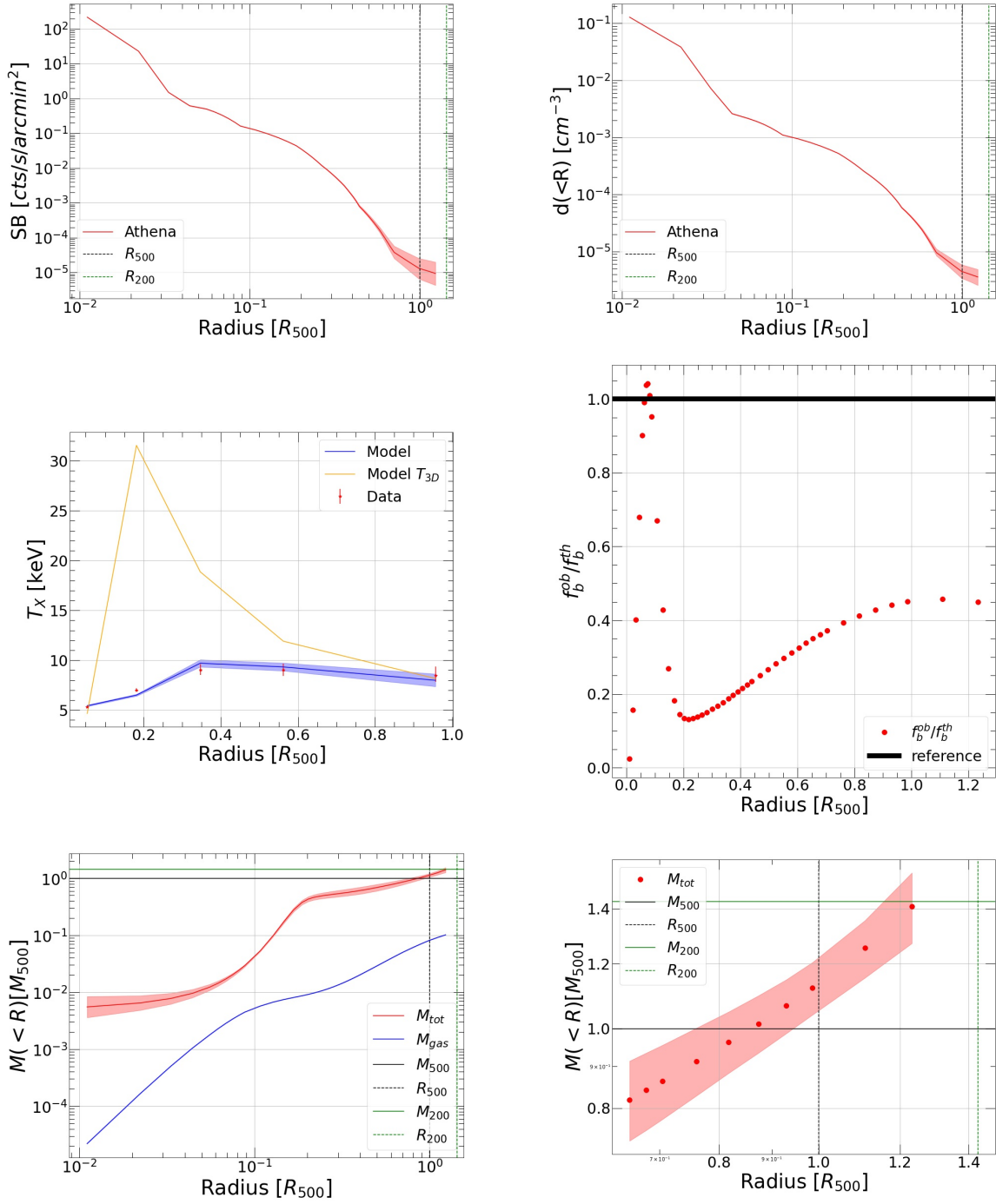


Figure 63: Simulated Cluster 05 (masked sub-structures): $z = 0.33$, $M_{500}^{CXO} = 6.644 \cdot 10^{14} M_\odot$, $R_{500}^{CXO} = 1.24 \cdot 10^3 \text{ kpc}$, $T_{exp} = 20 \text{ ksec}$

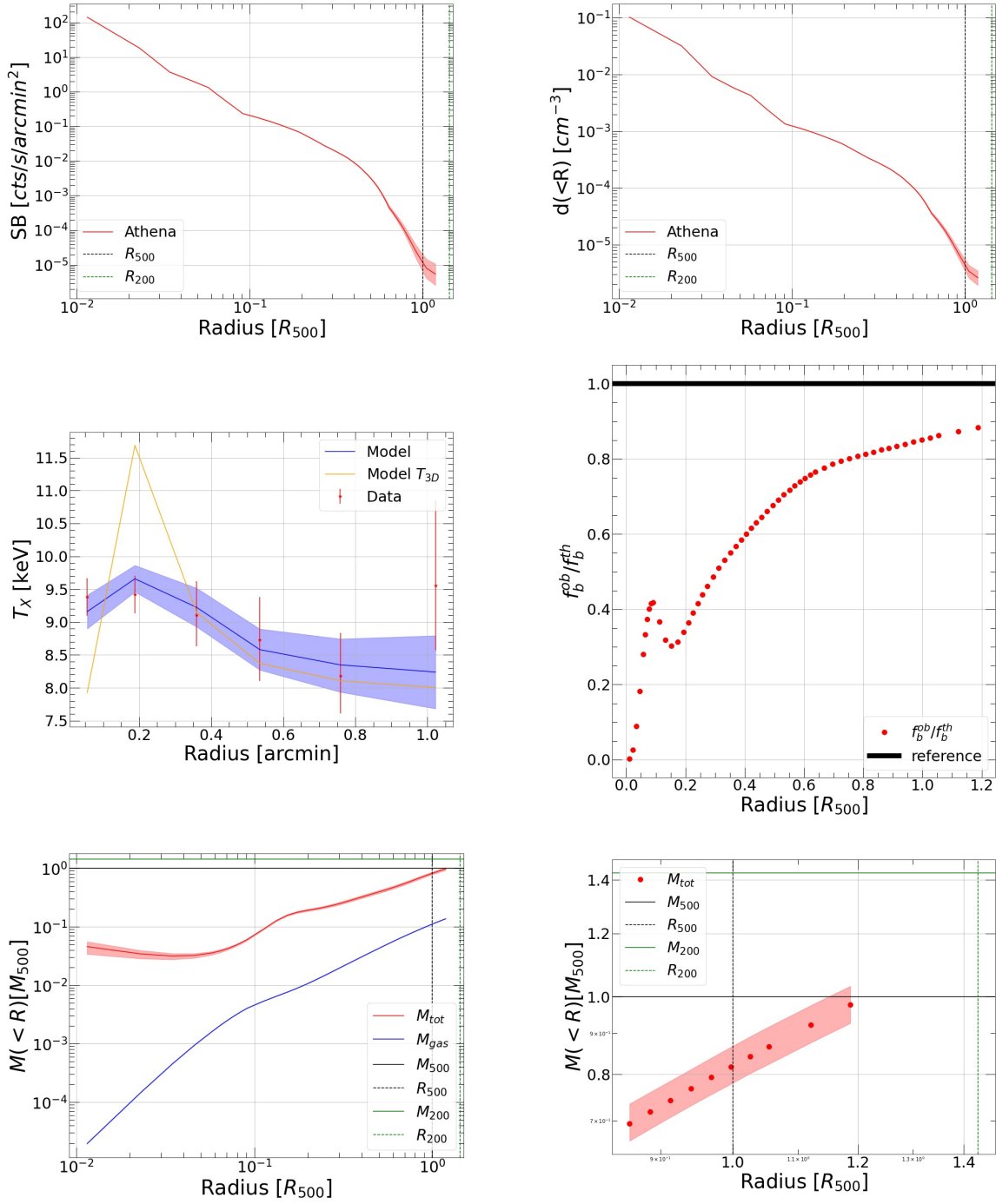


Figure 64: Simulated Cluster 06: $z = 0.33$, $M_{500}^{CXO} = 5.975 \cdot 10^{14} M_\odot$, $R_{500}^{CXO} = 1.196 \cdot 10^3 kpc$, $T_{exp} = 20 ksec$

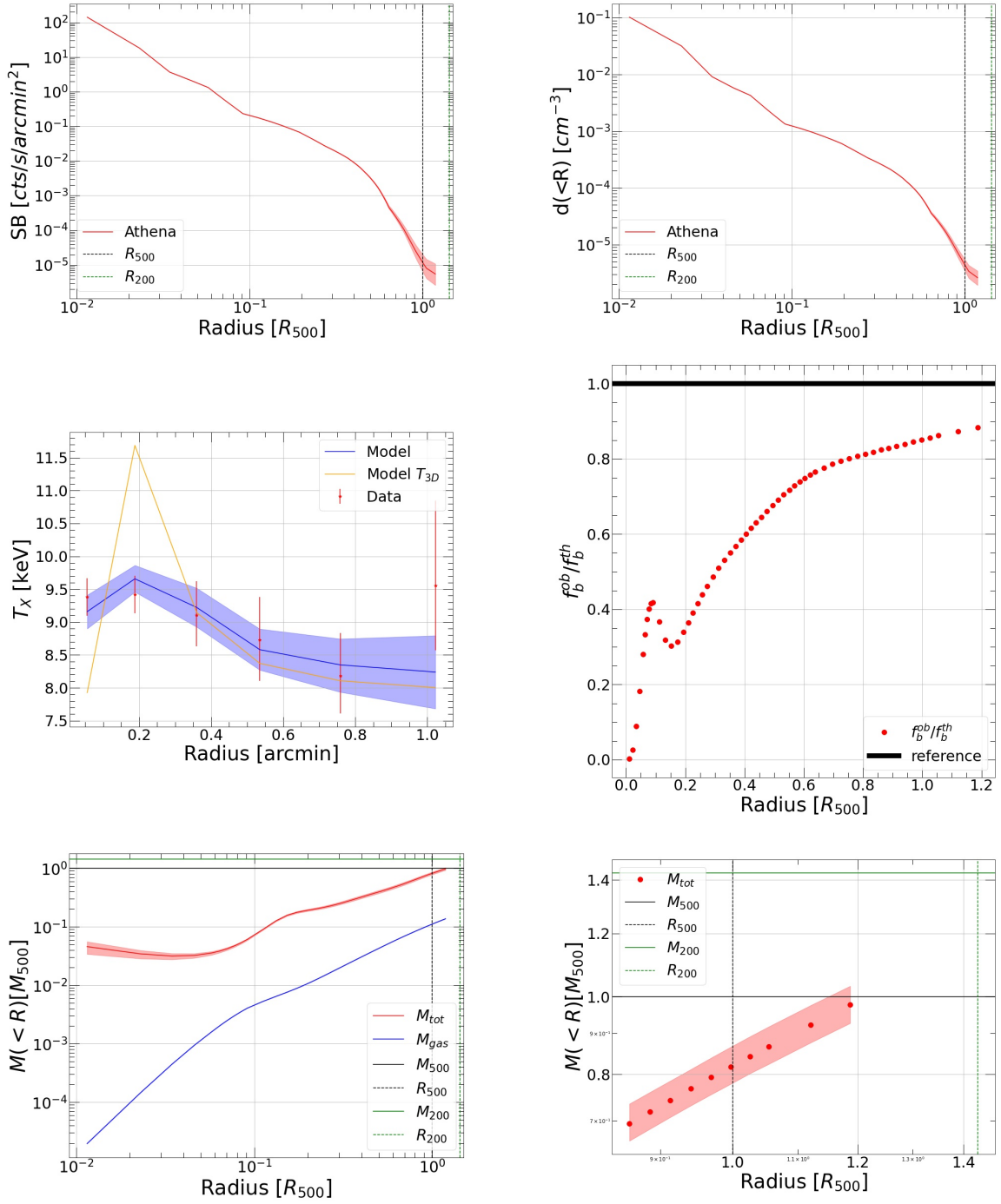


Figure 65: Simulated Cluster 06 (masked sub-structures): $z = 0.33$, $M_{500}^{CXO} = 5.975 \cdot 10^{14} M_\odot$, $R_{500}^{CXO} = 1.196 \cdot 10^3 \text{ kpc}$, $T_{exp} = 20 \text{ ksec}$

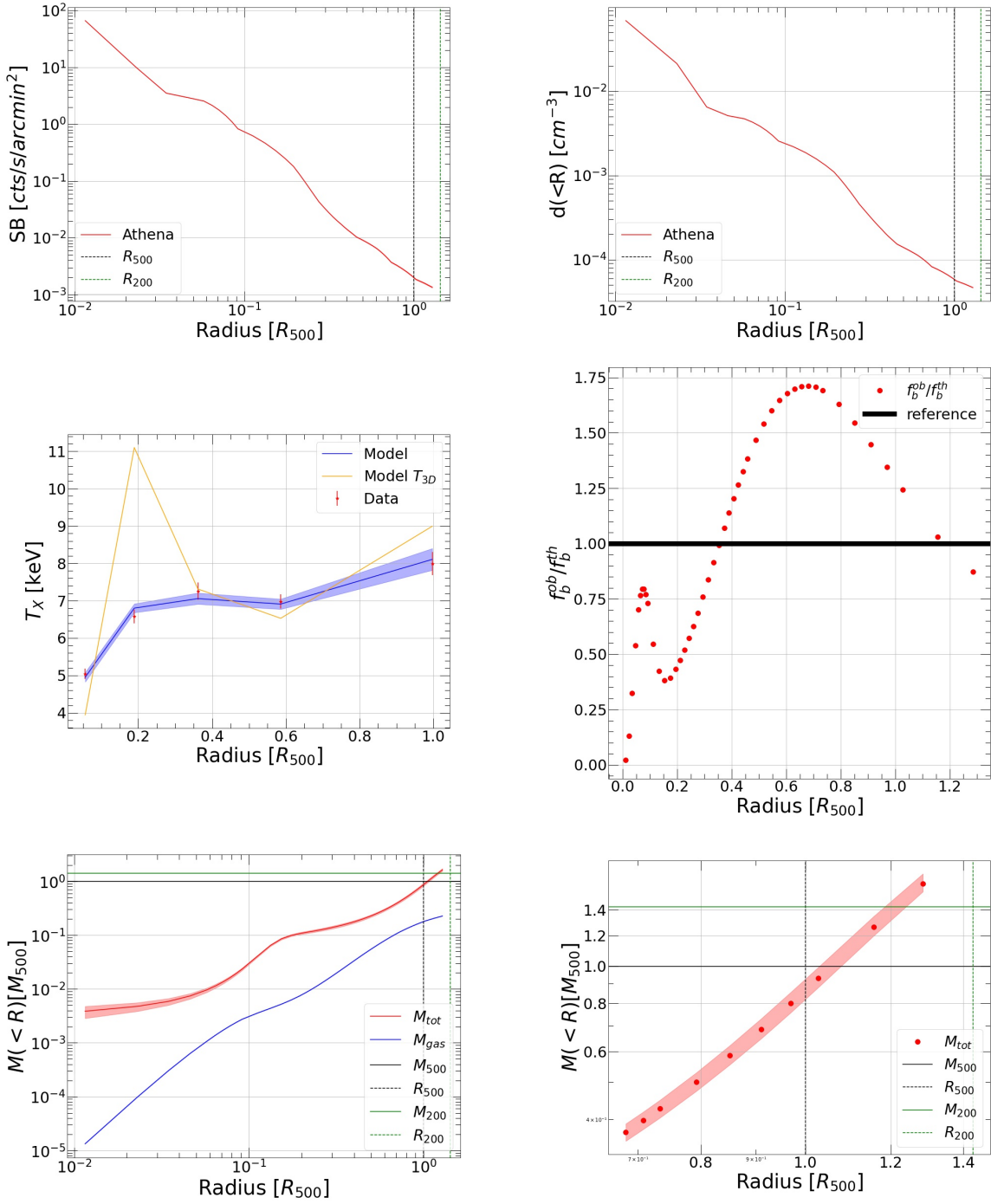


Figure 66: Simulated Cluster 07: $z = 0.33$, $M_{500}^{CXO} = 5.868 \cdot 10^{14} M_\odot$, $R_{500}^{CXO} = 1.189 \cdot 10^3 \text{ kpc}$, $T_{exp} = 20 \text{ ksec}$

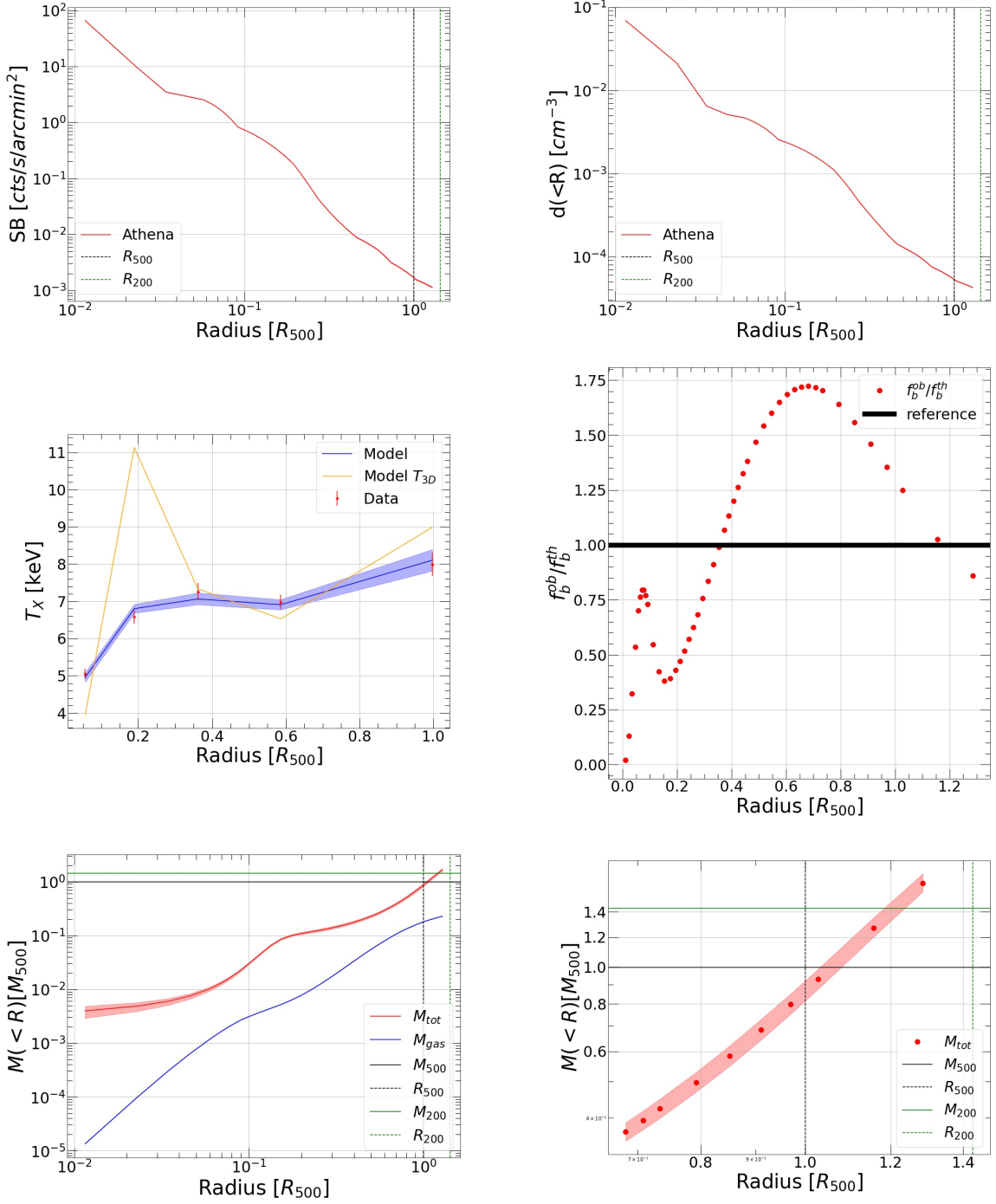


Figure 67: Simulated Cluster 07 (masked sub-structures): $z = 0.33$, $M_{500}^{C\!X\!O} = 5.868 \cdot 10^{14} M_\odot$, $R_{500}^{C\!X\!O} = 1.189 \cdot 10^3 \text{ kpc}$, $T_{\text{exp}} = 20 \text{ ksec}$

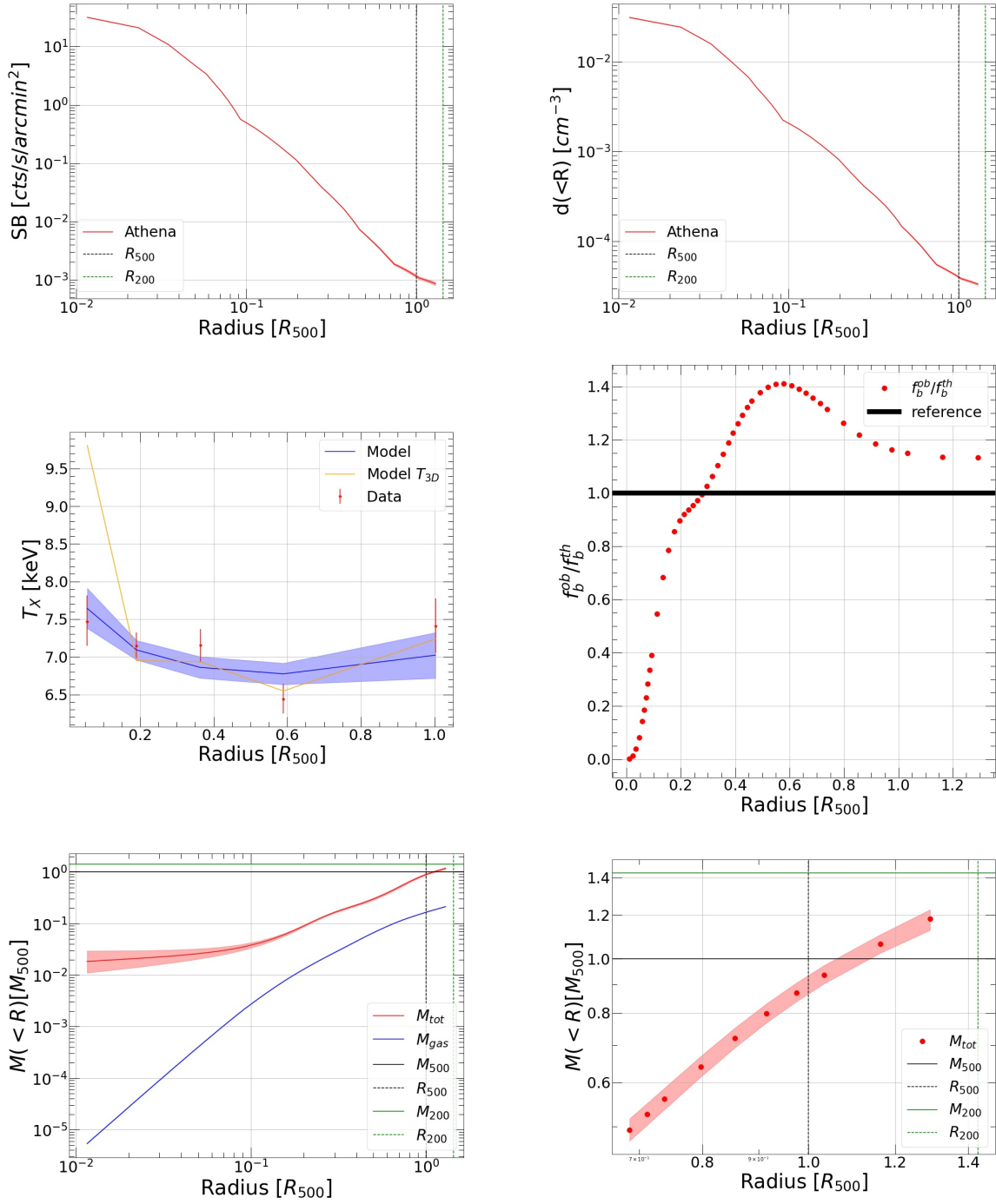


Figure 68: Simulated Cluster 08: $z = 0.33$, $M_{500}^{CXO} = 5.767 \cdot 10^{14} M_\odot$, $R_{500}^{CXO} = 1.182 \cdot 10^3 \text{ kpc}$, $T_{exp} = 20 \text{ ksec}$